Simulations for new battery materials

Hungru Chen

1st supervisor: Prof. John H. Harding

2nd supervisor: Prof. Anthony R. West

Submitted for the degree of Doctor of Philosophy

Department of Materials Science and Engineering
The University of Sheffield

November 2012

Declaration

This thesis has been composed by myself and has not been submitted or accepted in any previous degree application. The work in this thesis has been conducted by myself, except where acknowledgement has been given.

Hungru Chen

November 2012

Acknowledgements

First and foremost, I would like to express my gratitude to my supervisor Prof. John H. Harding for helpful suggestions and illuminating discussions on this thesis. I thank everyone I met in the Materials Science and Engineering department, especially those who have been harassed by my endless questions. Finally I thank my parents and family for their support.

Abstract

Using first-principles density functional calculations, $LiNiO_2$-related cathode materials are studied. It is found that in contrast to previous studies, the hole state in Li doped NiO shows predominately Ni character and is accompanied by a local Jahn-Teller distortion. We show that this is consistent with experiments. A new potential ground state $LiNiO_2$ cell is found in which charge disproportionation $Ni^{3+} \rightarrow Ni^{2+} + Ni^{4+}$ occurs. However another cell in which the Jahn-Teller distortions of Ni^{3+} octahedral are in a zigzag ordering, is close in energy. Therefore we suggest that in real $LiNiO_2$ samples, the two phases coexist. This explains the absence of long range ordering in $LiNiO_2$.

Rock-salt $LiMO_2$ compounds crystallise in three different structures depending on the cation ordering. We show that this cannot be explained by the size effect and propose that the exchange interaction between M ions is responsible for the ordering. Both size difference between Li and M and the exchange interaction between nearest-neighbouring M ions favour the layered structure, whereas the exchange interaction between second-nearest-neighbouring M ions destabilises the layered structure.

The defect formation energies are low in $LiNiO_2$, consistent with the difficulty to synthesise truly stoichiometric $LiNiO_2$. The tendency for Ni to be present in the Li layers can be explained by super-exchange interactions. Therefore with Co substitution for Ni, the nonmagnetic Co ions screen these interactions and destabilise the presence of Ni in the Li layer. The same effect is found with Al substitution from our calculations. We also show why substitution of Ni by Mn increases the concentration of the interlayer mixing defects worse compared to $LiNiO_2$. In addition, a correlation between the oxygen charge and the defect formation of oxygen vacancy is found. It appears that the lower the effective oxygen charge, the smaller the defect formation energy.

Table of Contents

Published work

The work described in this thesis has led to the following two publications.

1. "Charge disproportionation and Jahn-Teller distortion in $LiNiO_2$ and $NaNiO_2$: A density functional theory study," Hungru Chen, Colin. L. Freeman and John H. Harding, *Physical Review B* **84**, 085108 (2011)

2. "Nature of the hole states in Li-doped NiO," Hungru Chen and John H. Harding, *Physical Review B* **85**, 115127 (2012)

Chapter 1

Introduction

1.1 Lithium ion batteries

Since the commercialisation by SONY in 1991, lithium ion batteries have become an indispensible part of our life. They show higher energy density compared to conventional rechargeable batteries, no memory effect or self-discharge. Therefore they are now used to power almost all our portable electronic devices like mobile phones, music players, digital cameras and laptops. There is also a demand for the storage of renewable energies. The lithium ion battery is certainly one of the candidates since it offers high energy density. Also Li ion batteries are looking to replace petrol as the power source in automobiles in order to reduce their carbon footprint.

A lithium ion battery is composed of three parts, the anode (negative electrode), electrolyte and cathode (positive electrode) as illustrated in figure 1-1. Upon charging, lithium ions are extracted from cathode, drift across the electrolyte and are inserted into the anode. Meanwhile the electrons flow through the external circuit from cathode to anode. Using the common cathode material $LiCoO_2$ and anode material graphite as an example, the reactions at the electrodes are:

- Cathode

$$LiCoO_2 \xrightarrow{charge} Li_{1-x}CoO_2 + xLi^+ + xe^-$$

- Anode

$$C + xLi^+ + xe^- \xrightarrow{charge} Li_xC$$

- Overall

$$LiCoO_2 + C \xrightarrow{charge} Li_xC + Li_{1-x}CoO_2$$

Upon discharging, the exactly reverse process occurs.

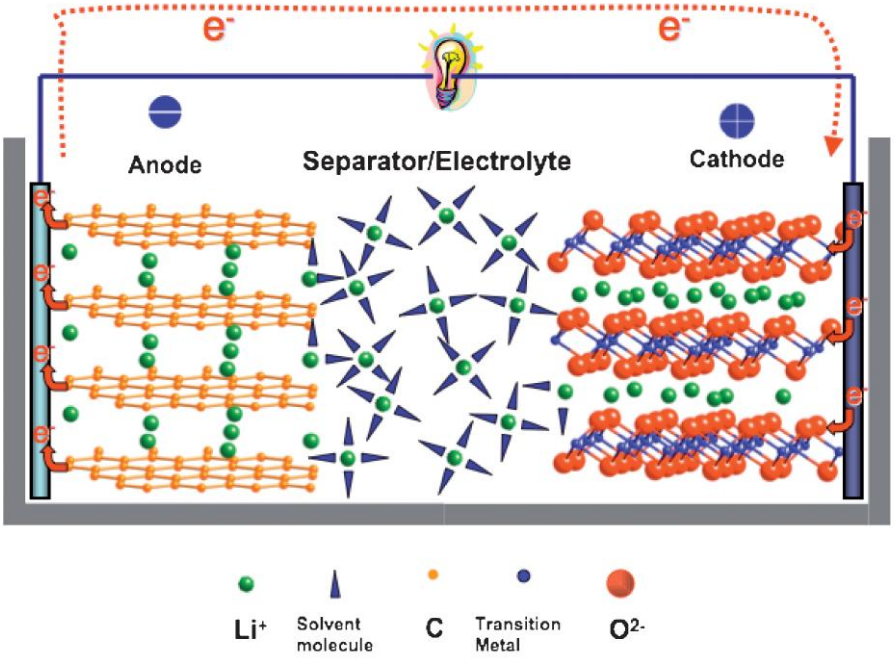

Figure 1-1: Illustration of the three main components in a lithium ion battery. Upon charging and discharging, lithium ions drift across the electrolyte between the two electrodes. This image is taken from [1].

Figure 1-2 is a schematic electronic energy diagram of a Li ion battery at open circuit. μ_A and μ_c are the electrochemical potentials of the anode and the cathode respectively. In the electrolyte, the energy separation E_g between the lowest unoccupied molecular orbital (LUMO) and the highest occupied molecular orbital (HOMO) is called the potential window. If μ_A locates above the LUMO, the electrolyte gets reduced. Similarly if μ_c locates below the HOMO, the electrolyte gets oxidized. Therefore to form a thermodynamically stable battery, the positions of μ_A and μ_c must lie within the potential window of the electrolyte, which imposes the constraint on the open circuit voltage V_{oc} of a battery

$$eV_{oc} = \mu_A - \mu_c \leq E_g$$

Therefore to achieve a high battery voltage the electrolyte should offer a wide potential window. Also it should have high Li-ion conductivity but be electronically insulating in order to avoid internal short-circuiting. And for safety reasons, it should be non-flammable.

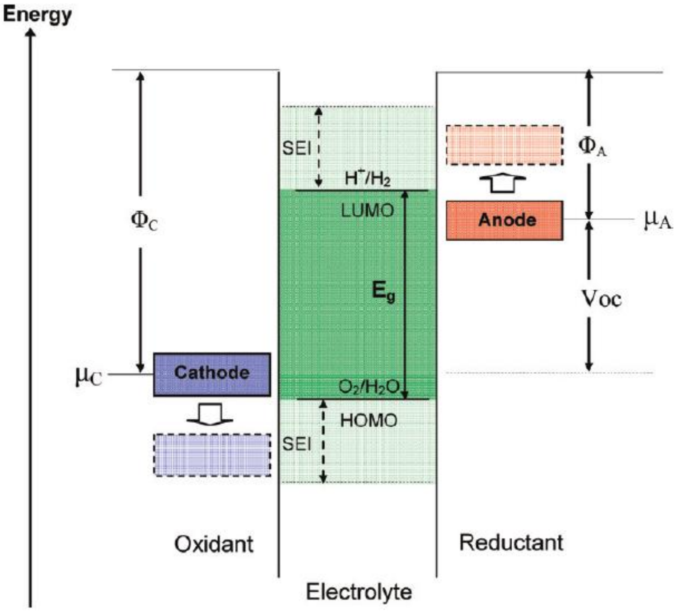

Figure 1-2: Schematic energy diagram of a lithium battery at open circuit. Φ_A and Φ_B are the work functions of the anode and cathode. E_g is the window of the electrolyte for thermodynamics stability. For a μ_A higher than LUMO and/or a μ_C lower than HOMO, a kinetic stability is required by the formation of an SEI (solid-electrolyte interface) layer. The image is taken from [2].

Good electrode materials should possess the following characteristics:

- Lithium ions should be able to be reversibly extracted from and inserted into the material without changing its host structure. The higher quantity of Li ion that can be reversibly intercalated per formula unit, the higher is the capacity.
- The cathode should have a high (positive) electrochemical potential and the anode should have a low electrochemical potential in order to obtain a high battery voltage.
- The mobility of Li ions should be high in electrode materials. High mobility enables rapid extraction and insertion of Li ions and gives high rate capability (high power).
- The electronic conductivity should be as good as the Li conductivity or better for high rate capability (high power).
- High thermal stability for the use in various ambient conditions.
- The electrode materials should be compatible with the electrolyte. This means that the Fermi levels of both cathode and anode should lie within the potential window of the electrolyte. Also there should not be chemical reactions between the electrodes and the electrolyte.
- From a commercial point of view, electrode materials should be inexpensive and easy to synthesise.
- Electrode materials should be non-toxic and environmentally benign.

Although both anode and cathode are equally important in a Li ion battery, the restriction of the performance of current Li ion batteries comes from cathode materials. As seen in figure 1-3, cathode materials display less specific capacity than the commercially used anode material graphite. Therefore cathode materials are the main focus in this thesis.

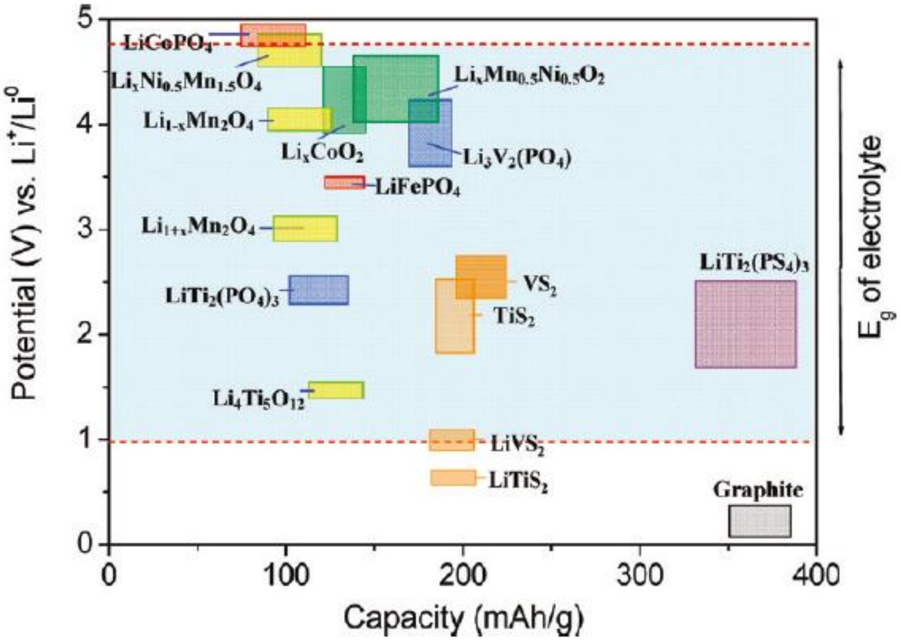

Figure 1-3: Voltage versus capacity of several electrode materials. Materials denoted with the same colour have the same crystal structure. The image is taken from [2].

1.2 Cathode materials

All currently used cathode materials can be divided into three main categories according to their crystal structures. As shown in figure 1-4, they can be layered structures, spinel structures or olivine structures. The common feature of these structures is that Li can be extracted and inserted in and out of the structure.

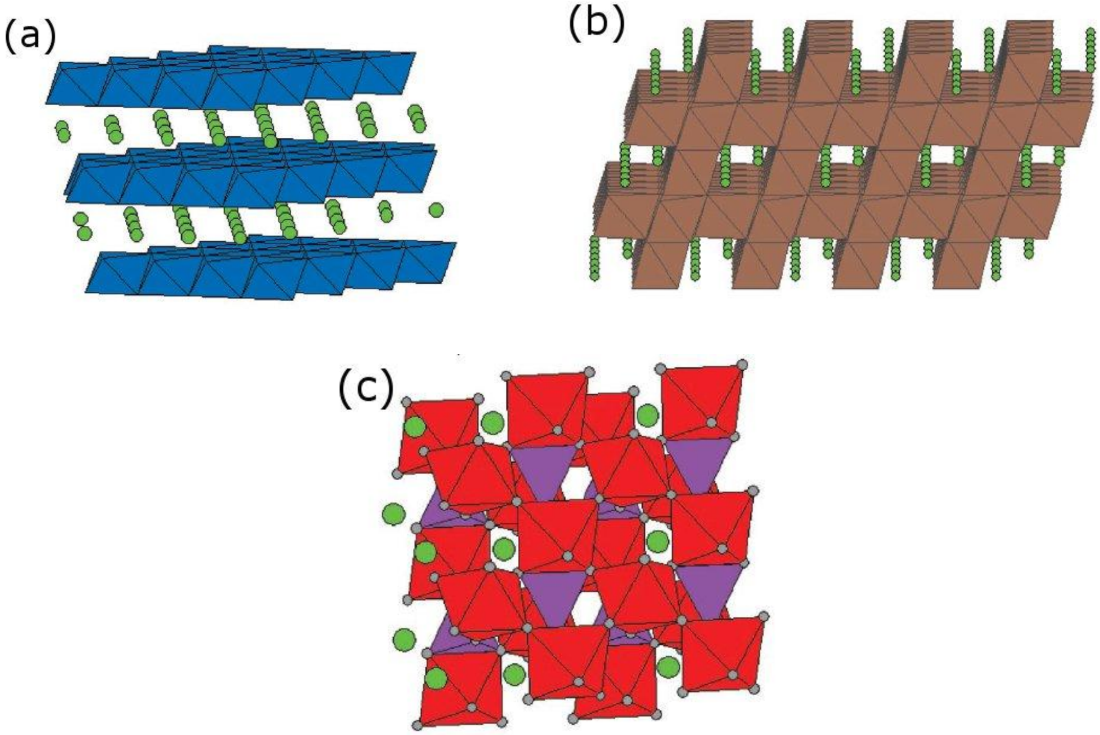

Figure 1-4: (a) Layered (b) spinel and (c) olivine structures. Lithium is denoted in green. In the layered structure, the edge-sharing octahedra form a two-dimensional network. In the spinel and olivine structure, the polyhedra form three-dimensional networks. The image is taken from [3].

1.2.1 Cathode materials with the layered structure

The first and most commonly used cathode material is $LiCoO_2$ and it exhibits the layered rocksalt structure. This structure has alternating transition metal and lithium layers with oxygen layers in between them, as shown in figure 1-4. The CoO_2 layers are composed of edge sharing CoO_6 octahedra which makes it a rigid host for lithium intercalation. Nevertheless, partially delithiated Li_xCoO_2 is meta-stable when $x<1$[4]. It is suggested that delithiated Li_xCoO_2 decomposes to spinel Co_3O_4 and stoichiometric $LiCoO_2$ with oxygen evolution and that the lower the Li content is, the easier the decomposition process. Such irreversible structural transformation is responsible for capacity loss. Therefore, in practice, only half of the lithium can be reversibly cycled without significant capacity fading which results from structural change. Besides the process of oxygen evolution associated with the structural change at low lithium content is exothermic and could cause an explosion. This is a serious safety concern.

$LiNiO_2$ is a potential cathode material to replace $LiCoO_2$ because cobalt is toxic and expensive. Although it is usually reported to adopt the layered structure, there is always a certain amount of extra Ni present in the Li layers which makes its real formula $Li_{1-x}Ni_{1+x}O_2$[5]. So far no truly stoichiometric $LiNiO_2$ material is available. The presence of Ni in the Li layers degrades the electrochemical property as a cathode[6]. Also, similar to $LiCoO_2$, partially delithiated $LiNiO_2$ is unstable. Layered Li_xNiO_2 transforms irreversibly to spinel-like and disordered rock-salt structures accompanied by oxygen evolution at a lower temperature compared to Li_xCoO_2[4]. This makes $LiNiO_2$ even more dangerous than $LiCoO_2$. Overall, $LiNiO_2$ is not an ideal cathode material. However these problems can be overcome by partially substituting Ni with other cations.

$LiVO_2$ and $LiCrO_2$ also crystallize in the layered structure. However in $Li_{1-x}VO_2$, after the Li deintercalation the V ions migrate to the Li layers rapidly which causes irreversible structural change[7]. This makes it difficult to insert Li back into the structure and results in poor electrochemical performance as a cathode. $LiCrO_2$ is electrochemically inactive[8]. Only tiny amounts of Li can be extracted from its structure.

$LiMnO_2$ and $LiFeO_2$ have attracted immense interest as replacements for $LiCoO_2$ because Mn and Fe are cheap and non-toxic. Unfortunately stable phases of $LiMnO_2$ and $LiFeO_2$ do not adopt the layered structure [9, 10] and consequently it is difficult to extract Li from them. Although layered $LiMnO_2$[11] and $LiFeO_2$[12] have been reported, they are meta-stable and can only be obtained from low-temperature synthesis methods such as ion-exchange. Besides, they transform back to non-layered structure upon lithium deintercalation and are again not suitable for the use as cathodes.

Recently many research groups have started to shift their attention to $NaMO_2$ because all $NaMO_2$ (M=first row transition metals) adopt the layered rocksalt structure and some of them have been reported to show promising electrochemical performance as cathodes[13-15]. For example, it is reported that 0.8 Na per formula unit in layered $NaMnO_2$ can be reversibly deintercalated and intercalated[15]. Such performance is better than its lithium counterpart $LiMnO_2$. However sodium is heavier than lithium and therefore sodium based cathode materials exhibit lower specific energy.

1.2.2 Cathode materials with the spinel structure

The first material with the spinel structure identified as a cathode material was $LiMn_2O_4$[16]. Manganese is substantially cheaper than cobalt and not toxic. Therefore it attracted interest as a potential replacement for $LiCoO_2$. As shown in figure 1-4, the spinel structure has the 16d octahedral sites occupied by manganese ions, the 32e sites occupied by oxygen ions and the tetrahedral 8a site occupied by lithium ions. Generally, materials with spinel structure give high operating voltage above 4V. $Li_2FeMn_3O_8$ was even reported to exhibit a 5V operating voltage[17]. Moreover, the 3D host structure results in good structural stability. However, the capacity fades during charge-discharge cycling or high temperature operating due to manganese dissolution from $LiMn_2O_4$[18].

1.2.3 Cathode materials with the olivine structure

In recent years a new type of materials, lithium transition metal phosphates, which exist in the olivine structure have become favoured due to their low cost, high safety, non-toxicity and long cycle-life. $LiFePO_4$ is the prototype of this type of material[19].

The olivine structure is shown in figure 1-4. The structure has an orthorhombic unit cell containing four formula units with space group *Pnma*. Transition metals locate at octahedral sites and lithium ions move in the 1D channel. The rigid PO_4^{3-} tetrahedral polyanion is composed of 4 strong covalent O – P bonds. There are two main advantages of such a strong poly-anion unit. First, it eliminates the problem of oxygen evolution and makes the material stable even under harsh conditions such as high temperature or overcharge and therefore suitable for the use in hybrid automobiles. Second, the host structure remains intact even at low Li content and hence gives rise to exceptionally long cycling life. The main obstacle in materials with the olivine structure is the low electronic conductivity because the distance between transition metals is large, unlike edge sharing MO_6 octahedra in layered $LiMO_2$ which results in better electronic conductivity due to the smaller M-M distance. Nevertheless this problem can be solved by reducing the particle size[20] or carbon coating[21]. Recently a material based on $LiFePO_4$ has been reported to display an ultrafast charging discharging rate[22]. The full discharged process in 10-20 seconds was achieved.

1.3 Previous theoretical studies on cathode materials

Computer simulations have been widely used to investigate properties of cathode materials from structures, voltages and lithium mobilities. The effect of transition metal ion M and anion X on the structure and average intercalation voltage in layered-$LiMO_2$[23-25], olivine-$LiMXO_4$ (X=Ge, Si, Sb, As, P)[25, 26] has been systematically studied. As shown in figure 1-5, a good agreement between the calculated values and experiments is obtained. Also a correlation between voltage and electronegativity of X is observed which can be used to alter the character of M-O bonding and tune the lithium insertion voltage. As one theoretical study[24] on layer-$LiMO_2$ suggests, charge transfer between M-O during Li deintercalation has a strong influence on voltage.

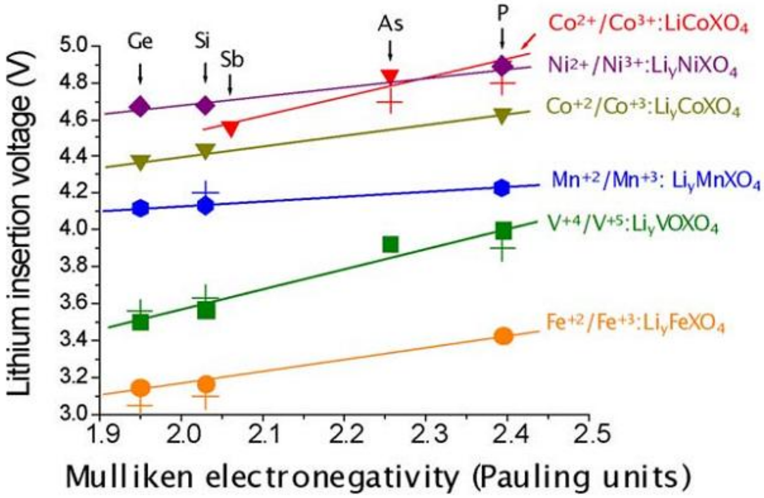

Figure 1-5: Calculated average lithium intercalation voltage compared to experimental results (crosses) for various polyoxianionic compounds[26].

Another important factor for a material to function as a cathode material is the Li mobility. Li mobility in layered-$LiMO_2$[27-29], olivine-$LiMPO_4$[30, 31] and spinel-LiM_2O_4[32] has also been extensively studied by theoretical calculations. Figure 1-6 shows the predicted lithium diffusion pathway in different structures and the activation energy for lithium migration. It is shown that in layered-$LiMO_2$, the lithium slab distance is the main factor that influences lithium diffusion[27]. As shown in figure 1-7, when the lithium slab distance is larger, the activation energy is lower and vice versa. This can be easily understood. Since the space between lithium slabs is the lithium diffusion channel, the large the space the easier for lithium to move.

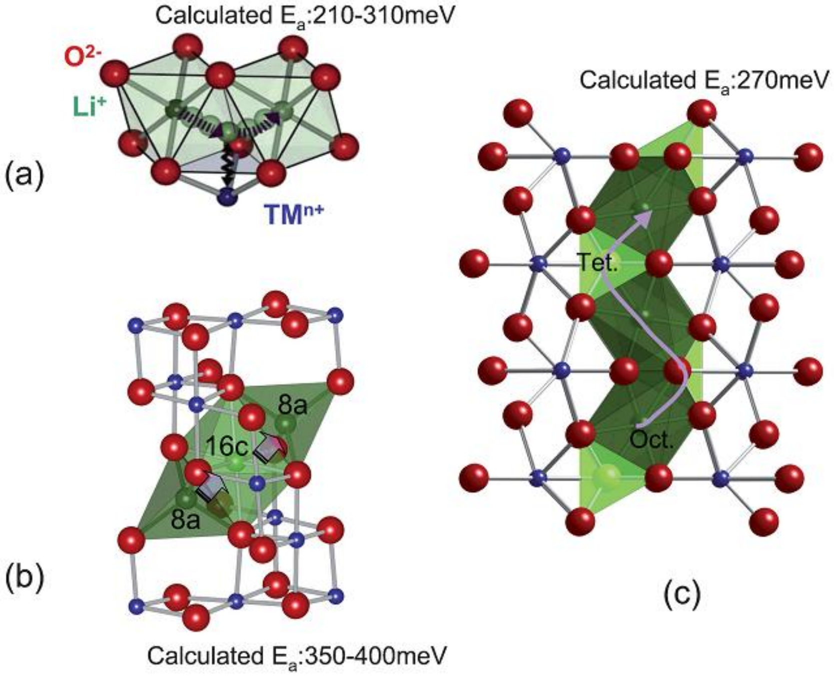

Figure 1-6: The lithium diffusion paths in lithium transition oxides.(a) layered structure (b)spinel structure (c)olivine structure[1].

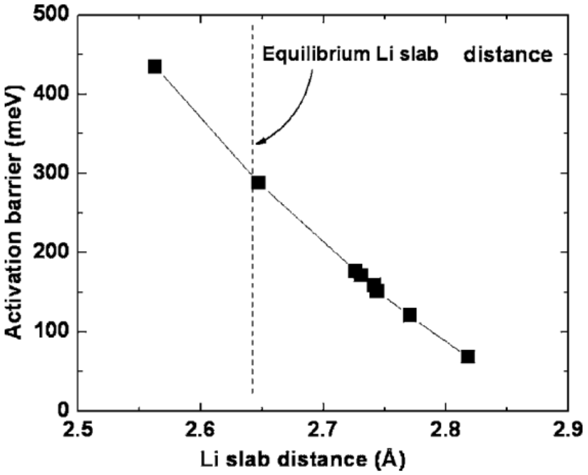

Figure 1-7: Activation barrier for lithium migration as a function of lithium slab distance[27].

1.4 Motivation and objectives

Over the past decade, there has been a growing interest in olivine-structured $LiFePO_4$ as a cathode material over layered rocksalt $LiMO_2$. Because $LiFePO_4$ shows excellent cyclability, it is cheaper and, most importantly, safer. Nevertheless from Table 1-1, we can see that materials with layered rocksalt structure still have better performance in terms of capacity and energy density. If the safety issue of layered rocksalt $LiNiO_2$ materials can be resolved, they it be a better choice. The most serious problem of layered $LiNiO_2$ as a potential cathode material is thermal instability, which is directly related to the safety of a battery. Experimentally this can now be mitigated by cationic substitution. For example, aluminium substitution in $LiNiO_2$ has given great improvements in thermally stability[33] and cyclability[34] which makes $LiNiO_2$-based compounds still promising cathode materials.

Table 1-1: Main features of most common cathode materials[35].

Features	$LiCoO_2$	$LiNiO_2$	$LiMn_2O_4$	$LiFePO_4$
Structure	Layered rock-salt	Layered rock-salt	Spinel	Olivine
Nominal voltage(V)	3.6	4.0	3.9	3.5
Specific capacity (mA.h.g^{-1})*	274	274	148	170
Discharge capacity (mA.h.g^{-1})**	145	160	105	155
Specific energy (Wh kg^{-1})	520	640	410	540
Energy density (Wh L^{-1})	2650	3070	1720	1940
Safety	Fair	Poor	Good	Good
Environmental friendliness	Poor	Fair	Good	Good
Availability	Low	Fair	High	High
Cost	High	Fair	Low	Low

*Theoretical , **Observed

In this thesis we therefore focus on $LiNiO_2$-based layered cathode materials. The main objective is to investigate the effect of cation substitution on structural imperfection and oxygen non-stoichiometry. Once we know how to control the structural stability of the material and prevent oxygen loss, then we can make batteries with high performance and greater safety. In chapter 3, the crystal and electronic structures of

$LiNiO_2$ are first investigated in order to pave the way for the subsequent study on structural defects. A new possible ground state of $LiNiO_2$ is found which explains the unusual behaviour of this compound in which no long-range structural or magnetic ordering is observed. In chapter 4, we investigate the structural variation of $LiMO_2$ compounds with rock-salt structure. The exchange interaction between transition metal ions is found to be responsible for the cation arrangement. In chapter 5 the structural defects in $LiNiO_2$ based layered compounds are investigated. The effect of cationic substitution is explained. Finally in chapter 6, we summarise all results and discuss how all these simulation are going to help to design new cathode materials.

References

1. Meng, Y.S. and M.E. Arroyo-de Dompablo, *First principles computational materials design for energy storage materials in lithium ion batteries.* Energy & Environmental Science, 2009. **2**(6): p. 589-609.

2. Goodenough, J.B. and Y. Kim, *Challenges for Rechargeable Li Batteries* Chemistry of Materials, 2009. **22**(3): p. 587-603.

3. Thackeray, M., *Lithium-ion batteries: An unexpected conductor.* Nat Mater, 2002. **1**(2): p. 81-82.

4. Dahn, J.R., et al., *Thermal stability of* Li_xCoO_2, Li_xNiO_2 *and* λ-MnO_2 *and consequences for the safety of Li-ion cells.* Solid State Ionics, 1994. **69**(3–4): p. 265-270.

5. Kanno, R., et al., *Phase Relationship and Lithium Deintercalation in Lithium Nickel Oxides.* Journal of Solid State Chemistry, 1994. **110**(2): p. 216-225.

6. Peres, J.P., et al., *The relationship between the composition of lithium nickel oxide and the loss of reversibility during the first cycle.* Journal of Physics and Chemistry of Solids, 1996. **57**(6–8): p. 1057-1060.

7. de Picciotto, L.A., et al., *Structural characterization of delithiated* $LiVO_2$*.* Materials Research Bulletin, 1984. **19**(11): p. 1497-1506.

8. Myung, S.-T., et al., *Structural Investigation of Layered* $Li_{1-\delta}Mn_xCr_{1-x}O_2$ *by XANES and In Situ XRD Measurements.* Journal of The Electrochemical Society, 2003. **150**(12): p. A1560-A1568.

9. Koetschau, I., et al., *Orthorhombic* $LiMnO_2$ *as a High Capacity Cathode for Li-Ion Cells.* Journal of The Electrochemical Society, 1995. **142**(9): p. 2906-2910.

10. Tabuchi, M., et al., *Effect of Cation Arrangement on the Magnetic Properties of Lithium Ferrites* ($LiFeO_2$) *Prepared by Hydrothermal Reaction and Post-annealing Method.* Journal of Solid State Chemistry, 1998. **140**(2): p. 159-167.

11. Armstrong, A.R. and P.G. Bruce, *Synthesis of layered* $LiMnO_2$ *as an electrode for rechargeable lithium batteries.* Nature, 1996. **381**(6582): p. 499-500.

12. Shirane, T., et al., *Structure and physical properties of lithium iron oxide, $LiFeO_2$, synthesized by ionic exchange reaction.* Solid State Ionics, 1995. **79**(0): p. 227-233.

13. Komaba, S., et al., *Electrochemical intercalation activity of layered $NaCrO_2$ vs. $LiCrO_2$.* Electrochemistry Communications, 2010. **12**(3): p. 355-358.

14. Didier, C., et al., *Electrochemical Na-Deintercalation from $NaVO_2$.* Electrochemical and Solid-State Letters, 2011. **14**(5): p. A75-A78.

15. Ma, X., H. Chen, and G. Ceder, *Electrochemical Properties of Monoclinic $NaMnO_2$.* Journal of The Electrochemical Society, 2011. **158**(12): p. A1307-A1312.

16. Thackeray, M.M., et al., *Lithium insertion into manganese spinels.* Materials Research Bulletin, 1983. **18**(4): p. 461-472.

17. Kawai, H., et al., *Novel 5 V Spinel Cathode $Li_2FeMn_3O_8$ for Lithium Ion Batteries.* Chemistry of Materials, 1998. **10**(11): p. 3266-3268.

18. Aoshima, T., et al., *Mechanisms of manganese spinels dissolution and capacity fade at high temperature.* Journal of Power Sources, 2001. **97-98**: p. 377-380.

19. Padhi, A.K., K.S. Nanjundaswamy, and J.B. Goodenough, *Phospho-olivines as Positive-Electrode Materials for Rechargeable Lithium Batteries.* Journal of The Electrochemical Society, 1997. **144**(4): p. 1188-1194.

20. Yamada, A., S.C. Chung, and K. Hinokuma, *Optimized $LiFePO_4$ for Lithium Battery Cathodes.* Journal of The Electrochemical Society, 2001. **148**(3): p. A224-A229.

21. Huang, H., S.C. Yin, and L.F. Nazar, *Approaching Theoretical Capacity of $LiFePO_4$ at Room Temperature at High Rates.* Electrochemical and Solid-State Letters, 2001. **4**(10): p. A170-A172.

22. Kang, B. and G. Ceder, *Battery materials for ultrafast charging and discharging.* Nature, 2009. **458**(7235): p. 190-193.

23. Aydinol, M.K., A.F. Kohan, and G. Ceder, *Ab initio calculation of the intercalation voltage of lithium-transition-metal oxide electrodes for rechargeable batteries.* Journal of Power Sources, 1997. **68**(2): p. 664-668.

24. Aydinol, M.K., et al., *Ab initio study of lithium intercalation in metal oxides and metal dichalcogenides.* Physical Review B, 1997. **56**(3): p. 1354-1365.

25. Chevrier, V.L., et al., *Hybrid density functional calculations of redox potentials and formation energies of transition metal compounds.* Physical Review B. **82**(7): p. 075122.

26. Arroyo-de Dompablo, M.E., et al., *On-demand design of polyoxianionic cathode materials based on electronegativity correlations: An exploration of the Li_2MSiO_4 system (M = Fe, Mn, Co, Ni).* Electrochemistry Communications, 2006. **8**(8): p. 1292-1298.

27. Kang, K. and G. Ceder, *Factors that affect Li mobility in layered lithium transition metal oxides.* Physical Review B, 2006. **74**(9): p. 094105.

28. Van der Ven, A., et al., *First-principles theory of ionic diffusion with nondilute carriers.* Physical Review B, 2001. **64**(18): p. 184307.

29. Van der Ven, A. and G. Ceder, *Lithium diffusion mechanisms in layered intercalation compounds.* Journal of Power Sources, 2001. **97-98**(0): p. 529-531.

30. Islam, M.S., et al., *Atomic-Scale Investigation of Defects, Dopants, and Lithium Transport in the $LiFePO_4$ Olivine-Type Battery Material.* Chemistry of Materials, 2005. **17**(20): p. 5085-5092.

31. Morgan, D., A. Van der Ven, and G. Ceder, *Li Conductivity in $L_{ix}MPO_4$ (M=Mn, Fe,Co, Ni) Olivine Materials.* Electrochemical and Solid-State Letters, 2004. **7**(2): p. A30-A32.

32. Xu, B. and S. Meng, *Factors affecting Li mobility in spinel $LiMn_2O_4$ - A first-principles study by GGA and GGA+U methods.* Journal of Power Sources. **195**(15): p. 4971-4976.

33. Guilmard, M., et al., *Thermal Stability of Lithium Nickel Oxide Derivatives. Part I: $Li_xNi_{1.02}O_2$ and $Li_xNi_{0.89}Al_{0.16}O_2$ (x = 0.50 and 0.30).* Chemistry of Materials, 2003. **15**(23): p. 4476-4483.

34. Guilmard, M., et al., *Effects of aluminum on the structural and electrochemical properties of $LiNiO_2$.* Journal of Power Sources, 2003. **115**(2): p. 305-314.

35. Reeves, N., *Novel cathode and anode for rechargeable Lithium-ion batteries*, Unpublished thesis, Department of Engineering Materials, The University of Sheffield.

Chapter 2

Ab initio simulation methods

2.1 Introduction

Matter is a collection of nuclei and electrons. In principle by studying the behaviours of these particles, all chemical and physical properties of a material can be understood. Quantum mechanics tells us that the Schrodinger equation is the fundamental equation that governs the behaviour of particles. However solving the many-body Schrodinger equation is a formidable task. Many theories have been developed to deal with the quantum mechanical many-body problem, from the early simple Hartree self-consistent field approach, the ensuing Hartree-Fock theory to the currently widely used density functional theory[1, 2]. The development of advanced theories along with the rapid progress in computing power has made computer simulation more and more important in the field of materials science. Insights into materials properties at the atomic and molecular level that are not always attainable from experiments can therefore be gained through theoretical calculations.

2.2 Quantum Mechanical Many Body Problems

For a non-relativistic quantum system, its stationary properties can be obtained by solving the time-independent Schrodinger equation

$$\boldsymbol{H}\Psi = E\Psi \tag{2-1}$$

where Ψ is the many-body wavefunction of the system and the Hamiltonian $\boldsymbol{H}$ has the following form

$$\begin{aligned}\boldsymbol{H} = -\frac{\hbar^2}{2m_e}\sum_i \nabla_i^2 + \sum_{i,I}\frac{Z_I e^2}{|\boldsymbol{r}_i - \boldsymbol{R}_I|} + \frac{1}{2}\sum_{i\neq j}\frac{e^2}{|\boldsymbol{r}_i - \boldsymbol{r}_j|} \\ - \sum_I \frac{\hbar^2}{2M_I}\nabla_I^2 + \frac{1}{2}\sum_{I\neq J}\frac{Z_I Z_J e^2}{|\boldsymbol{R}_I - \boldsymbol{R}_J|}\end{aligned} \tag{2-2}$$

where electrons, denoted by lower case letters, have mass m_e, charge e and position $\boldsymbol{r}_i$ and nuclei, denoted with capital letters, have masses M_I, charges Z_I and positions $\boldsymbol{R}_I$. The Hamiltonian contains the kinetic energies of both electrons and nuclei, the Coulomb interactions between electrons and nuclei, the electron-electron Coulomb interactions and the nuclei-nuclei Coulomb interactions. Once the wavefunction is known, any physical observable can then be obtained as the expectation value from a corresponding operator ***O*** acting on the wavefunction.

$$\langle \boldsymbol{O} \rangle = \frac{\langle \Psi | \boldsymbol{O} | \Psi \rangle}{\langle \Psi | \Psi \rangle} \qquad (2\text{-}3)$$

However, when the system contains more than two particles, the Schrodinger equation cannot be solved analytically. Many approximations need to be made to tackle a given many-body quantum mechanical problem.

2.3 The Born-Oppenheimer approximation [3]

The first of many approximations in the calculation of a many-body system is called the Born-Oppenheimer approximation. Because the mass of nuclei is a thousand times greater than electrons, the response of electrons to nuclear movements can be regarded as instantaneous. Therefore the nuclei positions are seen as fixed and used as input parameters which generate a static external potential. As a result, the wavefunctions of electrons and nuclei can be decoupled.

$$\Psi(\boldsymbol{r}, \boldsymbol{R}) = \varphi(\boldsymbol{r}; \boldsymbol{R}) \phi(\boldsymbol{R}) \qquad (2\text{-}4)$$

Also, the kinetic energy of nucleus can be neglected from the Hamiltonian and the last term in equation 2-2 is only a constant. Now the full Hamiltonian is reduced to the "electronic Hamiltonian"

$$\boldsymbol{H}_e = -\frac{\hbar^2}{2m_e}\sum_i \nabla_i^2 + \sum_{i,I}\frac{Z_I e^2}{|\boldsymbol{r}_i - \boldsymbol{R}_I|} + \frac{1}{2}\sum_{i\neq j}\frac{e^2}{|\boldsymbol{r}_i - \boldsymbol{r}_j|}$$

(2-5)

$$= \boldsymbol{T} + \boldsymbol{V} + \boldsymbol{U}$$

where $\boldsymbol{T}$ is the kinetic energy operator, $\boldsymbol{V}$ is the external potential and $\boldsymbol{U}$ is the electron-electron interaction. This simplifies the original problem to

$$\boldsymbol{H}_e\varphi(\boldsymbol{r};\boldsymbol{R}) = E_e\varphi(\boldsymbol{r};\boldsymbol{R}) \tag{2-6}$$

Even though the number of variables in the equation is greatly reduced, at this point there is still no hope of dealing with a real material by direct solving the wavefunction of the system.

2.4 Density functional theory

2.4.1 The Hohenberg-Kohn theorems [4]

The intuitive procedure to study a system is usually that – with a known external potential we solve the Schrödinger equation to obtain wave functions and then by applying appropriate operators to wave functions we can acquire all physical properties. The wave functions are apparently the centre of the scheme. Nonetheless, in 1964 from the Hohenberg-Kohn theorems a totally different concept emerged.

The first Hohenberg-Kohn theorem states that the external potential $V_{ext}(\mathbf{r})$ is a unique functional of its ground state electron density $n(\mathbf{r})$, except for a constant, for any system. Consequently all properties of the system are determined by the ground state electron density $n(\mathbf{r})$, since the Hamiltonian is uniquely determined by the external potential $V_{ext}(\mathbf{r})$. Therefore instead of the complicated many-body wavefunction, the ground state electron density $n(\mathbf{r})$ serves as the central variable of a problem. To prove this theorem, let us assume that there are two different external potentials $V_{ext}^{(1)}(\boldsymbol{r})$ and $V_{ext}^{(2)}(\boldsymbol{r})$ which give rise to two different Hamiltonians, $\boldsymbol{H}^{(1)}$ and $\boldsymbol{H}^{(2)}$, two different ground state wavefunctions $\Psi^{(1)}$ and $\Psi^{(2)}$ and two different ground state energies $E^{(1)}$ and $E^{(2)}$, but the same ground state electron density $n(\boldsymbol{r})$. It then follows that

$$\begin{aligned} E^{(1)} &= \langle \Psi^{(1)} \middle| \boldsymbol{H}^{(1)} \middle| \Psi^{(1)} \rangle < \langle \Psi^{(2)} \middle| \boldsymbol{H}^{(1)} \middle| \Psi^{(2)} \rangle \\ &= \langle \Psi^{(2)} | \boldsymbol{H}^{(2)} | \Psi^{(2)} \rangle + \langle \Psi^{(2)} | \boldsymbol{H}^{(1)} - \boldsymbol{H}^{(2)} | \Psi^{(2)} \rangle \end{aligned} \tag{2-7}$$

so that

$$E^{(1)} < E^{(2)} + \int \left[V_{ext}^{(1)}(\boldsymbol{r}) - V_{ext}^{(2)}(\boldsymbol{r}) \right] n(r) \mathrm{d}\mathbf{r}, \tag{2-8}$$

and similarly

$$E^{(2)} < E^{(1)} + \int \left[V_{ext}^{(2)}(\boldsymbol{r}) - V_{ext}^{(1)}(\boldsymbol{r}) \right] n(r) \mathrm{d}\mathbf{r} \tag{2-9}$$

The addition of the above two inequalities leads to a contradiction

$$E^{(1)} + E^{(2)} < E^{(1)} + E^{(2)} \tag{2-10}$$

Thus two different external potentials cannot possibly result in the same ground state electron density.

From the second Hohenberg-Kohn theorem, there is a universal functional F[n], which is the same for any electron system, that ground state energy E[n] can be written as

$$E[n] \equiv \int V_{ext}(\boldsymbol{r})n(\boldsymbol{r}) + F[n] \tag{2-11}$$

and

$$F[n] \equiv \langle\Psi|\boldsymbol{T} + \boldsymbol{U}|\Psi\rangle \tag{2-12}$$

It is known that the energy of a system is lowest in its ground state with its ground state wavefuntion Ψ. Now if the system is in any other arbitrary state Ψ', which is the ground state associated with another different external potential $V'_{ext}(\boldsymbol{r})$ and $\boldsymbol{H}'$ but not the ground state associated with $V_{ext}(\boldsymbol{r})$ and $\boldsymbol{H}$. It then follows that

$$\begin{gathered} E[\Psi'] = \int V_{ext}(\boldsymbol{r})n'(\boldsymbol{r}) + F[n'] = \langle\Psi'|\boldsymbol{H}|\Psi'\rangle \\ > \langle\Psi|\boldsymbol{H}|\Psi\rangle = \int V_{ext}(\boldsymbol{r})n(\boldsymbol{r}) + F[n] = E[\Psi] \end{gathered} \tag{2-13}$$

There the energy obtained from the above definition is indeed a minimum with the ground state electron density $n(\boldsymbol{r})$. Now if $F[n]$ is known, then by minimising the energy of the system the ground state electron density and energy can be found (Variational principle). Unfortunately, the form of $F[n]$ is still currently unknown.

2.4.2 The Kohn-Sham Approach[5]

For a non-interacting system described by the following single-particle equation,

$$\left\{-\frac{\hbar^2}{2m}\nabla^{\mathbf{2}}+V_f(\boldsymbol{r})\right\}\varphi_i=\varepsilon_i\varphi_i \tag{2-14}$$

its ground state wavefunction can be written as a Slater determinant of the solutions φ_i with the corresponding electron density

$$n(\boldsymbol{r})=\sum_{i=1}^{N}|\varphi_i(\boldsymbol{r})|^2 \tag{2-15}$$

and most importantly the kinetic energy of this non-interacting system can be expressed exactly as

$$T_s=-\frac{\hbar^2}{2m}\sum_{i=1}^{N}\langle\varphi_i|\nabla^2|\varphi_i\rangle. \tag{2-16}$$

Therefore if we can find a non-interacting system that produces the same electron density as the real interacting system, the kinetic energy can be calculated according to the above equation. But of course it is not the exact kinetic energy of the interacting system. Base on this, Kohn and Sham[5] then suggested that the energy functional $G[n]$ in the ground state energy of a real interacting system

$$E[n]=\int V_{ext}(\boldsymbol{r})n(\boldsymbol{r})+\frac{1}{2}\iint\frac{n(\boldsymbol{r})n(\boldsymbol{r}')}{|\boldsymbol{r}-\boldsymbol{r}'|}d\boldsymbol{r}d\boldsymbol{r}'+G[n] \tag{2-17}$$

takes the form

$$G[n] \equiv T_s[n] + E_{xc}[n] \tag{2-18}$$

where $T_s[n]$ is the kinetic energy of a fictitious non-interacting system with the same ground state electron density $n(\boldsymbol{r})$ and $E_{xc}[n]$ is defined as the exchange and correlation energy of the interacting system with density $n(\boldsymbol{r})$. The exchange-correlation functional $E_{xc}[n]$ accounts for the difference in kinetic energy between the real interacting system and the non-interacting system, as well as the non-classical electrostatic contribution from the electron-electron interaction of the real interacting system.

By substituting T_s with the expression of equation 2-16 and applying appropriate minimisation of $E[n]$ with respect to density $n(\boldsymbol{r})$, we can get

$$V_f(\boldsymbol{r}) = V_{ext}(\boldsymbol{r}) + \int \frac{n(\boldsymbol{r}')}{|\boldsymbol{r}-\boldsymbol{r}'|} d\boldsymbol{r}' + V_{XC}(\boldsymbol{r}) \tag{2-19}$$

where

$$V_{XC} = \frac{\delta E_{XC}[n]}{\delta n(\boldsymbol{r})} \tag{2-20}$$

is the exchange-correlation potential. Therefore, the single particle equation becomes

$$\left\{-\frac{\hbar^2}{2m}\nabla^2 + V_{ext}(\boldsymbol{r}) + \int \frac{n(\boldsymbol{r}')}{|\boldsymbol{r}-\boldsymbol{r}'|} d\boldsymbol{r}' + V_{XC}(\boldsymbol{r})\right\}\varphi_i = \varepsilon_i\varphi_i \tag{2-21}$$

This is the so-called Kohn-Sham equation. If the form of V_{XC}, or equivalently $E_{xc}[n]$, is known, the Kohn-Sham equation can then be solved self-consistently. Given an initial estimate of the ground state electron density, the effective potential in the Kohn-Sham equation can be constructed from equation 2-19. By solving the Kohn-Sham equation we can then compare the density calculated from the solutions equation from equation 2-17 with the initial density used to construct the effective potential. This procedure should be repeated until a self-consistent density is obtained, which is then the correct ground state electron density of the system. In summary, the Kohn-Sham approach maps an interacting many-body system to a non-interacting system with the same ground state electron density, which is a much simpler problem to handle mathematically. All the many-body effects are thrown into a "black box", the exchange-correlation term.

If the spin polarisation is considered, the electron density is decomposed into spin-up and spin-down components

$$n(\boldsymbol{r}) = n_{\uparrow}(\boldsymbol{r}) + n_{\downarrow}(\boldsymbol{r}) \tag{2-22}$$

with the total energy functional $E_{XC}[n_{\uparrow}, n_{\downarrow}]$.

The Kohn-Sham equation

$$\left\{-\frac{\hbar^2}{2m}\nabla^2 + V_{ext}(\boldsymbol{r}) + \int \frac{n(\boldsymbol{r}')}{|\boldsymbol{r}-\boldsymbol{r}'|} d\boldsymbol{r}' + V_{XC}^{\sigma}(\boldsymbol{r})\right\}\varphi_i^{\sigma} = \varepsilon_i^{\sigma}\varphi_i^{\sigma} \qquad \sigma = \uparrow, \downarrow \tag{2-23}$$

is then solved separately for the spin-up and spin-down electrons with their corresponding exchange-correlation potentials

$$V_{XC}^{\uparrow} = \frac{\delta E_{XC}[n_{\uparrow}, n_{\downarrow}]}{\delta n_{\uparrow}(\boldsymbol{r})} \tag{2-24}$$

and

$$V_{XC}^{\downarrow} = \frac{\delta E_{XC}[n_{\uparrow}, n_{\downarrow}]}{\delta n_{\downarrow}(\boldsymbol{r})} \tag{2-25}$$

The introduction of the additional degrees of freedom of spins often results in multiple self-consistent solutions of the spin-polarised Kohn-Sham equation which correspond to different stable spin configurations. Hence all possible spin configurations should be considered in order to find the real ground state.

2.4.3 Exchange and correlation functionals

So far no exact exchange and correlation energy functional has been found. All current used functionals are approximations and therefore fail in some circumstances because they do not capture the non-locality that the true exchange-correlation functional should possess, i.e. the exchange-correlation energy should be not expressed simply as a sum over electron density at each point ***r*** and instead it should contain a non-local object that includes the effect of the electron density at ***r’***.

The two most commonly adopted functional forms are LDA (Local Density Approximation) and GGA (Generalised Gradient Approximation). In LDA, the main idea is to treat the inhomogeneous electron as locally homogeneous. That means the exchange-correlation energy at each point depends only on the electron density at the same point. So the exchange-correlation energy for a system with density n(r) is given by

$$E_{xc}^{LDA} = \int n(\boldsymbol{r})\epsilon_{xc}(n_{\uparrow}, n_{\downarrow})\, d\boldsymbol{r} \tag{2-26}$$

where ϵ_{xc} is the exchange-correlation energy density. We then take the well developed form of ϵ_{xc} derived for a homogeneous electron gas. The exact form of the exchange part of ϵ_{xc} of the homogeneous gas can be obtained from the Hartree-Fock theory and the correlation part of ϵ_{xc} has been accurately calculated from Monte-Carlo simulations [6]. Since LDA assumes the local energy depends only on local density (locality), it works badly on systems with rapid change in electron density, such as isolated atoms or small molecules.

To address the issue of inhomogeneities in the electron density, the idea of GGA is that in addition to the dependence on the local density, the gradient of the local density should also be taken into consideration. The GGA functional takes the form

$$E_{XC}^{GGA}[n_{\uparrow}, n_{\downarrow}] = \int n(\boldsymbol{r})\, \epsilon_{xc}^{GGA}[n_{\uparrow}(\boldsymbol{r}), n_{\downarrow}(\boldsymbol{r}), \nabla n_{\uparrow}(\boldsymbol{r}), \nabla n_{\downarrow}(\boldsymbol{r})]\, d\boldsymbol{r} \tag{2-27}$$

Several different forms of GGA functional have been developed and gained success over the LDA functional[7, 8]. As shown in figure 2-1, generally LDA underestimates bulk lattice constants. Another well-known problem with LDA is the overestimate of binding energies which could be as large as several eV. This is greatly improved by the use of GGAs[9].

A notorious problem in both LDA and GGAs is the underestimate of band gaps in insulators. This can be attributed to that the lack of non-locality of LDA and GGAs and therefore it can be improved by functional with better treatment of the non-local exchange such as the hybrid functionals, to be introduced below. Also, since the dispersion interaction is a dynamical, inherently non-local correlation effect, for the same reason that neither LDA nor GGA functionals can describe Van der Waals systems well.

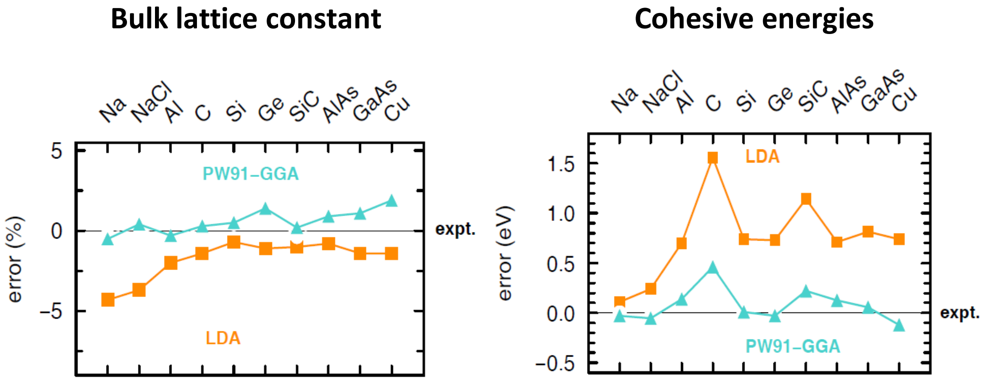

Figure 2-1: Comparison of the performance of the LDA and GGA functionals. Image courtesy of Dr. Martin Fuchs, Fritz-Haber-Institute der MPG.

2.5 Treatments for strongly correlated systems

Although density functional theory has gained great success, it is well known that by employing the LDA or GGA approximation functional it gives incorrect descriptions of transition metal compounds. In the Hartree-Fock theory, the electron exchange is precisely dealt with by the use of a single Slater determinant(*) but the electron correlation is not accounted for. The correlation energy, the difference between Hartree-Fock energy and the exact energy, in transition metal oxides is usually large and therefore these materials are termed "strongly correlated." As a result, many wide gap magnetic insulators are predicted to be metallic or small gap semiconductors with underestimated magnetic moments.

The failure of the standard DFT to describe these systems originates from the so-called self-interaction-error. Considering a one electron system, it is obvious that the single electron cannot exert electrostatic potential on itself. However the Hartree energy (Coulomb interaction) from the Kohn-Sham formalism reads

$$\frac{1}{2}\int \frac{n(\boldsymbol{r})n(\boldsymbol{r}')}{|\boldsymbol{r}-\boldsymbol{r}'|}d\boldsymbol{r}d\boldsymbol{r}' \neq 0 \qquad (2\text{-}28)$$

which is clearly nonzero, as if the electron interacts with itself. If the exact exchange-correlation functional were known, by the definition "exact" it would cancel this self-interaction which makes the total electron interaction vanish in such electron system. However the LDA and GGA approximations fail to do so. Consequently the electrons tend to be over delocalised spatially[10]. This spurious self-interaction error is especially pronounced in strongly-correlated systems such as 3d transition metal compounds due to the spatially localised nature of 3d electron states.

---

*As a result of exact exchange, the self-interaction error is zero.

2.5.1 The DFT+U method

The DFT+U method was originally proposed to give a better description of strongly correlated systems such as first row transition metal oxides[11]. It is known that the Hubbard model[12] works well in describing strongly correlated systems. In the Hubbard model, the strongly correlated d electrons are subjected on-site coulomb repulsions and U is the energy cost to place two electrons at the same site:

$$U \equiv E(d^{n+1}) + E(d^{n-1}) - 2E(d^{n}) \tag{2-29}$$

The behaviour of electrons can be crudely regarded as a competition between the kinetic energy t and the on-site coulomb energy U. When t is greater than U, electrons can hop between sites and are hence itinerant. When U is greater than t, electrons are localised and insulating. The metal-insulator transition in some transition metal oxides and the insulating behaviour of Mott insulator are correctly described based on the Hubbard Model.

The main idea of the DFT+U method is to incorporate an orbital dependent, Hubbard-model like energy correction parameter U in the standard DFT method. Electrons are separated into two subsystems. The localised electrons *i* (3d or 4f) are described by the Hubbard term and the less localised electrons (s and p) are described by the original DFT term. The energy functional then takes the form:

$$
\begin{aligned}
E^{DFT+U}[n] &= E^{DFT}[n] + E^{Hubbard}[n_i] - E^{dc}[n_i] \\
&= E^{DFT}[n] + \frac{U}{2}\sum_{i\neq j} n_i n_j - \frac{1}{2}UN(N-1)
\end{aligned}
\tag{2-30}
$$

where $N = \sum_i n_i$ and $E^{dc}[n_i]$ is called the "double counting term", which is the average Coulomb energy of localised electrons *i*, and must be deducted because the contribution from localised electrons is counted twice, both in E^{DFT} and $E^{Hubbard}$.

By taking into account exchange interaction and adopting rotationally invariant formulation, Dudarev et al.[13] proposed the practical form

$$
\begin{aligned}
E^{DFT+U} &= E^{DFT} + \frac{U-J}{2}\sum_{\sigma} Tr[\rho^{\sigma} - \rho^{\sigma}\rho^{\sigma}] \\
&= E^{DFT} + \frac{U_{eff}}{2}\sum_{\sigma} Tr[\rho^{\sigma} - \rho^{\sigma}\rho^{\sigma}]
\end{aligned}
\tag{2-31}
$$

where ρ^{σ} is the on-site density matrix of the d electrons which contains the information of the d orbital occupancies.

As a result of the introduction of U_{eff} term in DFT, partial occupations of orbitals, on which the U_{eff} term is applied, are discouraged. Considering a system doped with one electron/hole (defect state) in its N orbitals, where the U_{eff} term is applied, the energy of the electron/hole evenly distributing over N orbitals will then be higher than the electron/hole occupying one orbital with N-1 empty orbitals. In other words, the electron/hole is forced to localise as U_{eff} increases. Figure 2-2 shows the effect of applying U_{eff} to nickel d orbitals on the distribution of charge density of NiO. The 3d orbitals are clearly more localised with the application of U_{eff}.

The DFT+U method has been widely used in studying strongly-correlated systems. However up to now there is no satisfactory way to determine the value of U_{eff} in the DFT+U method. Although methods has been proposed to calculate the U_{eff} parameter[14-16], the most common way is to choose a value that gives reasonable experimental results such as lattice constants, magnetic moments, band gaps, etc.

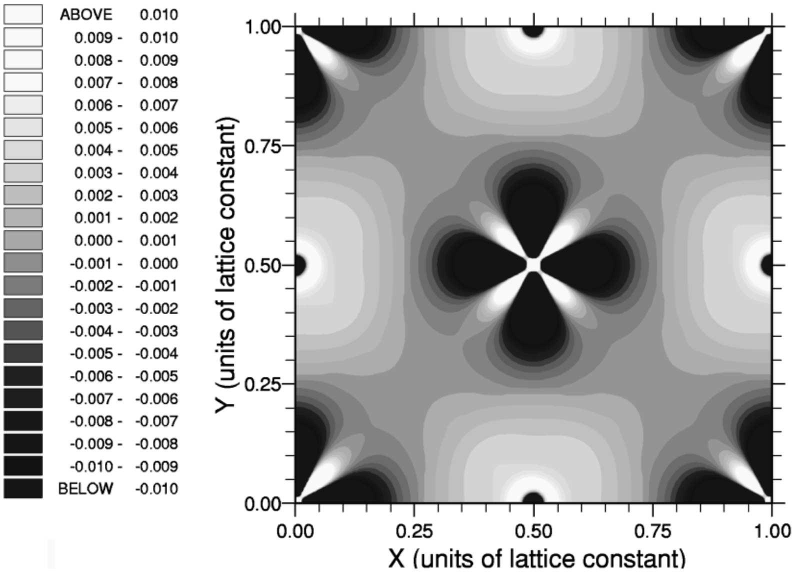

Figure 2-2: The difference between the charge density with and without U in the (100) plane of NiO [13]. Nickel is located at the centre of the figure.

2.5.2 Hybrid functionals

Because the self-interaction error is cancelled exactly in the Hartree-Fock approximation from its construction, hybrid functionals that mix a portion of exchange energy from Hartree-Fock theory with explicit exchange-correlation energy from DFT have been proposed as a way of overcoming the shortcomings of the LDA and GGA approximations. The exchange-correlation energy of a hybrid functional takes the form

$$E_{XC}^{hybrid} = \alpha E_X^{HF} + (1-\alpha)E_X^{DFT} + E_C^{DFT} \tag{2-32}$$

Unlike the DFT+U method in which the U_{eff} parameter is system dependent, the amount of HF exchange energy is an *a priori* fixed parameter in the hybrid functional method. Studies have shown that the mixing of 20-35 % of exchange energy give rise to good bulk properties of transition metal oxides such as lattice constants, band gaps, exchange coupling constants[17, 18]. Nonetheless the calculation of the Hartree-Fock exchange energy is computationally expensive which makes it less appealing for studying systems containing large number of particles.

To circumvent this problem, recently Heyd, Scuseria and Ernzerhof proposed to split the exchange energy of the PBE0 hybrid functional [19] into the long-range and short-range components and also showed that the long-range components contributes little to the total energy and thus can be neglected[20]. The resulting functional, called the HSE functional, then has the form

$$E_{XC}^{HSE} = \frac{1}{4}E_X^{HF,SR}(\mu) + \frac{3}{4}E_X^{PBE,SR}(\mu) + E_X^{PBE,LR}(\mu) + E_C^{PBE} \tag{2-33}$$

with μ defined in the following equation which splits the Coulomb operator into the long (right) and short range (left) parts

$$\frac{1}{r} = \frac{1 - erf(\mu r)}{r} + \frac{erf(\mu r)}{r} \tag{2-34}$$

where *erf* is the error function.

μ is called the range separating parameter determining the extent of short-range interactions. It was shown that the optimum value of μ is approximately 0.2-0.3 Å^{-1} in order to reproduce various properties of molecules and solids[20]. The exclusion of the long-range part of Hartree-Fock exchange greatly reduces computational cost and enables the study of extended systems such as crystalline solids or large molecules. The HSE functional has been proved to reproduce the localised nature of transition metal oxides pretty well give and is becoming popular for studying solid crystalline compounds[21, 22].

2.6 Solving the Kohn-Sham equation in practice

In order to solve the Kohn-Sham equation for real materials, some remaining problems need to be addressed. First, a material contains virtually an infinite number of electrons, how this can be dealt with? Second, a good mathematical representation of wavefunctions is required. Finally, how do we treat electron-nuclear interactions?

2.6.1 The Bloch theorem

A perfect solid crystalline material is composed of infinitely repeating unit lattice cells. Due to the periodicity of solid crystals, the potential arising from the coulomb interaction that the electrons feel is also periodic with the same periodicity as the crystal. The Bloch theorem states that in the presence of a periodic potential $V(\boldsymbol{r}) = V(\boldsymbol{r}+\boldsymbol{R})$, where $\boldsymbol{R} = n_1\boldsymbol{a_1} + n_2\boldsymbol{a_2} + n_3\boldsymbol{a_3}$ is the translation vector of the lattice and $\boldsymbol{a_1}$, $\boldsymbol{a_2}$, and $\boldsymbol{a_3}$ are lattice vectors of the primitive lattice, the following relation exists:

$$\Psi_{\boldsymbol{k}}(\boldsymbol{r}+\boldsymbol{R}) = e^{i\boldsymbol{k}\cdot\boldsymbol{R}}\Psi(\boldsymbol{r}) \qquad (2\text{-}35)$$

or the equivalent form

$$\Psi_{\boldsymbol{k}}(\boldsymbol{r}) = e^{i\boldsymbol{k}\cdot\boldsymbol{R}}u_{\boldsymbol{k}}(\boldsymbol{r}) \qquad (2\text{-}36)$$

where $u_{\boldsymbol{k}}(\boldsymbol{r})$ has the same periodicity as the potential $u_{\boldsymbol{k}}(\boldsymbol{r}+\boldsymbol{R})$ = $u_{\boldsymbol{k}}(\boldsymbol{r})$ and $\boldsymbol{k}$ is called the Bloch vector, arising from the translational symmetry.

The reciprocal lattice vector $\boldsymbol{G} = m_1\boldsymbol{b_1} + m_2\boldsymbol{b_2} + m_3\boldsymbol{b_3}$ is defined to fulfil the following relation

$$e^{i\boldsymbol{G}\cdot\boldsymbol{R}} = 1 \tag{2-37}$$

It then follows that

$$\Psi_{\boldsymbol{k}+\boldsymbol{G}}(\boldsymbol{r}+\boldsymbol{R}) = e^{i(\boldsymbol{k}+\boldsymbol{G})\cdot\boldsymbol{R}}\Psi_{\boldsymbol{k}+\boldsymbol{G}}(\boldsymbol{r}) = e^{i\boldsymbol{k}\cdot\boldsymbol{R}}\Psi_{\boldsymbol{k}+\boldsymbol{G}}(\boldsymbol{r}) \tag{2-38}$$

$$\Longrightarrow \quad \Psi_{\boldsymbol{k}+\boldsymbol{G}}(\boldsymbol{r}) = \Psi_{\boldsymbol{k}}(\boldsymbol{r}) \tag{2-39}$$

Therefore only wavefunctions in the first Brillouin zone need to be calculated, which is the volume defined by the primitive reciprocal lattice vector.

At this point, thanks to Bloch theorem the problem is simplified from the calculation of all electrons in the infinite solid to the calculation of a much smaller number of electrons in one unit cell, and the electron wavefunction in the neighbouring cell differs only by a phase factor $e^{i\boldsymbol{k}\cdot\boldsymbol{R}}$. In addition only wavefunctions in the first Brillouin zone in the k-space need to be considered. However, since ***k*** is continuous one still encounters the problem of an infinite number of ***k*** vectors, which is not computationally feasible.

Fortunately, the wavefunctions at ***k***-points close together in the first Brillouin zone are nearly identical. Consequently the wavefunctions at a single ***k***-point is representative of wavefunctions over a region. Now wavefunctions only need to be calculated for a finite number of ***k***-points. There are many methods developed to determine representative ***k***-points. One popular method proposed by Monkhorst and Pack[23] that chooses evenly distributed ***k***-points in the first Brillouin zone is used in all our calculations. Figure 2-3 illustrates the convergence behaviour of total energy with ***k***-points. In all our calculations, the numbers of ***k***-points are large enough to ensure good convergence and accurate results.

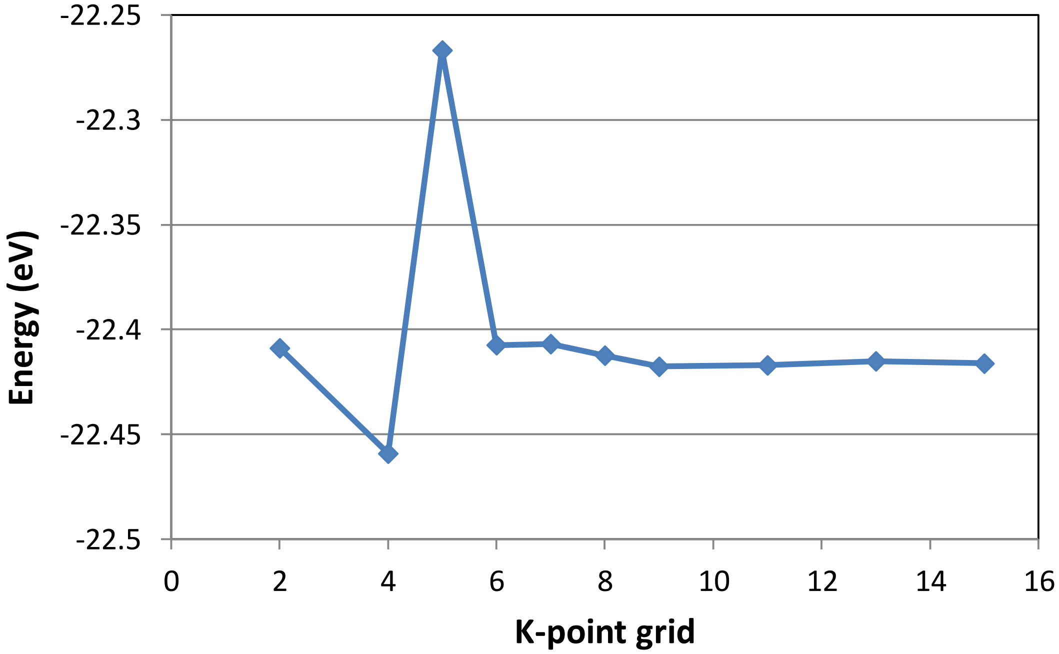

Figure 2-3: The convergence of $LiNiO_2$ total energy against ***k***-points.

2.6.2 Plane wave basis

According to the Bloch theorem, the wave function of electrons in a periodic potential can be expressed as

$$\Psi_{\boldsymbol{k}}(\boldsymbol{r}) = e^{i\boldsymbol{k}\cdot\boldsymbol{R}}u_{\boldsymbol{k}}(\boldsymbol{r}) \tag{2-40}$$

The periodic function $u_{\boldsymbol{k}}(\boldsymbol{r})$ can be naturally expanded with the discrete plane-wave basis (a Fourier series)

$$u_{\boldsymbol{k}}(\boldsymbol{r}) = \sum_{\boldsymbol{G}} C_{\boldsymbol{k}}(\boldsymbol{G})e^{i\boldsymbol{G}\cdot\boldsymbol{r}} \tag{2-41}$$

where ***G*** are reciprocal lattice vectors corresponding to the real space crystal lattice vector ***R***.

The wavefunction is then written as a sum of plane waves

$$\Psi_{\boldsymbol{k}}(\boldsymbol{r}) = \sum_{\boldsymbol{G}} C_{\boldsymbol{k}}(\boldsymbol{G})e^{i(\boldsymbol{k}+\boldsymbol{G})\cdot\boldsymbol{r}} \tag{2-42}$$

In principle, an infinite number of plane-waves should be used to express exactly the wavefunction. However, the plane wave coefficient $C_{\boldsymbol{k}}(\boldsymbol{G})$ becomes more and more insignificant as |***K***+***G***| increases and the plane-wave expansion can be truncated by setting a cut-off kinetic energy of the plane-wave $E_{cut} = \left(\frac{\hbar^2}{2m}\right)|\boldsymbol{k}+\boldsymbol{G}|^2$. Figure 2-3 shows the convergence behaviour of total energy with respect to the cut-off energy of the plane-wave. A high cut-off energy is set for all our calculations to ensure good convergence and accurate results.

Apart from the plane wave basis set, there is another category of basis sets, localised basis sets. As suggested by the name, localised basis sets centred at atomic positions, such as atomic orbitals and Gaussian type functions. Nevertheless the choice of plane wave basis is favoured in studying systems with periodic boundary conditions. The main advantage of the plane wave basis is computational efficiency. Plane waves are more easily to be handled mathematically than other basis sets. Besides, the completeness of the plane wave basis set can be easily controlled and the convergence of properties can be systematically checked. Moreover, the plane wave basis is independent of atomic positions and the superposition errors arising from over-completeness of local basis sets are avoided.

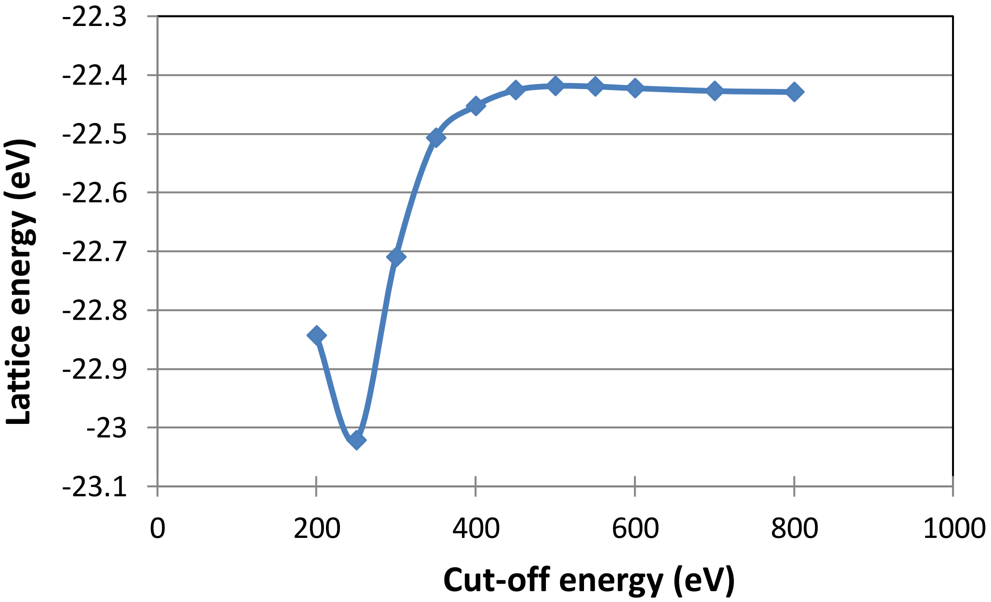

Figure 2-4: The convergence of $LiNiO_2$ total energy against plane-wave cut-off energy.

2.6.3 Pseudopotentials and the Projector-Augmented Wave Method

Due to the orthogonality between the core and valence electrons, the wave functions of valence electrons oscillate rapidly near the nucleus. A large number of plane waves is needed to represent such oscillation. Fortunately it is known that the core electrons do not contribute much in chemical bonding and are not sensitive to the surrounding environment. Theories have been developed to replace electron states by node-less wavefunctions that still give the same scattering properties and outside the core region, the pseudo-wavefunction and the true wavefunction are identical. This is the basic idea of pseudopotential as illustrated in figure 2-5. The main advantage of the pseudopotential method is that fewer plane waves are needed and therefore it is much more computationally efficient than solving the problem with the true potential. However the true wavefunction is not obtainable from the pseudopotential method.

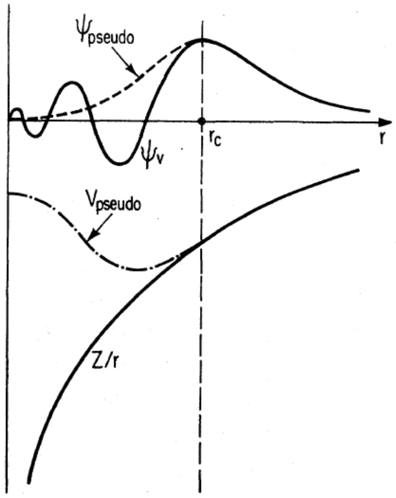

Figure 2-5: The solid lines represent the true potential and wave function and the dashed line represent the pseudopotential and pseudowavefuntion. Taken from [24]

The projector augmented wave (PAW) method was introduced by Bloch in 1994 [25]. This method starts from the search of a linear transformation $\mathbf{T}$ such that

$$|\Psi\rangle = \mathbf{T}\,|\widetilde{\Psi}\rangle \tag{2-43}$$

where $|\Psi\rangle$ is the true wavefunction and $|\widetilde{\Psi}\rangle$ is the pseudo wavefunction which is smooth with no oscillation near the nucleus. In order to keep$|\Psi\rangle$ and $|\widetilde{\Psi}\rangle$ identical outside certain cut-off radii $r_{c,\boldsymbol{R}}$ around atoms at positions $\boldsymbol{R}$, the transformation T should have the following form

$$\boldsymbol{T} = \boldsymbol{I} + \sum_{\boldsymbol{R}} \boldsymbol{T}_{\boldsymbol{R}} \tag{2-44}$$

where $\boldsymbol{I}$ is the unity operator and $\boldsymbol{T}_{\boldsymbol{R}}$ is an operator that acts only within spheres $|\boldsymbol{r}-\boldsymbol{R}| < r_{c,\boldsymbol{R}}$ around each atom at position $\boldsymbol{R}$**.** This is called the augmentation region.

Around each atom at ***R***, a set of local spherical waves, called partial waves, Φ_i is built with the index *i* containing the atomic position ***R*** and angular momentum quantum numbers *l*, *m*. The nature choice of partial waves Φ_i are solutions of the radial Schrodinger equation of isolated atoms. The operator $\boldsymbol{T}_{\boldsymbol{R}}$ is then defined from the following relation which makes a set of pseudo partial waves $\widetilde{\Phi}_i$ coincide with partial waves Φ_i outside the augmentation region.

$$|\Phi_i\rangle = (\boldsymbol{I} + \boldsymbol{T}_{\boldsymbol{R}})\,|\widetilde{\Phi}_i\rangle \tag{2-45}$$

$$\Rightarrow \boldsymbol{T}_{\boldsymbol{R}}|\widetilde{\Phi}_i\rangle = |\Phi_i\rangle - |\widetilde{\Phi}_i\rangle \tag{2-46}$$

If the set of pseudo partial waves $\widetilde{\Phi}_i$ is complete, then inside the augmentation region the pseudo wavefunction $|\widetilde{\Psi}\rangle$ can be expanded as

$$|\widetilde{\Psi}\rangle = \sum_i |\widetilde{\Phi}_i\rangle\, c_i \qquad (2\text{-}47)$$

From all the above relations, it follows

$$\begin{aligned} |\Psi\rangle &= \mathbf{T}|\widetilde{\Psi}\rangle \\ &= |\widetilde{\Psi}\rangle + \sum_{\boldsymbol{R}} \boldsymbol{T_R}\, |\widetilde{\Psi}\rangle \\ &= |\widetilde{\Psi}\rangle + \sum_i \boldsymbol{T_R}\, |\widetilde{\Phi}_i\rangle c_i \\ &= |\widetilde{\Psi}\rangle + \sum_i |\Phi_i\rangle\, c_i - \sum_i |\widetilde{\Phi}_i\rangle\, c_i \end{aligned} \qquad (2\text{-}48)$$

Since $\boldsymbol{T}$ is required to be linear and c_i are the coefficients of the expansion with Φ_i, they can be determined as

$$c_i = \langle \tilde{p}_i|\widetilde{\Psi}\rangle \qquad (2\text{-}49)$$

with the condition

$$\sum_i |\widetilde{\Phi}_i\rangle\langle \tilde{p}_i| = \boldsymbol{I} \qquad (2\text{-}50)$$

where $\tilde{p}_i$ are called projectors. Finally we arrive at

$$|\Psi\rangle = |\widetilde{\Psi}\rangle - \sum_i |\widetilde{\Phi}_i\rangle\, \langle \tilde{p}_i|\widetilde{\Psi}\rangle + \sum_i |\Phi_i\rangle\, \langle \tilde{p}_i|\widetilde{\Psi}\rangle \qquad (2\text{-}51)$$

and

$$\boldsymbol{T} = \boldsymbol{I} + \sum_i \left(|\Phi_i\rangle - |\widetilde{\Phi}_i\rangle \right) \langle \tilde{p}_i| \tag{2-52}$$

In summary, the PAW method divides the true electron wavefunction in to three components as illustrated in figure 2-6. By appropriate choice of the partial waves Φ_i, the pseudo-partial waves $\widetilde{\Phi}_i$ and the projectors $\tilde{p}_i$ around atoms, the linear transformation T is then defined and what is really calculated in practice from the Kohn-Sham equation is the pseudowavefunction $\widetilde{\Psi}$. Through the transformation T the true wavefunction Ψ can be obtained and so do all physical quantities. It can be shown that the norm-conserving and ultra-soft pseudopotentials are approximations of the PAW method. Therefore not only the all-electron wavefunction is accessible in the PAW method, its accuracy and efficiency are of the same order of the ultra-soft pseudopotential method or better.

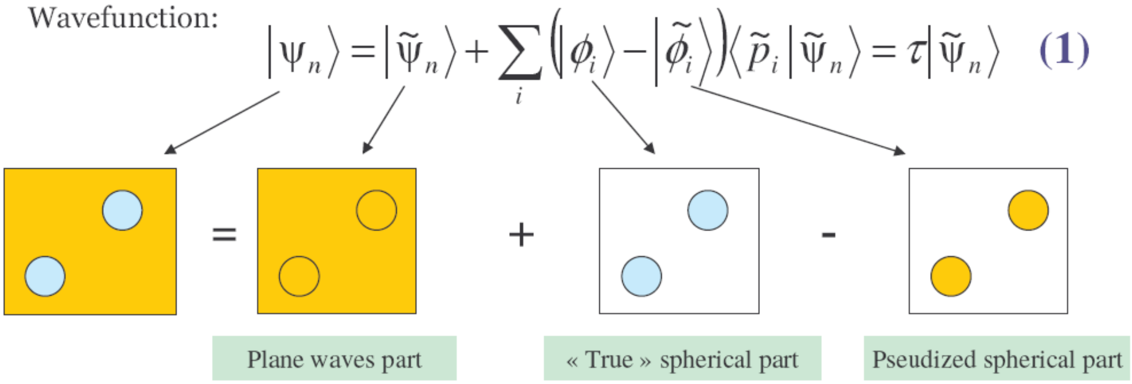

Figure 2-6: Schematic representation of the three components in the PAW method. Image courtesy of Dr. Marc Torrent, Département de Physique Théorique et Appliquée, Commissariat à l’Energie Atomique, Bruyères-le-Châtel.

2.7 Structural optimisation

The total energy in the density functional theory is a function of atomic positions $E(\boldsymbol{R}_1, \boldsymbol{R}_2, \cdots, \boldsymbol{R}_N)$. Finding the optimised structure can be achieved in principle simply by minimising the energy which is a function of atomic positions, $E(\boldsymbol{R}_1, \boldsymbol{R}_2, \cdots, \boldsymbol{R}_N)$. However it is not a simple task. There are various mathematical algorithms that can be used in the search of the minimum value of a function, such as the steep descent, conjugate gradient, Newton-Raphson method, to be introduced below. In density functional theory, the form of $E(\boldsymbol{R}_1, \boldsymbol{R}_2, \cdots, \boldsymbol{R}_N)$ is not attainable and therefore the knowledge about forces acting on ions (derivatives) needed in minimisation methods have to be calculated through the Hellmann-Feynman theorem[26, 27]. According to the theory, the force acting on an ion at position $\boldsymbol{R}_I$ can be written as

$$\boldsymbol{F}_I = -\frac{\partial E}{\partial \boldsymbol{R}_I} = -\int n(\boldsymbol{r}) \frac{\partial V_{ext}(\boldsymbol{r})}{\partial \boldsymbol{R}_I} d\boldsymbol{r} - \frac{\partial E_{II}}{\partial \boldsymbol{R}_I} \tag{2-53}$$

where $n(\boldsymbol{r})$ is the electron density, $V_{ext}(\boldsymbol{r})$ is the external potential and E_{II} is the Coulomb interaction between nuclei. This enables us to calculate the ionic forces (derivatives) from the ground state density $n(\boldsymbol{r})$ obtained from solving the Kohn-Sham equation. One point needs to be made here that when a localised basis set is used, the incompleteness of the basis gives rise to the so-called Pulay forces[28]. However the plane wave basis is independent of atomic positions and the error is zero. Every minimisation method has its pros and cons. An inappropriate choice of minimisation method could result in slow convergence or even divergence. Also, no minimisation method guarantees the global minimum. In some systems such as transition metal oxides there are many local minimums (meta-stable states), a subtle different initial configuration can lead to a different local minimum and therefore results should be explained with extreme care.

2.7.1 The steepest descent method

In this method, minimisation moves on the energy surface from a point $\boldsymbol{x}_n$ to the next point $\boldsymbol{x}_{n+1}$ along the direction where the function decreases most rapidly, which is the direction opposite to the gradient at point $\boldsymbol{x}_n$:

$$\boldsymbol{x}_{n+1} = \boldsymbol{x}_n + \lambda_n \boldsymbol{v}_n \tag{2-54}$$

where λ_n is the step size controlling how far one should go along that direction and the direction

$$\boldsymbol{v}_n = -\nabla E(\boldsymbol{x}) = -\boldsymbol{g}_n \tag{2-55}$$

λ_n can be determined by locating the lowest point on the direction, the line search in one dimension. First bracket the minimum by finding three points x_1, x_2 and x_3 that fulfil the relation $E(x_3)<E(x_1)$ and $E(x_2)$, this ensures that a minimum lie between x_1 and x_2. Then choose the next point x_4 in between x_1 and x_2 using a golden section and reject one of the outer points x_1 or x_2 which is not adjacent to that of x_3 and x_4 which has a lower energy. Repeat the same procedure until the minimum is reached.

In this steepest descent method, the minimisation direction in any step is only orthogonal to its previous one but not to any others and therefore later minimisation directions can undo the effect of earlier ones. This results in a large number of steps to reach the minimum when dealing with an energy surface with long narrow valleys.

2.7.2 The conjugate gradient method

The difference of the conjugate gradient method from the steepest descent method is that the conjugate directions are introduced as search directions. Two directions $\boldsymbol{v}_i$ and $\boldsymbol{v}_j$ are conjugate if they fulfil the relation

$$\boldsymbol{v}_i \cdot \left(\boldsymbol{A} \cdot \boldsymbol{v}_j\right) = 0 \tag{2-56}$$

where

$$\boldsymbol{A} \equiv \sum_{i,j} \frac{\partial^2 E}{\partial x_i x_j} \tag{2-57}$$

is called the Hessian matrix. It can be shown that the minimum of a quadratic function of n variables can be reached in exactly n steps by moving along a set of n conjugate directions.

To ensure the minimisation direction at point n is conjugate to all previous directions, it can be calculated according

$$\boldsymbol{v}_n = -\boldsymbol{g}_n + \gamma_n \boldsymbol{v}_{n-1} \tag{2-58}$$

where

$$\gamma_n = \frac{\boldsymbol{g}_n \cdot \boldsymbol{g}_n}{\boldsymbol{g}_{n-1} \cdot \boldsymbol{g}_{n-1}} \tag{2-59}$$

If a direction is conjugate to all its previous direction, it does not cancel the effect of any previous minimisation steps. Hence by deploying the conjugate gradient method, the number of steps in minimisation could be reduced compared to the steepest descent method when one is close to the minimum.

2.7.3 The Newton-Raphson method

In this method, the second order derivative (Hessian) of a function is also used in the search of the minimum. At the point x_0, a function can be approximated with a Taylor series to second order

$$E(\boldsymbol{x}) = E(\boldsymbol{x}_0) + (\boldsymbol{x} - \boldsymbol{x}_0)\nabla E(\boldsymbol{x}) + \frac{1}{2}(\boldsymbol{x} - \boldsymbol{x}_0)\boldsymbol{H}(\boldsymbol{x} - \boldsymbol{x}_0) \tag{2-60}$$

At the minimum point x_{min}, $\nabla E(\boldsymbol{x}_{min}) = 0$ and therefore

$$\boldsymbol{x}_{min} = \boldsymbol{x}_0 - \boldsymbol{H}^{-1}\nabla E(\boldsymbol{x}) \tag{2-61}$$

Obviously if the target function is quadratic, the minimum can be reached in one step. For functions containing terms beyond second order, the minimum is approached iteratively according to equation 2-61. Although the Newton-Raphson method gives rapid convergence, the calculation of the inverse Hessian matrix for large system can be very costly.

2.7.3 Quasi-Newton methods

In quasi-Newton methods, the inverse Hessian matrix is not calculated directly and instead an approximation $\boldsymbol{B}$ to the Hessian matrix is used. At a step *i*, it is chosen to satisfy the relation

$$\nabla E(\boldsymbol{x}_i + \Delta\boldsymbol{x}) = \nabla E(\boldsymbol{x}_i) + \boldsymbol{B}\Delta\boldsymbol{x} \tag{2-62}$$

In the popular Broyden-Fletcher-Goldfarb-Shanno (BFGS) approach, the approximated inverse Hessian matrix at the *i*th step $\boldsymbol{B}_i^{-1}$ is calculated according to

$$\begin{aligned}\boldsymbol{B}_i^{-1} = \boldsymbol{B}_{i-1}^{-1} &+ \frac{(\boldsymbol{x}_i - \boldsymbol{x}_{i-1}) \times (\boldsymbol{x}_i - \boldsymbol{x}_{i-1})}{(\boldsymbol{x}_i - \boldsymbol{x}_{i-1}) \cdot (\boldsymbol{g}_i - \boldsymbol{g}_{i-1})} \\ &- \frac{[\boldsymbol{B}_{i-1}^{-1} \cdot (\boldsymbol{g}_i - \boldsymbol{g}_{i-1})] \times [\boldsymbol{B}_{i-1}^{-1} \cdot (\boldsymbol{g}_i - \boldsymbol{g}_{i-1})]}{(\boldsymbol{g}_i - \boldsymbol{g}_{i-1}) \cdot \boldsymbol{B}_{i-1}^{-1} \cdot (\boldsymbol{g}_i - \boldsymbol{g}_{i-1})} \\ &+ [(\boldsymbol{g}_i - \boldsymbol{g}_{i-1}) \cdot \boldsymbol{B}_{i-1}^{-1} \cdot (\boldsymbol{g}_i - \boldsymbol{g}_{i-1})]\boldsymbol{u} \times \boldsymbol{u}\end{aligned} \tag{2-63}$$

where

$$\boldsymbol{u} = \frac{(\boldsymbol{g}_i - \boldsymbol{g}_{i-1})}{(\boldsymbol{g}_i - \boldsymbol{g}_{i-1}) \cdot (\boldsymbol{g}_i - \boldsymbol{g}_{i-1})} - \frac{[[\boldsymbol{B}_{i-1}^{-1} \cdot (\boldsymbol{g}_i - \boldsymbol{g}_{i-1})]}{(\boldsymbol{g}_i - \boldsymbol{g}_{i-1}) \cdot \boldsymbol{B}_{i-1}^{-1} \cdot (\boldsymbol{g}_i - \boldsymbol{g}_{i-1})} \tag{2-64}$$

The unit matrix $\boldsymbol{I}$ is often used as $\boldsymbol{B}_0$ and hence the first step is equivalent to the steepest descent method.

2.8 Vienna Ab-initio Simulation Package (VASP)[29, 30]

VASP is a package for performing ab-initio quantum mechanical calculations based on ultrasoft-pseudopotentials or the projector augmentation method, and a plane wave basis set. Methods for solving electronic structures introduced above are all implemented in VASP. All calculations in this thesis were carried out using VASP.

References

1. Martin, R.M., *Electronic Structure - Basic Theory and Practical Methods.* Cambridge University Press, 2004.

2. Kohanoff, J., *Electronic Structure Calculations for Solids and Molecules - Theory and Computational Methods.* Cambridge University Press, 2006.

3. Born, M. and R. Oppenheimer, *Zur Quantentheorie der Molekeln.* Annalen der Physik, 1927. **389**(20): p. 457-484.

4. Hohenberg, P. and W. Kohn, *Inhomogeneous Electron Gas.* Physical Review, 1964. **136**(3B): p. B864.

5. Kohn, W. and L.J. Sham, *Self-Consistent Equations Including Exchange and Correlation Effects.* Physical Review, 1965. **140**(4A): p. A1133-A1138.

6. Ceperley, D.M. and B.J. Alder, *Ground State of the Electron Gas by a Stochastic Method.* Physical Review Letters, 1980. **45**(7): p. 566-569.

7. Perdew, J.P. and Y. Wang, *Accurate and simple analytic representation of the electron-gas correlation energy.* Physical Review B, 1992. **45**(23): p. 13244.

8. Perdew, J.P., K. Burke, and M. Ernzerhof, *Generalized Gradient Approximation Made Simple.* Physical Review Letters, 1996. **77**(18): p. 3865.

9. Staroverov, V.N., et al., *Tests of a ladder of density functionals for bulk solids and surfaces.* Physical Review B, 2004. **69**(7): p. 075102.

10. Lundberg, M. and P.E.M. Siegbahn, *Quantifying the effects of the self-interaction error in DFT: When do the delocalized states appear?* The Journal of Chemical Physics, 2005. **122**(22): p. 224103-9.

11. Anisimov, V.I., J. Zaanen, and O.K. Andersen, *Band theory and Mott insulators: Hubbard U instead of Stoner I.* Physical Review B, 1991. **44**(3): p. 943-954.

12. Hubbard, J., *Electron Correlations in Narrow Energy Bands.* Proceedings of the Royal Society of London. Series A. Mathematical and Physical Sciences, 1963. **276**(1365): p. 238-257.

13. Dudarev, S.L., et al., *Electron-energy-loss spectra and the structural stability of nickel oxide: An LSDA+U study.* Physical Review B, 1998. **57**(3): p. 1505-1509.

14. Kulik, H.J., et al., *Density Functional Theory in Transition-Metal Chemistry: A Self-Consistent Hubbard U Approach.* Physical Review Letters, 2006. **97**(10): p. 103001.

15. Hybertsen, M.S., M. Schlüter, and N.E. Christensen, *Calculation of Coulomb-interaction parameters for La_2CuO_4 using a constrained-density-functional approach.* Physical Review B, 1989. **39**(13): p. 9028-9041.

16. Andriotis, A.N., R.M. Sheetz, and M. Menon, *LSDA+U method: A calculation of the U values at the Hartree-Fock level of approximation.* Physical Review B. **81**(24): p. 245103.

17. de P. R. Moreira, I.r., F. Illas, and R.L. Martin, *Effect of Fock exchange on the electronic structure and magnetic coupling in NiO.* Physical Review B, 2002. **65**(15): p. 155102.

18. Tran, F., et al., *Hybrid exchange-correlation energy functionals for strongly correlated electrons: Applications to transition-metal monoxides.* Physical Review B, 2006. **74**(15): p. 155108.

19. Perdew, J.P., M. Ernzerhof, and K. Burke, *Rationale for mixing exact exchange with density functional approximations.* The Journal of Chemical Physics, 1996. **105**(22): p. 9982-9985.

20. Heyd, J., G.E. Scuseria, and M. Ernzerhof, *Hybrid functionals based on a screened Coulomb potential.* The Journal of Chemical Physics, 2003. **118**(18): p. 8207-8215.

21. Rivero, P., et al., *Description of magnetic interactions in strongly correlated solids via range-separated hybrid functionals.* Physical Review B, 2009. **79**(24): p. 245129.

22. Chen, H. and J.H. Harding, *Nature of the hole states in Li-doped NiO.* Physical Review B, 2012. **85**(11): p. 115127.

23. Monkhorst, H.J. and J.D. Pack, *Special points for Brillouin-zone integrations.* Physical Review B, 1976. **13**(12): p. 5188-5192.

24. Payne, M.C., et al., *Iterative minimization techniques for ab initio total-energy calculations: molecular dynamics and conjugate gradients.* Reviews of Modern Physics, 1992. **64**(4): p. 1045-1097.

25. Blöchl, P.E., *Projector augmented-wave method.* Physical Review B, 1994. **50**(24): p. 17953-17979.

26. Hellman, H., *Einfuhrung in die Quantumchemie.* Franz Duetsche, Leipzig, 1937.

27. Feynman, R.P., *Forces in Molecules.* Physical Review, 1939. **56**(4): p. 340-343.

28. Pulay, P., *Ab initio calculation of force constants and equilibrium geometries in polyatomic molecules.* Molecular Physics, 1969. **17**(2): p. 197-204.

29. Kresse, G. and J. Furthmüller, *Efficient iterative schemes for ab initio total-energy calculations using a plane-wave basis set.* Phys. Rev. B, 1996. **54**: p. 11169.

30. Kresse, G. and D. Joubert, *From ultrasoft pseudopotentials to the projector augmented-wave method.* Phys. Rev. B, 1999. **59**: p. 1758.

Chapter 3

Ground state properties of $LiNiO_2$

3.1 Introduction

$LiNiO_2$ is a potential cathode material to replace $LiCoO_2$ in lithium ion batteries. Compared to cobalt, nickel is less toxic and inexpensive which make it a desirable material. In addition, $LiNiO_2$ exhibits good capacity with competitive voltages in the range of 3-4 V.

Although this compound has been intensively studied for decades, the local geometry, electronic and magnetic structure are still highly debatable. One factor that causes such confusion is the difficulty to synthesis truly stoichiometric $LiNiO_2$, even the most recent experimental studies struggle to do so. Where quoted, typical defect concentrations are of the order of a few percent – nickel is found on the lithium site of the perfect structure. The true formula is therefore $(Li_{1-x}Ni_x)NiO_2$

and the magnetic behavior and electrochemical performance are are sensitive to the value of x.

$LiNiO_2$ is usually synthesized by mixing NiO with Li_2CoO_3 or Li_2O[1, 2]. An X-ray spectroscopy study on $Li_xNi_{1-x}O$ reveals that the hole donated by Li^+ shows pronounced oxygen character[3]. Accordingly many subsequent XAS studies on the electronic structure of $LiNiO_2$ have been interpreted in terms of “oxygen hole”, thus claiming that the charge state of nickel remains Ni^{2+} in $LiNiO_2$ as the same in NiO. Similarly, the nature of the charge compensation accompanying Li deintercalation in $Li_{1-x}NiO_2$ is also controversial, again due to large amount of oxygen character of holes observed[4].

In this chapter, the effect of Li-doping on the crystal and electronic structure of NiO is first discussed in order to clarify the properties of doped holes. Then we go on to investigate possible local crystal structures of $LiNiO_2$ and its corresponding electronic structures.

3.2 Nature of hole states in Li-doped NiO

3.2.1 Review of literature

Hole doped Mott-insulators have attracted considerable attention due to the discovery of high-temperature superconducting cuprates. One basic question is the nature of the hole state in Mott insulating systems. NiO is traditionally considered to be a prototype Mott insulator with a wide band gap. It is often classified as a charge-transfer insulator, although the original Zaanen-Sawatzky-Allen paper[5] suggested that it is on the borderline between a charge-transfer and a Mott-Hubbard insulator. Indeed, recent work suggests a mixture of charge-transfer and Mott-Hubbard character[6], although most experimental and theoretical work has apparently supported the charge-transfer nature of the band gap in NiO[7-10]. Hole doping in NiO is usually obtained by doping NiO with lithium oxide (with which it forms an extensive solid solution) whereby Ni^{2+} is replaced by Li^{+}. Antolini has summarised the experimental evidence on the question of the nature of the hole[11]. The older magnetic measurement studies adopted Ni^{3+} as the relevant nickel charge state for interpreting their results[12], as do all the current studies on the related compound $LiNiO_2$[13]. Changes in the Ni-Ni bond length with the composition, *x,* of $Li_xNi_{1-x}O$ obtained from nickel K-edge X-ray absorption fine structure spectroscopy[14] support the idea that the nickel ion should be considered as Ni^{3+} - i.e. the hole is on the metal. On the other hand, oxygen K-edge X-ray absorption spectroscopy of $Li_xNi_{1-x}O$ has been interpreted in terms of holes on the oxygen atoms[3]. This interpretation relies on ideas taken from an analysis of excitations in pure NiO[7]. This work, together with a number of *ab initio* calculations[15, 16] discussed below, is the justification of the idea that the hole is in the oxygen valence band, localised on an oxide ion next to the Li dopant (hence formally producing an O^- ion).

Previous theoretical work using spin-unrestricted Hartree-Fock and hybrid functionals with a high-percentage of Fock exchange predicted that the hole states resided mainly on oxygen[15, 16]. However the high percentages of Fock exchange used lead to an unreasonably large band gap in NiO[17, 18]; in effect these methods over-emphasise an ionic description. Consequently the valence band edge was found to consist exclusively of oxygen states in these calculations. This is not consistent with the large contribution from Ni states seen in the valence band edge in experiment[7]. Recent work using Dynamic-Mean-Field theory (DMFT) calculations also predicted oxygen holes[19]. However, that calculation ignores the Li ion completely except for its ability to generate holes. This discounts both the structure relaxation and the Li impurity potential. Moreover, these calculations failed to reproduce the “surviving” gap upon Li doping observed in oxygen K-edge X-ray-absorption spectra which the previous authors[14] ascribed to a localising potential. We have therefore performed calculations that explicitly include the Li ion, performed within periodic boundary conditions rather than using a finite cluster.

3.2.2 Computational details

Hybrid functional and DFT+U methods are used to investigate Li-doped NiO. The HSE06 hybrid functional, which mixes 25% of Hartree-Fock exchange with 75% of the PBE functional, is used[20]. The inclusion of Hartree-Fock exchange corrects the self-interaction error contained in standard DFT functionals and so greatly improves the description of strongly correlated systems such as transition metal oxides. It has been shown previously that 20% to 35% of exact exchange in DFT calculations results in good physical properties for NiO[17]. In DFT+U, the rotational invariant formalism[21] is used and $U_{eff} = U – J$, the onsite correction, is set to be 5.3 eV for Ni 3d electrons. The number is taken from a previous study on NiO in which this U_{eff} value was shown to give reasonable physical properties[22]. In this study we assume that the hole is localised on the Ni ion (through the application of the U_{eff} correction for Ni only). The application of the onsite correction on oxygen 2p orbitals has also been used for oxide materials. Nevertheless, the effect of onsite correction on both 3d and 2p orbitals is included in the HSE06 calculations for which we also present results. It will be shown that the correction on 3d alone is sufficient to reproduce qualitatively same results as the HSE06 method.

To model Li-doped NiO, we consider a single composition whereby one Ni is replaced by Li in a 2x2x2 antiferromagnetic NiO supercell with 8 formula units. This corresponds to a non-stoichiometry of x=0.125 in $Li_xNi_{1-x}O$ which is well within the experimental range and, moreover, was the composition chosen for the Hartree-Fock calculations discussed above.

The full structure optimisation is performed without any cell or symmetry constraint, until the force is less than 0.01 eV-Å^{-1} per ion. A plane wave energy cut-off of 500eV and k-point meshes of 5x5x5 for HSE06 and 6x6x6 for GGA+U were used. All calculation were carried out using the Vienna *ab initio* simulation package (VASP)[23].

3.2.3 Localisation of hole states

NiO adopts a cubic rocksalt structure with space group Fm3m. The Ni^{2+} ions in NiO have a high spin d^8 ($t_{2g}^6 e_g^2$) electronic configuration. The calculated lattice parameters, Ni magnetic moments and band gaps of NiO are listed in Table 3-1. Both the HSE06 functional and the GGA+U calculations yield good agreement with experimental values apart from the underestimate of the band gap by about 1 eV in GGA+U.

Table 3-1: Comparison of calculated and experimentally measured properties of NiO

	Lattice parameter (Å)	**Ni magnetic moment (μ_B)**	**Band gap (eV)**
HSE06	4.179	1.66	4.1
GGA+U	4.20	1.69	3.2
Experiment	4.171[a]	1.64[b], 1.77[c], 1.90[d]	4[e]

[a]Reference [24] [b]Reference[25] [c]Reference[26]

[d]Reference[27] [e]Reference[28]

Upon Li doping, the local environment of one of the Ni ions undergoes substantial distortion with four short and two long Ni-O bonds, whereas the environments of the other six Ni stay unaltered as shown in Table 3-2. The magnetic moment of the nickel ion in the distorted environment is also substantially reduced. The Ni-O bond lengths of this distorted Ni are very similar to those reported for Ni^{3+} in $LiNiO_2$ (which has a Jahn-Teller distortion). Comparing this to the local density of states (DOS) of the undistorted Ni^{2+} ($t_{2g}^6 e_g^2$) in figure 3-1, the extra unoccupied spin-up e_g state in the distorted Ni DOS shows that its electronic configuration should be $t_{2g}^6 e_g^1$ and hence Ni^{3+}.

Table 3-2: Ni-O bond lengths and Ni magnetic moments in the optimised $LiNi_7O_8$ structure.

	HSE06			**GGA+U**		
	d_{Ni-O} (Å)	**Bader charge (e)**	**Magnetic moment (μ_B)**	**d_{Ni-O} (Å)**	**Bader charge (e)**	**Magnetic moment (μ_B)**
Ni (undistorted)	2.07-2.09	+1.43	1.65	2.08-2.10	+1.31	1.69
Ni (distorted)	1.90 x 4, 2.13 x 2	+1.61	0.88	1.93 x 4, 2.14 x 2	+1.43	1.05

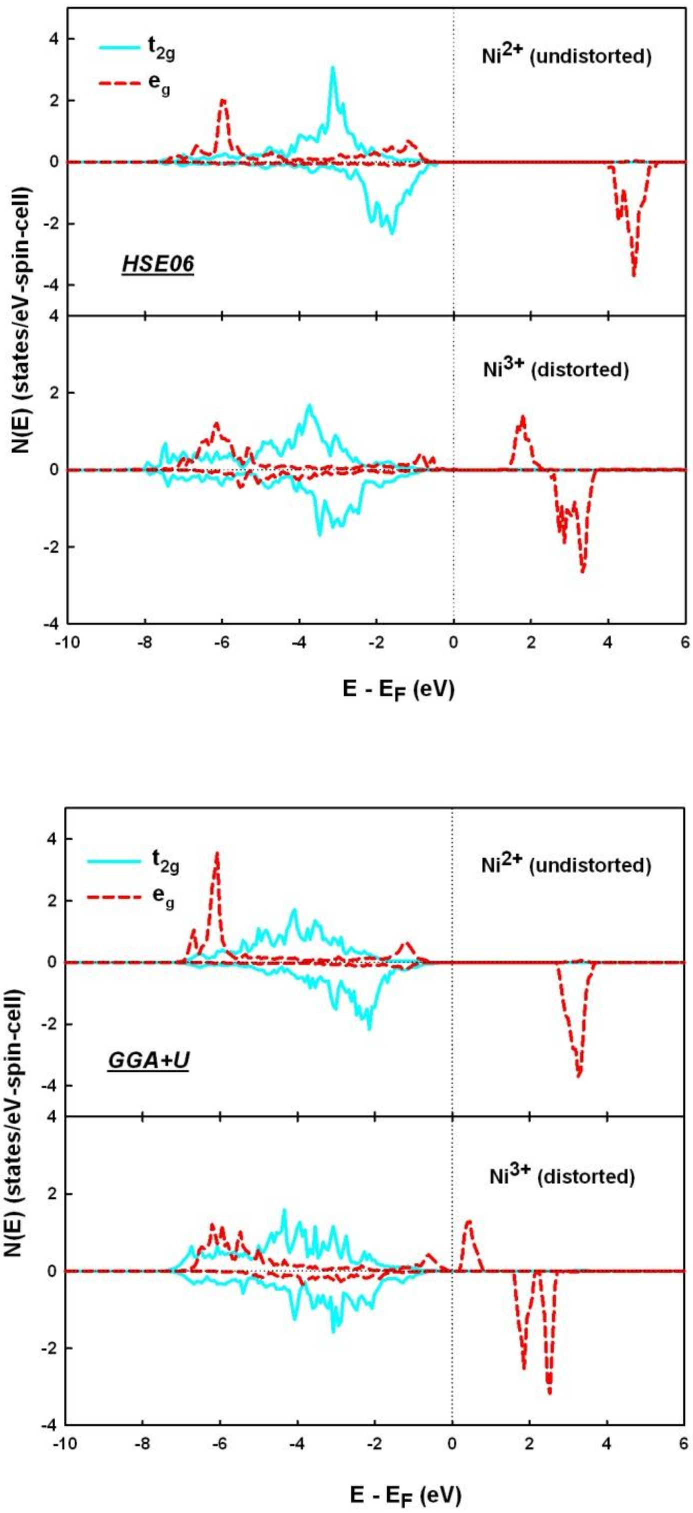

Figure 3-1: Local density of states of the undistorted and distorted Ni in the $LiNi_7O_8$ supercell using the HSE06 functional (upper) and GGA+U (lower).

Figure 3-2 shows the total density of states of pure NiO and Li doped NiO ($LiNi_7O_8$), from both HSE06 and GGA+U calculations. In NiO, the valence band edge states consist of about 50% Ni and 50% oxygen character, consistent with the large Ni d spectral weight at the top of the valence band obtained from both local-density approximation (LDA) + DMFT calculations[19] and also from experiment[7]. Upon hole doping by substituting one Ni with Li, hole states in $Li_{0.125}Ni_{0.875}O$ emerge with three peaks within the NiO band gap. They are clearly associated with the distorted Ni^{3+}, as can be seen from the local density of states (LDOS) in figure 3-1.

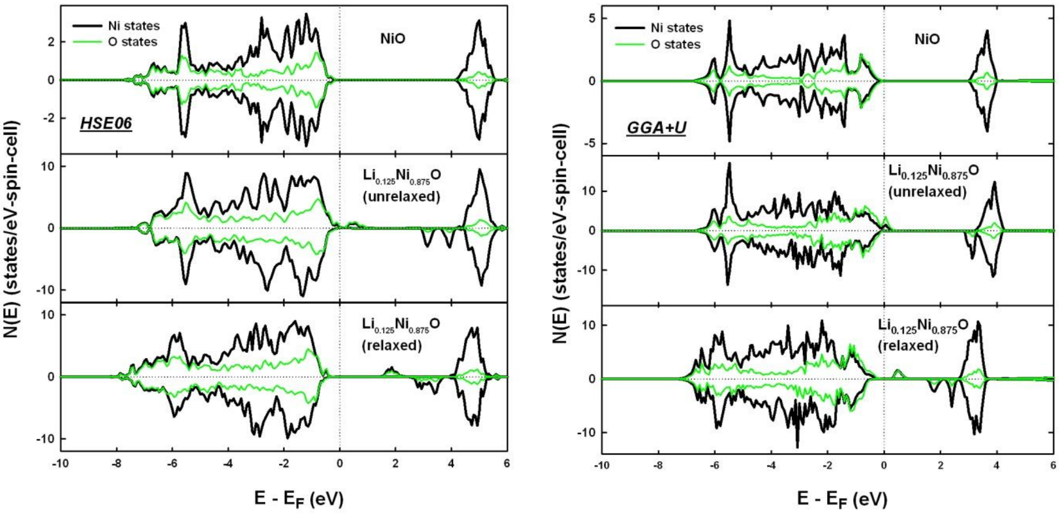

Figure 3-2: Density of states of NiO and $Li_{0.125}Ni_{0.875}O$ for the HSE06 functional (upper) and GGA+U (lower) showing both relaxed and unrelaxed cases for $Li_{0.125}Ni_{0.875}O$. Note in the GGA+U density of states for $Li_{0.125}Ni_{0.875}O$, the Ni and O states overlap completely at the spin-up peak around 0.5 eV.

However, the band gaps are only opened if structural relaxation is allowed (see figure 3-2). This indicates that Jahn-Teller distortion is the key for the emergence of the band gap and a concomitant hole localisation on Ni. Although the band gaps narrow to about 1.3eV (HSE06) and 0.5eV (GGA+U) in $Li_{0.125}Ni_{0.875}O$, they are both consistent with the absence of metallic conductivity in the $Li_xNi_{1-x}O$ system.

In order to have a direct comparison with existing experimental results, we have attempted to reproduce the oxygen K-edge absorption spectra from our ground state structures of NiO and $Li_{0.125}Ni_{0.875}O$, by plotting out the calculated empty oxygen states with a Gaussian smearing width 1 eV. Although the core-hole effect is not accounted for in our calculations, it has been shown that the main characteristics of the oxygen K-edge absorption spectra can still be correctly reproduced without the core-hole in NiO at the DFT+U level[29]. Figure 3-3 shows the calculated spectra for pure NiO and $Li_{0.125}Ni_{0.875}O$, along with the experimental spectra[3]. The four peaks A to D in the NiO oxygen absorption spectrum agree well with available experimental spectra.

Upon Li doping a new peak E appears in the calculated spectra which corresponds to the peak at 528.5 eV in the experimental spectra. When compared to the density of states in figure 3-2, this new peak E is seen to be the contribution from the states that describe the hybridisation between O^{2-} and Ni^{3+}. As x increases, the concentration of Ni^{3+} increases and consequently the intensity of this peak increases. In addition to the peak appearing at about 528.5 eV, there is another peak at about 530 eV which was ignored by the original authors but can be clearly seen in the x=0.4 curve as circled. This peak is also seen in an oxygen K-edge electron-energy-loss-spectroscopy[30] and was ignored there also. As we can see from figure 3-2, in addition to the oxygen states associated with peak E, there is also a small oxygen contribution associated with the empty spin-down e_g states of the Ni^{3+} ion. We suggest that these states are the source of the double peak feature at high lithium concentration.

To further elucidate where the hole states go in Li doped NiO, we have plotted out the charge density constructed from the wave functions of the hole states in the band gap, as shown in figure 3-4. Because the HSE06 and GGA+U calculations produce indistinguishable graphs only the HSE06 case is presented for simplicity. It is clear that hole states mainly reside on one nickel ion with a small amount on the six oxygen ions surrounding the nickel. Again the contribution from oxygen is the consequence of the strong hybridisation between the nickel ion and its six surrounding oxygen ions.

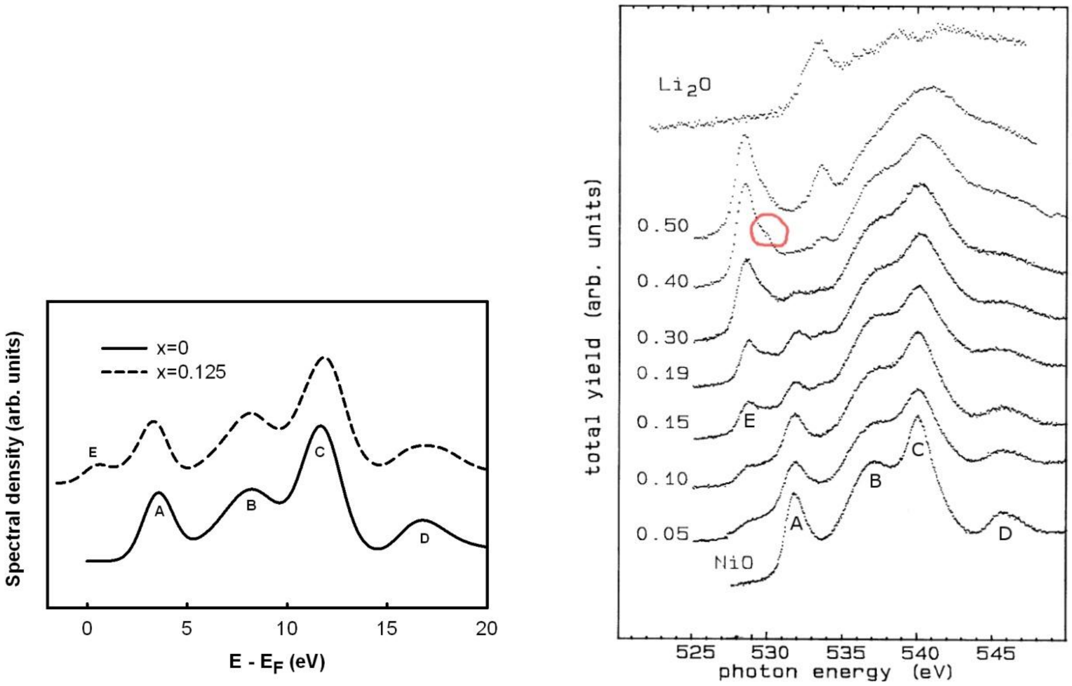

Figure 3-3: Calculated oxygen empty states (left) of $Li_xNi_{1-x}O$ with x=0, 0.125 (offset for clarity) using GGA+U compared to experimental result (right) from ref[3]. Note the peak (circled) in the experimental data for *x* = 0.4

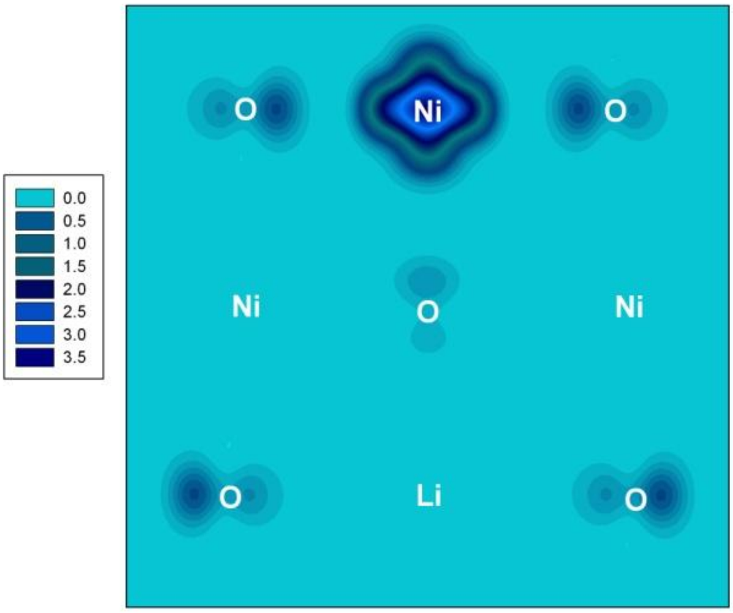

Figure 3-4: Charge density contour map (e/Å^3) of hole states in the (100) plane for $Li_{0.125}Ni_{0.875}O$. Results shown for the HSE06 functional; those for the GGA+U method are indistinguishable.

3.3 Charge disproportionation and Jahn-Teller distortion in $LiNiO_2$

3.3.1 Review of literature in theory and experiment

Chemical intuition suggests that the nickel ion in $LiNiO_2$ should be regarded as low-spin Ni^{3+} ($t_{2g}^6e_g^1$) since lithium and oxygen are Li^+ and O^{2-} respectively. Due to the orbital degeneracy of the electronic configuration of Ni^{3+}, according to Jahn-Teller theorem[31], the $(Ni^{3+})(O^{2-})_6$ octahedron should undergo a distortion that lifts such degeneracy and lowers the energy. Indeed two different Ni-O bond lengths have been observed both in Extended X-ray Absorption Fine Structure(EXAFS) spectroscopy[32] and neutron diffraction[33] studies which are attributed to a *local* Jahn-Teller distortion. However unlike other Jahn-Teller active systems such as $NaNiO_2$ and $LiMnO_2$, no cooperative distortion has been observed in $LiNiO_2$.

A trimer ordering of Jahn-Teller distortions of Ni^{3+} ions was proposed from the neutron study[33] and the absence of long-range ordering was explained by domain formation induced by the strain generated by such trimer ordering. The analysis of the neutron partial density function (PDF) in the study supports the hypothesis of a Jahn-Teller distortion since their results show four bond-lengths grouped as “long bonds” (2.04 Å and 2.06 Å with an average length of 2.05 Å) and “short bonds” (1.90 Å and 1.96 Å with an average length of 1.93 Å) suggestive of the 2:1 ratio of short to long bonds expected for Jahn-Teller distortion. However, the long-range PDF peaks increase in height with temperature – an unusual effect that the authors again attribute to domain formation.

The electronic structure of $LiNiO_2$ has been directly probed by X-ray Absorption Spectroscopy (XAS). Following the interpretation of oxygen hole in Li-doped NiO, XAS studies on $LiNiO_2$ suggested the charge state $Li^+Ni^{2+}(O_2)^{1.5-}$[4, 34]. Another XAS study revealed different surface electronic structure from the bulk in $LiNiO_2$[35]. It was found that the nickel ions at the surface show largely Ni^{2+} character and Ni^{3+} in the bulk.

The electrically insulating behavior with a band gap of ~0.5 eV[36] was first reproduced from a DFT+U calculation by allowing a collinear Jahn-Teller distortion which causes the split of Ni^{3+} e_g band[37]. However as mentioned above such a collective distortion has never been observed in $LiNiO_2$. In another theoretical study using density functional calculation with the self-interaction-correction method, Ni is also determined to be Ni^{3+} in $LiNiO_2$[38]. Although the insulating behaviour is reproduced with a band gap, the six Ni-O bonds of the NiO_6 octahedron are assumed to be identical in the study which is not consistent with the two different Ni-O bond lengths experimentally observed.

The magnetic properties of $LiNiO_2$ have been a matter of debate since the first measurements in 1958[12]. Reynard *et al.*[13] suggested, on the basis of anomalies in the spin susceptibility observed at 10 K and 400 K, that there are at least two energy scales involved, corresponding to spin and orbital interactions, and that the possibility of orbital frustration should be considered. The neutron studies[33] argue against this since this would imply that the number of “short” and “long” Ni—

O bonds would be equal. The authors suggest instead that the magnetic properties should be explained by the assumption that there is local orbital ordering: the $3d_{z^2-r^2/3}$ orbitals of three Ni^{3+} ions point towards their shared oxygen. This model also receives support from a recent electron diffraction study. However, there remain problems with the interpretation of the magnetic data using this scheme; in particular the coexistence of ferromagnetic and antiferromagnetic spin fluctuations. It is argued that the existence of domains, required to prevent stress buildup caused by the trimer ordering, may restrict the antiferromagnetic fluctuations.

Finally, a whole range of possible electronic ground states are noted in compounds that have a nominal Ni^{3+} charge state, from a totally delocalized metal ($LaNiO_3$) to a strongly localized orbital ordering insulator ($NaNiO_2$). This is shown in Table 3-3 where the behaviour is correlated with the nickel-oxygen bond length (d_{Ni-O}). Charge disproportionation, an alternative to lifting the orbital degeneracy, is also reported for other rare earth nickelates[39]. It can be seen from the Table 1 that in the case of $LiNiO_2$ there could be a competition between charge ordering and orbital ordering for the ground state. We demonstrate that this is indeed the case using first principles density functional theory and to discuss the consequences.

Table 3-3: The Ni-O bond lengths (d_{Ni-O}) in compounds with the nominal valence state Ni^{3+} and their ground state behaviour. Numbers of Ni-O bonds of a given length given in brackets. *Note that the Ni-O bond lengths differ between studies of $LiNiO_2$.

Compound	**d_{Ni-O} (Å)**	**<d_{Ni-O} >(Å)**	*Electronic ground state*
$LaNiO_3$[40]	1.933 x 6	1.93	Metallic (delocalised)
$NdNiO_3$[41]	$Ni^{3+\delta}$ 1.891 x 2 1.911 x 2 1.930 x 2	1.947	Charge ordering insulator
	$Ni^{3-\delta}$ 1.960 x 2 1.966 x 2 2.023 x 2		
$LuNiO_3$[42]	$Ni^{3+\delta}$ 1.892 x 2 1.915 x 2 1.937 x 2	1.957	Charge ordering insulator
	$Ni^{3-\delta}$ 1.975 x 2 2.019 x 2 2.003 x 2		
$YNiO_3$[43]	$Ni^{3+\delta}$ 1.901 x 2 1.924 x 2 1.944 x 2	1.958	Charge ordering insulator
	$Ni^{3-\delta}$ 1.963 x 2 2.006 x 2 2.012 x 2		
$AgNiO_2$[44]	$Ni^{3.5+}$ 1.934 x 6	1.963	Moderately charge ordering, $3Ni^{3+} \rightarrow Ni^{2+}+2Ni^{3.5+}$
	Ni^{2+} 2.022 x 6		
$LiNiO_2$[33]	1.91 x 4 2.04 x 2	1.97	
$NaNiO_2$[45]	1.92 x 4 2.15 x 2	2.00	Orbital ordering insulator

3.3.2 Computational details

In this study, the rotational invariant form[21] of the DFT+U formalism was used and $U_{eff} = U - J$, the onsite correction, was set to be 6.5 eV for Ni 3d electrons adapted from a self-consistent calculation[46]. Other work[47] has used a smaller value of U_{eff}. It is, however, important to demonstrate that the results of calculations are not strongly dependent on the value of the U parameter chosen and we provide evidence for this below. The inclusion of the U parameter has been shown to successfully reproduce the charge disproportionation in $AgNiO_2$, $LuNiO_3$, $NdNiO_3$, $YNiO_3$ and used to investigate possible charge-orbital orderings in Fe_3O_4[48-50]. The cut off energy for plane-waves was set at 500 eV. For all cells, the k-point spacing is less than 0.03 $Å^{-1}$ in the Brillouin zone. Convergence of the energy was confirmed for both these parameters. For geometry optimisation, the force was converged to less than 0.01 eV-$Å^{-1}$ per ion. In all cases, the cells were fully optimised assuming the starting symmetry of the cell. All calculations were carried out using the Vienna *ab initio* simulation package (VASP)[23].

$LiNiO_2$ is frequently reported to crystallise in the hexagonal structure with $R\bar{3}m$ space group symmetry. A slight monoclinic distortion was observed at low temperatures (10 K) by the neutron diffraction study of [33] and a better fit found to the *C2/m* space group, but detailed analysis showed that the collinear ordering of the Jahn-Teller distortions implied by this space group was not supported by a combination of the Rietveld refinement and the neutron PDF data. An electron diffraction study[51] was analysed using the *Pm* space group which is the simplest space group that can incorporate a trimer ordering model.

Previous density functional calculations have predicted that distortions with *C2/m* symmetry lower the cohesive energy but did not consider charge disproportionation. In order to investigate the various possible electronic relaxations in $LiNiO_2$ we have used four unit cells as starting configurations. Two of these, $R\overline{3}m$ and *C2/m* cells (each with one formula unit) have been discussed before. In addition, two more cells are proposed and discussed below. One cell contains a zig-zag Jahn-Teller orbital ordering of the Ni^{3+} ions and has $P2_1/c$ symmetry with two formula units. The other cell, with *P2/c* symmetry containing four formula units, but retaining good agreement with the measured lattice parameters of the low temperature structure, was constructed for the charge disproportionation model. As far as we are aware, no attempt has been made to analyse the experimental data using the *P2/c* space group. We have also investigated the *Pm* unit cell (trimer ordering) but, as we shall show, when the cell geometry is optimised, it becomes indistinguishable from $P2_1/c$. The different orderings of Jahn-Teller distortion are illustrated in figure 3-5.

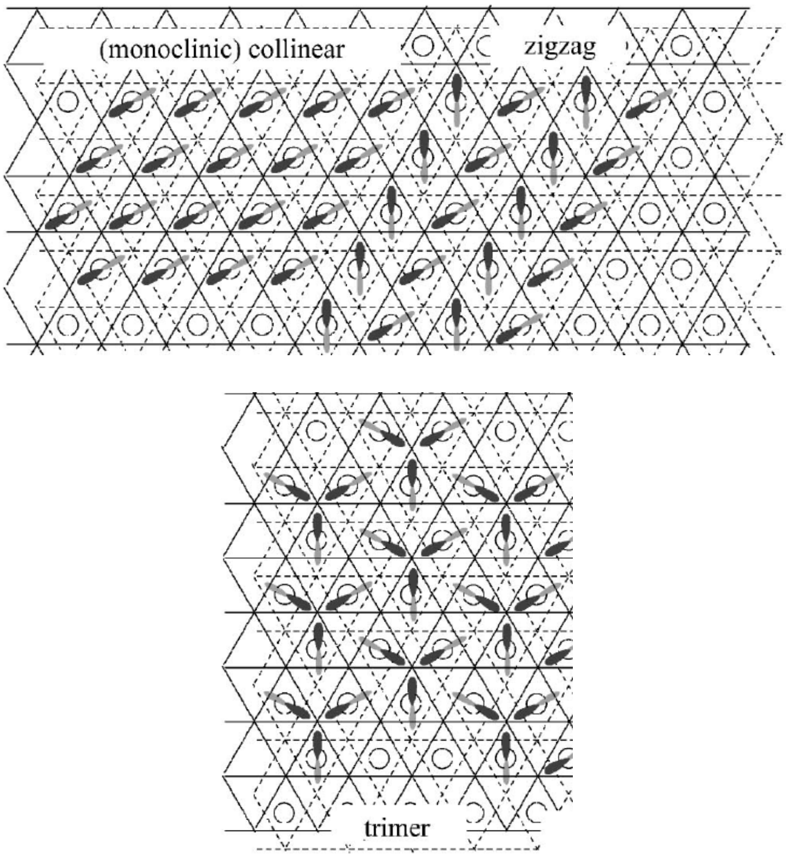

Figure 3-5: Three different possible ordering of Jahn-Teller distortions of Ni^{3+}. Open circles denotes Ni^{3+} ions and solid and dashed lines denote oxygen planes above and below the Ni^{3+} layer. Images are taken from [33].

3.3.3 Results and discussion

We have calculated the structures and lattice energies of the four unit cells discussed above and present our results both for the structure and relative energies of the cells (using the $R\overline{3}m$ cell as a baseline for convenience). The relative ordering of lattice energies for the four cases is independent of the choice of the U$_{\text{eff}}$ value provided that value falls in the range 5.5-7.0 eV as shown in Figure 3-6. Outside this range, the *P2/c* is destabilised relative to the *C2/m* and *P2₁/c* cells. Previous work[47] using a smaller value of U_{eff} (4.5 eV) is still comparable since, as can be seen from Figure 3-6, the relative energies of the *C2/m* and $P2_1/c$ cells change little over a very wide range of U_{eff} values. Even for a value of U_{eff} as low as 4.5 eV, the *P2/c* cell is comparable in energy with the *C2/m* and $P2_1/c$ cells. We note comparison with previous work where relevant (and consider only the fully relaxed cases) but our aim is rather different to theirs since we wish to consider whether the charge disproportionation cell can be lower in energy than any Jahn-Teller ordering. Structural data for the cells is given in Table 1 for the chosen U_{eff} value of 6.5 eV. All further results use this value. It is convenient to consider the results for the unit cells in turn.

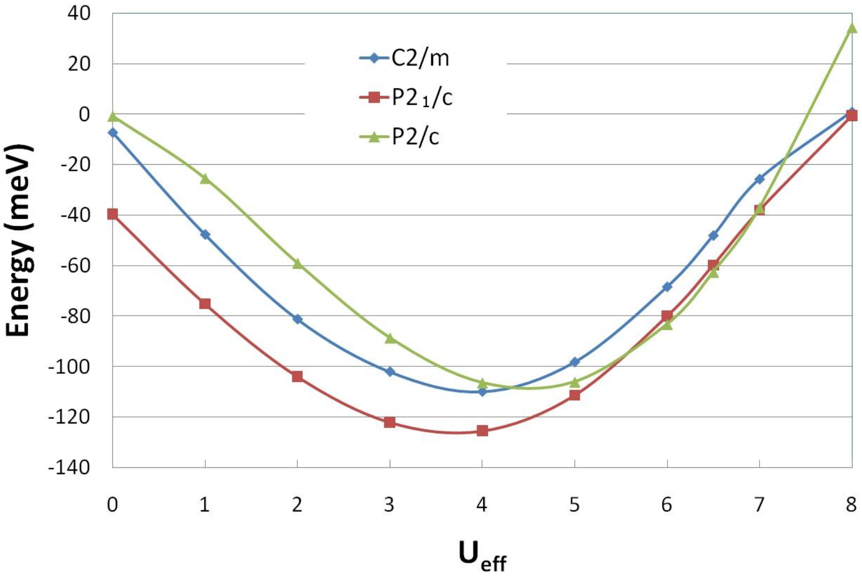

Figure 3-6: Stabilisation energies (relative to the $R\overline{3}m$ cell and given per formula unit) of the *C2/m*, $P2_1/c$ *and P2/c* cells as a function of U_{eff}.

The cell parameters of the $R\bar{3}m$ cell are shown in Table 3-4 and demonstrate good agreement with the experimental values. Figure 3-7 shows the density of states of the $R\bar{3}m$ cell. The empty spin-up e_g band(*) and half empty spin-down e_g band indicates an electronic configuration $t_{2g}^6 e_g^1$ which corresponds to the low-spin d^7 state and hence Ni^{3+}. $LiNiO_2$ is reported to be a semiconductor with a band gap of about 0.5 eV [36] but in the cell the spin-down e_g band lies on the Fermi level which implies conducting behaviour. The symmetry of the $R\bar{3}m$ cell ensures that all six Ni-O bonds are identical and disagrees with the observation of different Ni-O bond lengths seen in experiment.

Table 3-4: The optimised geometries of cells and calculated magnetic moments on nickel ions. Experimental values reported in brackets ($R\bar{3}m$; *C2/m*, the Ni-O bond lengths quoted here are taken from the analysis of the Rietveldt refinement, not the neutron PDF analysis as discussed in the text below since this is not tied to the *C2/m* symmetry).

Space Group	a (Å)	b (Å)	c (Å)	β (degrees)	d_{Ni-O} (Å)	Magnetic moment (μ_B)
$R\bar{3}m$	2.9023 (2.8788)		14.1889 (14.2035)		1.99[6] (1.974)	1.419
C2/m	5.151 (4.9693)	2.7929 (2.8774)	5.1461 (4.9967)	112.011 (109.204)	1.90[4], 2.14[2] (1.94[4], 1.96[2])	1.108
$P2_1/c$	5.8468	2.9302	4.90974	125.641	1.91[4], 2.12[2]	1.140
P2/c	5.0291	5.8059	4.942	70.6822	Ni(a) 2.05-2.07 Ni(b) 1.88-1.91	Ni (a) 1.759 Ni (b) 0.128

---

* From standard crystal field splitting models, the local e_g orbitals on Ni are higher in energy than the t_{2g} orbitals. For this discussion we identify the unoccupied states of nickel shown in the density of states figures as the equivalent of the e_g states discussed in the text.

In the optimised *C2/m* cell, there are four short Ni-O bonds at 1.90 Å and two long Ni-O bonds at 2.14 Å which corresponds to a Jahn-Teller distorted system. The total density of states of the *C2/m* cell shown in Figure 3-7 shows a split in the e_g band relating to a Jahn-Teller distortion. The band gap is approximately 0.5 eV, again in good agreement with the experimental data. Two unoccupied spin-up e_g states and one unoccupied spin-down e_g state are present which indicates an electronic configuration $t_{2g}^6e_g^1$, and hence Ni^{3+}. This cell appears to be an accurate description for the Jahn-Teller relaxed structure generally accepted as the ground state of $LiNiO_2$. However, this cell presupposes a long-range cooperative Jahn Teller distortion which is not observed.

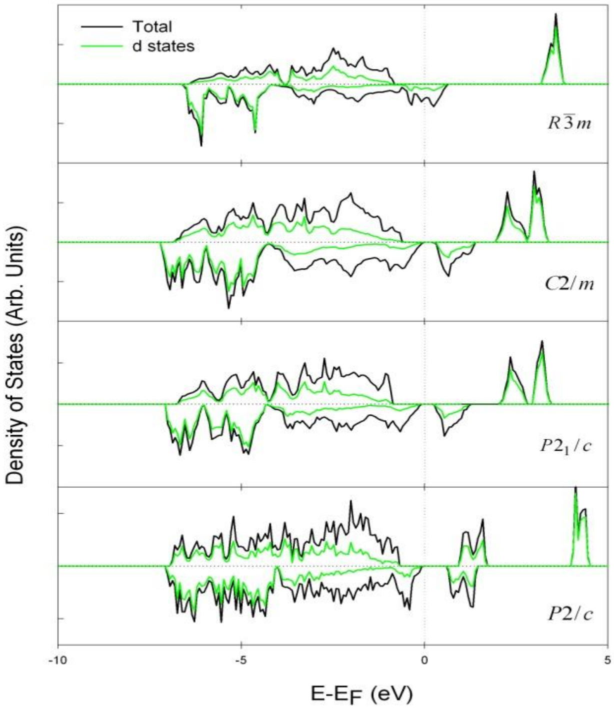

Figure 3-7: The density of states of the four candidate unit cells for $LiNiO_2$. Cells are indicated as above. Note that only the Jahn-Teller distorted (C2/m, $P2_1$/c) or charge disproportionation (P2/c) cells show semi-conducting behaviour.

In the *$P2_1/c$* cell, all Ni ions are Jahn-Teller distorted with 4 short Ni-O and 2 long Ni-O bonds, implying the presence of Ni^{3+} ions. The geometrical difference from the C2/m cell is that the orientations of Jahn-Teller distortions in this cell are in a zigzag ordering. This induces, as expected, significant distortion of the lattice from the *C2/m* cell which is not observed in experiment. The results are similar to previous work; the most notable change being that the monoclinic angle found here (125˚) is significantly larger than previously (107.87˚). From Figure 3-7, the electronic structure of this *$P2_1/c$* cell is almost identical to the C2/m cell since the Ni ions are all Ni^{3+} in both cells. Nevertheless, it will be shown that this zigzag Jahn-Teller ordering is more stable than the collinear case. Calculations were also performed using the *Pm* cell (which represents the trimer ordering case) as a starting point. Results without relaxation produced a cell of significantly higher energy (per formula unit) than the $R\bar{3}m$ cell. The higher energy of this structure may be due to the geometrical frustration identified in [33] resulting in significant strain in the structure. We are not able to relieve this strain by introducing the large-scale curvature suggested in [33] – the number of atoms required for such a calculation are beyond what *ab initio* calculations can currently consider. Upon geometrical relaxation, the *Pm* cell relaxed to a cell of *$P2_1/c$* symmetry with the behaviour discussed above.

The P2/c cell contains four $LiNiO_2$ formula units and two inequivalent Nickel sites in a zigzag ordering. The total density of states in Figure 3-7 indicates that the *P2/c* cell is a semi-conductor with a band gap about 0.5 eV, in good agreement with the measured value. In the optimised geometry, Ni(a) has six long Ni-O bonds at 2.04 ~ 2.07 Å with a magnetic moment of 1.759 μ_B. The local density of states in Figure 3-8 shows that one e_g band is unoccupied (the spin-down band but the choice is arbitrary), indicating the (high-spin) electronic configuration $t_{2g}{}^6e_g{}^2$ or Ni^{2+}. Ni(b) has six short Ni-O bond lengths at 1.88 ~ 1.91 Å with a magnetic moments 0.128 μ_B. The local density of states in Figure 3-8 for Ni(b) shows that both the spin-up and spin-down e_g bands are unoccupied, indicating the electronic configuration $t_{2g}{}^6e_g{}^0$ or low-spin Ni^{4+} .

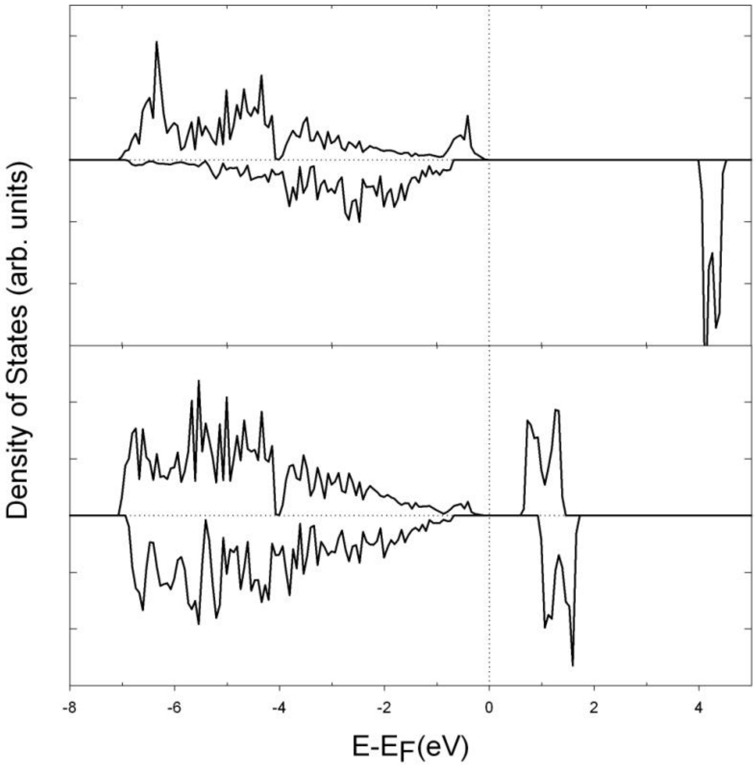

Figure 3-8: Local density of states for the two inequivalent nickels in the *P2/c* cell. The top diagram shows the nickel with six long Ni-O bonds. The bottom diagram shows the nickel with six short Ni-O bonds.

Figure 3-9 shows the iso-surface of the charge density difference which demonstrates substantially different amounts of electron density on the two Nickel ions. The *P2/c* cell therefore shows charge disproportionation. Although not reported in experiments, the *P2/c* cell reproduces the insulating character of $LiNiO_2$ and the amount of monoclinic distortion displayed is about 0.22°, in very good agreement with the value 0.16° detected by neutron diffraction at low temperature[33] in the sample assigned to *C2/m* symmetry.

We emphasise that, despite the simple denotation of the nickel charge states as Ni^{2+}, Ni^{3+} and Ni^{4+}, there is considerable charge transfer between the nickel and oxygen ions due to the covalency arising from the overlap between metal 3d and oxygen 2p orbitals. This is clear from the densities of states in Figure 3-7 from looking at the amount of d character shown in the figures. A similar point is made by the Mulliken and Bader charges shown in Table 3-5 below.

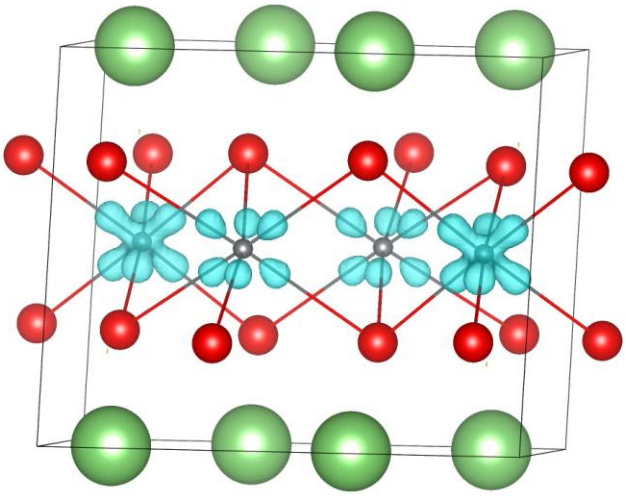

Figure 3-9: Charge density difference (total density minus sum of atomic densities) for the *P2/c* cell. Green denotes Li, red denotes O and grey denotes Ni. The iso-surface shown in blue corresponds to charge density 0.5 e/Å^3. Note the difference between two kinds of Ni atom.

TABLE 3-5: Bader charges of nickel and oxide ions in the cells calculated cells. The values in brackets are the volumes (Å^3) within which the charge is calculated.

Space Group	Bader Charge (Ni)	Bader Charge (O)
$R\bar{3}m$	+1.3671 (7.5376)	-1.183
C2/m	+1.4459 (7.1567)	-1.223
$P2_1/c$	+1.4259 (7.182)	-1.213
P2/c	Ni(a) +1.279 (8.279) Ni(b) +1.485 (6.425)	O(a) -1.123 O(b) -1.259

The lattice energies of the four cells are listed in Table 3-6. The lowest energy cell for $LiNiO_2$ is that with *P2/c* symmetry. This suggests that charge disproportionation must be considered as a reasonable mechanism to remove the orbital degeneracy of Ni^{3+} in $LiNiO_2$. The ordering of the other cells is the same as for previous work but the relative stabilisation energies are somewhat different – the ones quoted here are about twice those in [47]. This can reasonably be ascribed to the different U_{eff} values used. The lattice energy of the *P2/c* cell is, however, only about 2 meV lower than the $P2_1/c$ cell (the equivalent of 25 K and well within the margin of error of the calculation) and 14.5 meV lower than the *C2/m* cell (the equivalent of 170 K and probably within the margin of error). Table 3-6 also shows the lattice energies for $NaNiO_2$ in the three different symmetries explored for $LiNiO_2$. $NaNiO_2$, unlike $LiNiO_2$, is found exclusively in the Jahn-Teller relaxed state. Previous calculations on the $\mathrm{R\bar{3}m}$ and C2/m cells of $NaNiO_2$ were performed using a U_{eff} value of 4.5 eV but from Figure 3-6 it is clear that similar results are expected for our value of 6.5 eV except for the P2/c disproportionation cell which the previous work did not consider. Our calculations find the lowest energy configuration in $NaNiO_2$ to be the cooperative *C2/m* Jahn-Teller cell by approximately 32 meV (and 58 meV below the charge-disproportionation cell P2/c). This is many times the energy difference between the lowest-energy Jahn-Teller cell and the charge disproportionation cell in $LiNiO_2$.

Table 3-6: Calculated lattice energies per formula unit (meV) relative to the $\mathrm{R\bar{3}m}$ cell using a U_{eff} parameter of 6.5 eV. The lowest energy cells are shown in bold. The Pm cell is shown in italics since it is unrelaxed.

	$LiNiO_2$	$NaNiO_2$
Pm	*+61.80*	n/a
$R\bar{3}m$	0	0
C2/m	-48.05	**-78.65**
$P2_1/c$	-60.37	-46.28
P2/c	**-62.56**	-20.53

Our results suggest that both Jahn-Teller distortion and charge disproportionation are possible in samples of $LiNiO_2$ at the temperatures at which all the experiments to determine the structure were performed. The EXAFS experiments were performed at room temperature; no temperature is reported for the electron diffraction work but it is reasonable to infer that it was performed at room temperature; the neutron diffraction was performed at a range of temperatures between 10 K and 585 K. This may explain the differences in reported experimental structures. Slight changes in the *growth* conditions, stoichiometry, and other variables could favour the formation of one cell rather than another. It is also possible that both relaxations can occur within the same sample within different grains for example or at the surface versus the bulk or there exists a more stable phase with a complicated charge-orbital ordering pattern, in which Ni^{2+}, Ni^{3+} and Ni^{4+} coexist.

The *P2/c* cell matches the majority of the reported experimental findings, two different Ni-O bond lengths, the small monoclinic distortion, the band gap and the lack of Jahn-Teller related magnetic properties. Its most important failure is that such a cell should give an approximately 1:1 ratio of the Ni-O short to long bonds rather than the approximate ratio of 2:1 observed in [33] (assuming that we group the Ni—O bond lengths as suggested there). However, if the PDF in [33] is sampling a mixture of the cells involving charge disproportionation and Jahn-Teller distortion, then our results are consistent with this work since it is clear from the PDF that there is a range of Ni-O distances which contribute to the approximate 2:1 ratio depending on how they are grouped together. We would also have a natural explanation for the domain structure claimed by [33] at low temperatures.

We turn finally to the magnetic data. Both the data of ref[13] and the more recent µSR data[52] suggest that the ferromagnetic and antiferromagnetic states are close in energy. The ESR data suggests that the dominant interactions are ferromagnetic, but that strong antiferromagnetic fluctuations exist between 13 K and 50 K. However, the saturation of the linewidth suggests that the antiferromagnetic correlations do not propagate below 10 K. The detailed interpretation of the behaviour in terms of orbital frustration is not consistent with later neutron[33] and electron diffraction[51] work. The μSR data predicts different magnetic ground states for different compositions of $Li_{1-x}Ni_xO_2$; ferromagnetic for x = 0.03 and x = 0.15; antiferromagnetic for x = 0.02. The authors state that this supports the idea that the change in magnetic state is a bulk effect rather than demonstrating the formation of ferromagnetic or antiferromagnetic domains.

Our calculations cannot fully resolve this issue because of the limited accuracy of density functional theory calculations, but they can illustrate why the complexity exists. We have performed spin-polarised calculations on all the unit cells considered above. The *C2/m* cell has a ferromagnetic ground state with ferromagnetic coupling both within the layers and between the layers, but a mixed state with ferromagnetic coupling within the layers but antiferromagnetic coupling between the layers is only 3 meV above it in energy. For the $P2_1/c$ cell, the ferromagnetic ground state is again lowest, but an antiferromagnetic state is only 5meV above it. A similar result is obtained for the *P2/c* cell (which is the one that shows disproportionation of Ni^{3+}) but here, the antiferromagnetic state is only 3 meV above the ferromagnetic ground state. Although the figures apparently predict a ferromagnetic ground state two points should be noted. First, the density functional calculations are not accurate to a few meV. Second, 1 meV (in terms of *kT*) corresponds to about 11 K. The calculations are entirely consistent with the great magnetic complexity observed.

3.5 Conclusions

First, it is demonstrated that the hole induced by lithium doping in NiO predominately localises on a Ni ion that is second-neighbour to Li, with some partial density on the surrounding oxide ions. The lithium dopant acts not only as an acceptor, but the relaxation of lithium ions also amplifies the Jahn-Teller distortion around the Ni^{3+} ion, which then functions as a carrier trap. This shows the necessity of including the effect of the lithium ion explicitly. Unlike excitation, where the short lifetime does not allow the lattice time to respond, the physical hole doping is often coupled with lattice distortion and results in the formation of a small polaron. It is therefore not sufficient simply to consider the number of holes that are present at a given level of lithium doping in an otherwise perfect NiO lattice. The oxygen contribution to the hole states is a consequence of covalency between the Ni 3d and O 2p orbitals, which results in the appearance of the new peak in oxygen absorption spectra. The Ni is hence best described as oxidised from 2+ to 3+ and a strong Jahn-Teller distortion is found as expected. And the proposed charge state $Li^{+}Ni^{2+}(O_2)^{1.5-}$ can now be excluded.

A new ground state crystal structure with *P2/c* space group symmetry is predicted. In this cell, the charge disproportionation reaction $2Ni^{3+} \rightarrow Ni^{2+} + Ni^{4+}$ occurs which gives two groups of Ni-O bond lengths and the experimentally observed semiconducting behaviour. As a result, the ground state valency of Ni ions should be half 2+ and half 4+ charge state. Also the *P2/c* cell is consistent with the slight monoclinic distortion found at low temperature (10 K). Therefore the absence of cooperative Jahn-Teller distortion is well justified by this cell. Nonetheless, since the energy difference between two mechanisms is extremely small, and we cannot exclude the possibility that a trimer ordered system, stabilised by local (but still mesoscale) curvature is important. Our results do exclude the possibility that a space group incorporating the trimer ordering can be the ground state configuration. This supports the hypothesis that the mechanism by which individual nickel ions remove orbital degeneracy could easily be influenced by its local environment. This is probable since the various ways of ordering the Jahn-Teller distorted Ni^{3+} ions are all likely to involve significant strain effects caused by local distortion.

In real samples, due to thermal effect and impurities, both Jahn-Teller distortion and charge disproportionation may occur and the nickel valency could be a mixture of 2+, 3+ and 4+. Ni^{4+} would be expected to show an unusually short Ni-O bond length. This is seen in some of charge-ordered nickelates (see Table 3-3) and occasionally elsewhere[53].

Since Ni^{4+} has a very low magnetic moment, this provides an alternative method for relieving the magnetic frustration expected in this compound but our calculations are not accurate enough to predict the ground magnetic state of the system unambiguously.

Finally, we have illustrated the difference between $LiNiO_2$ and $NaNiO_2$. In $NaNiO_2$, there is only one dominant mechanism which is Jahn-Teller distortion. Here it is comparably easy to determine its ground state crystal and electronic structure without any dispute. The different case of $LiNiO_2$, where a number of different possible ground states are very close in energy, illustrates how two systems which are apparently so similar chemically, can nevertheless have very different behaviour.

References

1. Kanno, R., et al., *Phase Relationship and Lithium Deintercalation in Lithium Nickel Oxides.* Journal of Solid State Chemistry, 1994. **110**(2): p. 216-225.

2. Pouillerie, C., E. Suard, and C. Delmas, *Structural Characterization of* $Li_{1-z-x}Ni_{1+z}O_2$ *by Neutron Diffraction.* Journal of Solid State Chemistry, 2001. **158**(2): p. 187-197.

3. Kuiper, P., et al., *Character of Holes in* $Li_xNi_{1-x}O$ *and Their Magnetic Behavior.* Physical Review Letters, 1989. **62**(2): p. 221-224.

4. Uchimoto, Y., H. Sawada, and T. Yao, *Changes in electronic structure by Li ion deintercalation in* $LiNiO_2$ *from nickel L-edge and O K-edge XANES.* Journal of Power Sources, 2001. **97–98**(0): p. 326-327.

5. Zaanen, J., G.A. Sawatzky, and J.W. Allen, *Band gaps and electronic structure of transition-metal compounds.* Physical Review Letters, 1985. **55**(4): p. 418-421.

6. Schuler, T.M., et al., *Character of the insulating state in NiO: A mixture of charge-transfer and Mott-Hubbard character.* Physical Review B, 2005. **71**(11): p. 115113.

7. Sawatzky, G.A. and J.W. Allen, *Magnitude and Origin of the Band Gap in NiO.* Physical Review Letters, 1984. **53**(24): p. 2339-2342.

8. Fujimori, A. and F. Minami, *Valence-band photoemission and optical absorption in nickel compounds.* Physical Review B, 1984. **30**(2): p. 957-971.

9. Szotek, Z., W.M. Temmerman, and H. Winter, *Application of the self-interaction correction to transition-metal oxides.* Physical Review B, 1993. **47**(7): p. 4029-4032.

10. Massidda, S., et al., *Quasiparticle energy bands of transition-metal oxides within a model GW scheme.* Physical Review B, 1997. **55**(20): p. 13494-13502.

11. Antolini, E., $Li_xNi_{1-x}O$ *(0≤x≤0.3) solid solutions: formation, structure and transport properties.* Materials Chemistry and Physics, 2003. **82**(3): p. 937-948.

12. Goodenough, J.B., D.G. Wickham, and W.J. Croft, *Some magnetic and crystallographic properties of the system* $Li^{+}_{x}Ni^{++}_{1-2x}ni^{+++}_{x}O$. Journal of Physics and Chemistry of Solids, 1958. **5**(1–2): p. 107-116.

13. Reynaud, F., et al., *Orbital Frustration at the Origin of the Magnetic Behavior in $LiNiO_2$.* Physical Review Letters, 2001. **86**(16): p. 3638-3641.

14. Pickering, I.J., et al., *Nickel K-edge x-ray absorption fine structure of lithium nickel oxides.* Journal of the American Chemical Society, 1993. **115**(10): p. 4137-4144.

15. Mackrodt, W.C., et al., *Direct evidence of O(p) holes in Li-doped NiO from Hartree-Fock calculations.* Chemical Physics Letters, 1996. **250**(1): p. 66-70.

16. Mackrodt, W.C. and D.S. Middlemiss, *A hybrid Hartree–Fock density functional theory study of $Li_xNi_{1-x}O$.* Journal of Physics: Condensed Matter, 2004. **16**(27): p. S2811.

17. de P. R. Moreira, I., F. Illas, and R.L. Martin, *Effect of Fock exchange on the electronic structure and magnetic coupling in NiO.* Physical Review B, 2002. **65**(15): p. 155102.

18. Tran, F., et al., *Hybrid exchange-correlation energy functionals for strongly correlated electrons: Applications to transition-metal monoxides.* Physical Review B, 2006. **74**(15): p. 155108.

19. Kuneš, J., et al., *Local correlations and hole doping in NiO: A dynamical mean-field study.* Physical Review B, 2007. **75**(16): p. 165115.

20. Krukau, A.V., et al., *Influence of the exchange screening parameter on the performance of screened hybrid functionals.* The Journal of Chemical Physics, 2006. **125**(22): p. 224106-5.

21. Dudarev, S.L., et al., *Electron-energy-loss spectra and the structural stability of nickel oxide: An LSDA+U study.* Physical Review B, 1998. **57**(3): p. 1505-1509.

22. Rohrbach, A., J. Hafner, and G. Kresse, *Molecular adsorption on the surface of strongly correlated transition-metal oxides: A case study for CO/NiO(100).* Physical Review B, 2004. **69**(7): p. 075413.

23. Kresse, G. and J. Furthmüller, *Efficient iterative schemes for ab initio total-energy calculations using a plane-wave basis set.* Physical Review B, 1996. **54**(16): p. 11169-11186.

24. Bartel, L.C. and B. Morosin, *Exchange Striction in NiO.* Physical Review B, 1971. **3**(3): p. 1039-1043.

25. Alperin, H.A., *NiO magnetic moments.* J. Phys. Soc. Jpn. Suppl. B (3), 1962. **17**: p. 12.

26. Fender, B.E.F., A.J. Jacobson, and F.A. Wedgwood, *Covalency Parameters in MnO, α-MnS, and NiO.* J. Chem. Phys., 1968. **48**: p. 990-994.

27. Cheetham, A.K. and D.A.O. Hope, *Magnetic ordering and exchange effects in the antiferromagnetic solid solutions* $Mn_xNi_{1-x}O$. Physical Review B, 1983. **27**(11): p. 6964.

28. Hüfner, S., et al., *Photoemission and inverse photoemission spectroscopy of NiO.* Solid State Communications, 1984. **52**(9): p. 793-796.

29. Dobysheva, L.V., P.L. Potapov, and D. Schryvers, *Electron-energy-loss spectra of NiO.* Physical Review B, 2004. **69**(18): p. 184404.

30. Reinert, F., et al., *Electron and hole doping in NiO.* Zeitschrift fur Physik B Condensed Matter, 1995. **97**(1): p. 83-93.

31. Jahn, H.A. and E. Teller, *Stability of Polyatomic Molecules in Degenerate Electronic States. I. Orbital Degeneracy.* Proceedings of the Royal Society of London. Series A - Mathematical and Physical Sciences, 1937. **161**(905): p. 220-235.

32. Rougier, A., C. Delmas, and A.V. Chadwick, *Non-cooperative Jahn-Teller effect in* $LiNiO_2$*: An EXAFS study.* Solid State Communications, 1995. **94**(2): p. 123-127.

33. Chung, J.H., et al., *Local structure of* $LiNiO_2$ *studied by neutron diffraction.* Physical Review B, 2005. **71**(6): p. 064410.

34. Montoro, L.A., et al., *Electronic structure of the transition metal ions in* $LiCoO_2$, $LiNiO_2$ *and* $LiCo_{0.5}Ni_{0.5}O_2$. Chemical Physics Letters, 1999. **309**(1–2): p. 14-18.

35. Yoon, W.-S., et al., *Changes in electronic structure of the electrochemically Li-ion deintercalated* $LiNiO_2$ *system investigated by soft X-ray absorption spectroscopy.* Journal of Power Sources, 2006. **163**(1): p. 234-237.

36. Molenda, J., P. Wilk, and J. Marzec, *Structural, electrical and electrochemical properties of* $LiNiO_2$. Solid State Ionics, 2002. **146**(1–2): p. 73-79.

37. Anisimov, V.I., J. Zaanen, and O.K. Andersen, *Band theory and Mott insulators: Hubbard U instead of Stoner I.* Physical Review B, 1991. **44**(3): p. 943-954.

38. Petit, L., et al., *Ground State Valency and Spin Configuration of the Ni Ions in Nickelates.* Physical Review Letters, 2006. **97**(14): p. 146405.

39. Mazin, I.I., et al., *Charge Ordering as Alternative to Jahn-Teller Distortion.* Physical Review Letters, 2007. **98**(17): p. 176406.

40. García-Muñoz, J.L., et al., *Neutron-diffraction study of $RNiO_3$ (R=La,Pr,Nd,Sm): Electronically induced structural changes across the metal-insulator transition.* Physical Review B, 1992. **46**(8): p. 4414-4425.

41. García-Muñoz, J.L., et al., *Structure and charge order in the antiferromagnetic band-insulating phase of $NdNiO_3$.* Physical Review B, 2009. **79**(13): p. 134432.

42. Alonso, J.A., et al., *Room-temperature monoclinic distortion due to charge disproportionation in $RNiO_3$ perovskites with small rare-earth cations (R=Ho, Y, Er, Tm, Yb, and Lu): A neutron diffraction study.* Physical Review B, 2000. **61**(3): p. 1756-1763.

43. Alonso, J.A., et al., *Charge Disproportionation in $RNiO_3$ Perovskites: Simultaneous Metal-Insulator and Structural Transition in $YNiO_3$.* Physical Review Letters, 1999. **82**(19): p. 3871-3874.

44. Wawrzyńska, E., et al., *Charge disproportionation and collinear magnetic order in the frustrated triangular antiferromagnet $AgNiO_2$.* Physical Review B, 2008. **77**(9): p. 094439.

45. Yang, X., et al., *Highly Swollen Layered Nickel Oxide with a Trilayer Hydrate Structure.* Chemistry of Materials, 2007. **20**(2): p. 479-485.

46. Zhou, F., et al., *First-principles prediction of redox potentials in transition-metal compounds with LDA+U.* Physical Review B, 2004. **70**(23): p. 235121.

47. Chen, Z., et al., *First-principle investigation of Jahn–Teller distortion and topological analysis of chemical bonds in $LiNiO_2$.* Journal of Solid State Chemistry, 2011. **184**(7): p. 1784-1790.

48. Wawrzyńska, E., et al., *Orbital Degeneracy Removed by Charge Order in Triangular Antiferromagnet $AgNiO_2$.* Physical Review Letters, 2007. **99**(15): p. 157204.

49. Yamamoto, S. and T. Fujiwara, *Charge and Spin Order in $RNiO_3$ (R=Nd, Y) by LSDA+U Method.* J. Phys. Soc. Jpn., 2002. **71**: p. 1226.

50. Jeng, H.-T., G.Y. Guo, and D.J. Huang, *Charge-Orbital Ordering and Verwey Transition in Magnetite.* Physical Review Letters, 2004. **93**(15): p. 156403.

51. Cao, J., et al., *Local trimer orbital ordering in* $LiNiO_2$ *studied by quantitative convergent beam electron diffraction technique.* Solid State Ionics, 2009. **180**(20-22): p. 1209-1214.

52. Sugiyama, J., et al., *Low-temperature magnetic properties and high-temperature diffusive behavior of* $LiNiO_2$ *investigated by muon-spin spectroscopy.* Physical Review B, 2010. **82**(22): p. 224412.

53. Mansour, A.N., L. Croguennec, and C. Delmas, *A unique structure of Ni(III) in* $LiNi_{0.3}Co_{0.7}O_2$ *without Jahn-Teller distortion.* Electrochemical and Solid State Letters, 2005. **8**(10): p. A544-A548.

Chapter 4

Cation ordering in $LiMO_2$ compounds (M=V, Cr, Mn, Fe, Co, Ni) explained by exchange interactions

4.1 Introduction to crystal structures of $LiMO_2$ compounds

Compounds with formula $LiMO_2$ (where M is a first row transition metal) have attracted great interest due to their application in rechargeable lithium ion batteries. As introduced in chapter 1, the structure of the $LiMO_2$ compounds is the key to their electrochemical performance as cathodes. Only those with the layered structure display good electrochemical activities. It is therefore essential to understand the factors that influence the structure in $LiMO_2$.

Several polymorphs of $LiMO_2$ exist, which differ in the cation ordering. $LiVO_2$, $LiCrO_2$ and $LiCoO_2$ crystallize in a layered structure with space group symmetry $r\bar{3}m$[1-3]. Although $LiNiO_2$ is also often reported to have a layered structure, there is always a considerable amount of Ni present in the Li layer[4]. The stable structure of $LiMnO_2$

is orthorhombic with space group symmetry pmm[5]. The unique cation ordering in $LiMnO_2$ is believed to originate from the strong Jahn-Teller distortion of the Mn^{3+} ion. A metastable layered $LiMnO_2$ structure has been synthesised by an ion-exchange method[6]. Even in this case 10% of Mn was found to be present in the Li layers. $LiFeO_2$ exists in various crystalline structures[7, 8]. The cation-ordered tetragonal γ-$LiFeO_2$ is known to be the stable form of $LiFeO_2$. The cation-disordered cubic α-$LiFeO_2$ can be obtained by heating γ-$LiFeO_2$ above 600° and there is an intermediate β-$LiFeO_2$ between the α and γ phases. Many other metastable phases have also been obtained by low-temperature synthesis methods[9-11].

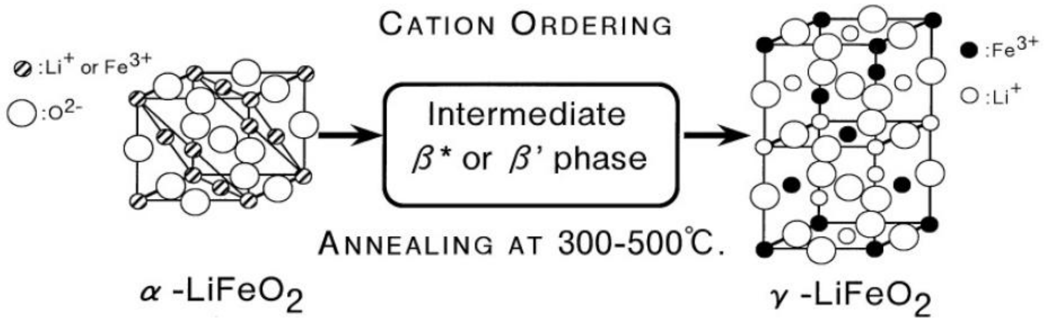

Figure 4-1: The phase relationship of $LiFeO_2$. Image taken from[12].

The structure variation in ionic compounds is usually explained by the ionic size effect. However since first row M^{3+} ions are all smaller than Li^+, if only the ionic size effect is taken into account, all $LiMO_2$ should have the same cation arrangement. Also given the similar ionic sizes of these M^{3+} ions, it is clear that the different arrangements of cations in $LiMO_2$ cannot be justified simply by the argument in terms of size effect. For example the ionic radii of V^{3+} and high-spin Fe^{3+} are given by Shannon[13] to be 0.64 Å and 0.645 Å respectively. The tiny 0.05 Å difference in size does not give a clear demarcation of the dramatically difference in cation arrangements in $LiVO_2$ and $LiFeO_2$. Also from table 4-1 there is clearly no correlation between the calculated M^{3+} - O^{2-} bond lengths and the stability of a particular phase.

Table 4-1: M^{3+} - O^{2-} bond lengths from our calculations discussed below and the stable phase of $LiMO_2$

	M^{3+} - O^{2-} (Å)	Stable $LiMO_2$ structure
V^{3+}	2.06	Layered
High-spin Fe^{3+}	2.05	γ-$LiFeO_2$
Cr^{3+}	2.03	Layered
Low-spin Co^{3+}	1.94	Layered

There has been one previous theoretical study attempting to explain the structural variation of $LiMO_2$ compounds[14]. In the study, an ionic model with pair-wise Buckingham potentials was used. By altering the parameters in the model and assigning different compounds arbitrarily to regions in the parameter space, it was concluded that the size and charge have effects on the structural stability. This argument derived from the ionic model is certainly not faulty. However as we have demonstrated above, it cannot explain the structural difference between layered

$LiVO_2$ and γ-$LiFeO_2$. First it is not adequate to describe transition metal oxides with an ionic model due to the considerable amount of covalency between metal and oxygen. Moreover the electronic effect such as Jahn-Teller distortion cannot be captured by simple pair potentials. Even if the ionic model can truly describe $LiMO_2$ compounds, correct parameters in the model are required to reproduce accurate interatomic interactions. Whether the parameters used in that study can represent $LiMO_2$ compounds or not is a question. Therefore the conclusion from the arbitrary assignment of parameters is only an artefact. Second and most importantly, the ordered γ-$LiFeO_2$ phase was not considered in that study.

4.2 Phase stabilities of $LiMO_2$

4.2.1 Computational details

In order to investigate the structural variation, lattice energies of $LiMO_2$ (M=Al, V, Cr, Mn, Fe, Co, Ni) are calculated with three different cation arrangements shown in figure 4-2, the layered, γ and o orderings. The cell of layered $LiMO_2$ (M=Al, V, Cr, Co) has space group symmetry $R\overline{3}/m$. Layered $LiMnO_2$ shows a monoclinic distortion which lowers its symmetry to C2/m. For layered $LiNiO_2$ the potential ground state cell with space group symmetry $P2_1/c$ considered in chapter 3 is adopted[15]. The γ and o cation orderings are the cation orderings in γ-$LiFeO_2$ and orthorhombic $LiMnO_2$, with space group symmetry $I4_1/amd$ and pmnm respectively. In addition, the lattice energies of $NaAlO_2$ with the three different cation arrangements are also calculated to investigate the influence of size difference between Li^+ and Na^+.

In the layered cation arrangement, the triangular M^{3+} sublattice could cause frustration and therefore only the ferromagnetic coupling between M^{3+} ions is calculated for simplicity. In cells with γ and o cation ordering, antiferromagnetic structures are adopted from those determined by neutron diffraction studies[5, 16].

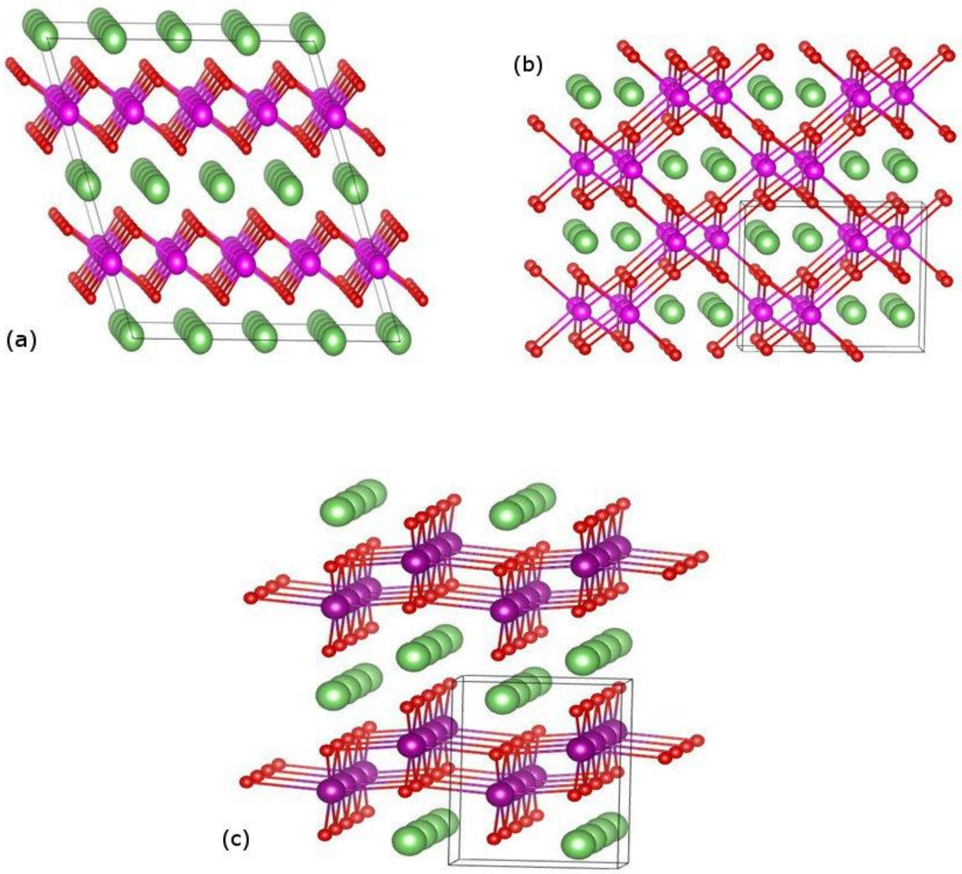

Figure 4-2: $LiMO_2$ with three different cation arrangements. The (a) Layered (b) γ and (c) o arrangements. Green, purple and red spheres denote Li, M and oxygen respectively.

All calculations are based on density functional theory in combination with the projector augmented wave (PAW) method[17] implemented in the Vienna ab initio simulation package (VASP)[18]. The Perdew-Burke-Ernzerhof exchange-correlation functional[19] is used and a Hubbard model U_{eff} correction[20] is applied to d electrons to account for energy associated with the on-site coulomb repulsion. All $LiMO_2$ structures are calculated with the same value 4.5 eV of U_{eff} on the d electrons of M^{3+}. The plane wave energy-cutoff is set to 500 eV for good convergence in lattice energies. For all cells, the *k*-point spacing is less than 0.05 $Å^{-1}$ in the Brillouin zone. All atomic positions in the cell and the lattice are free to relax until the residual force acting on each ion is less than 0.01 eV/ Å.

4.2.2 Results and discussion

Figure 4-3 shows the calculated stabilities of $LiMO_2$ compounds with the γ and o cation arrangement both in ferro- and anti-ferromagnetic states, relative to the layered cation arrangement. As shown in the figure only two compounds, $LiMnO_2$ and $LiFeO_2$, stabilise in phases other than the layered cation ordering. The rest of the compounds are stabilised in the layered structure. All experimentally observed stable structures of $LiMnO_2$ compounds are correctly predicted in our calculations apart from $LiMnO_2$. As seen in figure 4-3 $LiMnO_2$ is calculated to be most stable with the γ cation arrangement in the ferromagnetic state, which contradicts the experimentally observed o-$LiMnO_2$ structure. This issue will be addressed below.

Above all, a dramatic energy difference of about 200 meV between the ferromagnetic (FM) and antiferromagnetic (AF) configurations in $LiFeO_2$ with the γ cation arrangement is noted. There are also about 100 meV energy differences between the FM and AF configuration in $LiFeO_2$ and $LiMnO_2$ with the o cation arrangement. These numbers indicate strong exchange interactions between Fe^{3+} ions and between Mn^{3+} ions. In addition as seen in figure 4-3, $LiFeO_2$ would be stabilised in the layered structure if spins on Fe^{3+} are forced to align ferromagnetically. This suggests the possibility that the exchange interaction is the reason for $LiMnO_2$ and $LiFeO_2$ deviating from the layered structure. Therefore this prompted the investigation on the exchange interaction between transition metal ions discussed below.

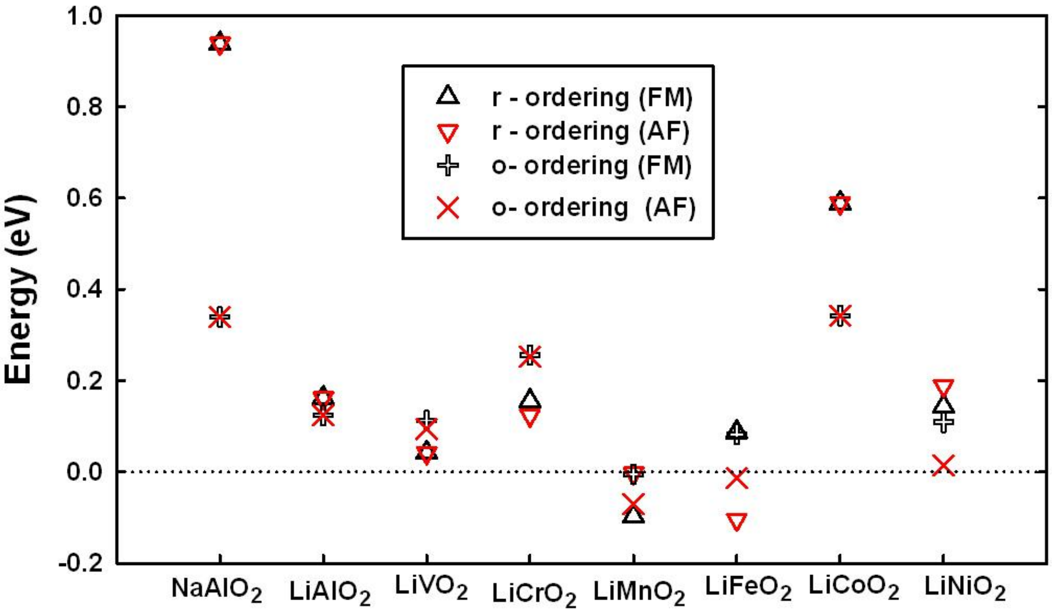

Figure 4-3: Calculated lattice energies of $LiMO_2$ with γ and o ordering relative to the layered ordering (ferromagnetic).

4.3 Exchange interactions between octahedrally coordinated transition metal ions

The exchange interaction is a quantum mechanical phenomenon arising from the overlap of wavefunctions (orbitals) which is responsible for magnetic behaviours in many materials such as the antiferromagnetic magnetic ordering and the trend of Neel temperature in first-row transition metal monoxides. In an insulating crystalline material where electrons are localised, the exchange interaction between magnetic moments on individual lattice site can be treated with the Heisenberg Hamiltonian:

$$\boldsymbol{H}_{Heis} = -\sum_{i,j} J_{ij}\boldsymbol{S}_i \cdot \boldsymbol{S}_j \tag{4-1}$$

where $\boldsymbol{S}_i$ and $\boldsymbol{S}_j$ are the spin operators at the i_{th} and j_{th} lattice sites, and J_{ij} is the exchange constant between $\boldsymbol{S}_i$ and $\boldsymbol{S}_j$. One can expect that in materials where such exchange interaction exists, there is ***an energy gain through the exchange interaction*** which should be included in the total lattice energy.

In oxides with the rock-salt structure, as illustrated in figure 4-4, the interaction between nearest-neighbour (NN) metal ions is denoted as J_1. This interaction J_1 can be understood as a result of direct orbital overlap between nearest neighbouring transition metal ions. In addition, there is a considerable magnitude of interaction between 2nd-nearest-neighbour (2NN) metals ions, denoted as J_2 in figure 4-4. This is quite unexpected since the distance between 2nd nearest neighbours is too large for any effective orbital overlap. To explain this, the superexchange mechanism was proposed[21].

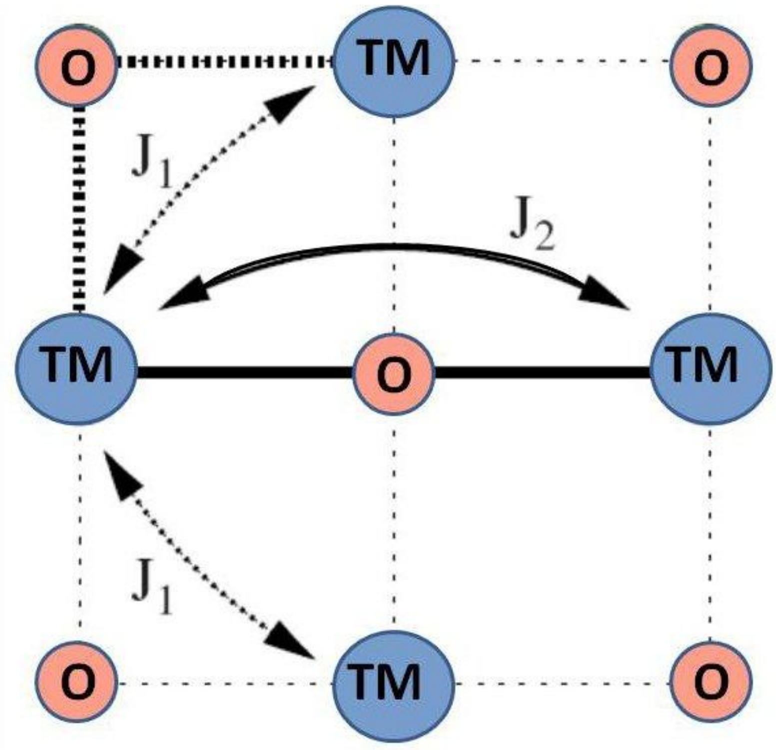

Figure 4-4: Interactions between transition metal ions in the rock-salt structure.

The superexchange interaction occurs between two transition metal ions separated by an anion. In transition metal oxides, 3d orbitals on metal ions overlap considerably with oxygen 2p orbitals. It can be seen in many experimental and theoretical studies in transition metal oxides that the doped electrons or holes often exhibit both 2p and 3d characters. Li doped NiO, considered in chapter 3 is a good example. Due to such orbital overlapping, electrons can then virtually transfer between transition metal ions mediated by oxygen, which is the origin of the superexchange interaction.

The interactions J_1 and J_2 have a strong dependence on the electronic configurations of transition metal ions. Goodenough[22] and Kanamori[23] summarised the interactions using semi-empirical rules based on the symmetry relation of orbitals. Generally J_1 is strong when there are half-filled t_{2g} orbitals, which allows the direct overlapping between t_{2g} orbitals of NN metal ions. Although the 90° metal-oxygen-metal superexchange is also possible and can contribute to J_1, it is rather weak. J_2 comes predominately from the 180° metal-oxygen-metal superexchange mediated by oxygen since the distance is large between transition metals and therefore there is only insignificant direct d orbital overlapping. J_2 is strong when there are half-filled e_g orbitals because the lobes of e_g orbitals point towards p orbitals which results in large overlap between metal 3d and oxygen 2p orbitals. While the Goodenough-Kanamori rule has given correct predictions of the sign of exchange interactions in various materials, it does not provide a clear indication on the magnitude.

As mentioned in the previous section, we suspect that the exchange interaction has an influence on the structural variation in $LiMO_2$ compounds. Here through calculating the magnitude of exchange interaction between transition metal ions we are going to show that the energy associated with exchange interactions, often considered secondary, can indeed have an impact on the crystal structure. And then we further discuss the structural variation of the $LiMO_2$ compounds.

4.3.1 Computational details

In order to probe the exchange interaction and its influence on site preferences, pairs of transition metal ions V^{2+} ($t_{2g}^3e_g^0$), high-spin Mn^{2+} ($t_{2g}^3e_g^2$), high-spin Fe^{3+} ($t_{2g}^3e_g^2$) and Ni^{2+} ($t_{2g}^6e_g^2$) are embedded in a 4x4x4 MgO cell with two different arrangements. As shown in figure 4-5, in the NN cell the transition metal ion pair is located as nearest neighbours in two edge sharing MO_6 octahedra. In the 2NN cell the transition metal ion pair is located as 2nd nearest neighbours in two corner sharing MO_6 octahedra. The choice of those four ions is because they do not exhibit orbital degeneracy. In transition metal oxides, ions with degenerate orbitals usually undergo Jahn-Teller distortion and the orbital degeneracy is lifted. Consequently, if we were to deal with ions with orbital degeneracy, there would be one more degree of freedom entering the problem, the orbital ordering, which would need to be considered. There are two reasons for the choice of MgO. First, Mg^{2+} is nonmagnetic and therefore the exchange interaction is absent between Mg^{2+} ions or between Mg^{2+} and embedded transition metal ions. Consequently the exchange interactions J_1 and J_2 only take place between embedded transition metal ion pairs in the NN and 2NN cell respectively. Second, the size of the Mg^{2+} ion is similar to first row transition metal M^{2+} ions and so ion size effect is minimised.

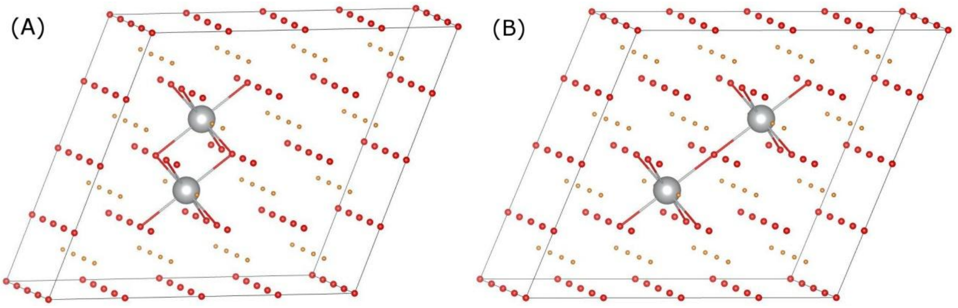

Figure 4-5: The (A) NN cell and (B) 2NN cell of two transition metals embedded in a 4x4x4 MgO cell. The transition metal, Mg and O are denoted in grey, orange and red spheres respectively.

In order to estimate the energy associated with the exchange interactions J_1 and J_2 from the Heisenberg Hamiltonian, total lattice energies of both FM and AF coupling of spins on metal ions are calculated. In our calculations, spins are collinear and restricted to the Z direction and therefore the Heisenberg model can be simplified to the Ising model

$$\boldsymbol{H}_{Ising} = -\sum_{i,j} J_{ij} \boldsymbol{S}_{z_i} \cdot \boldsymbol{S}_{z_j} \tag{4-2}$$

where $\boldsymbol{S}_{z_i}$ and $\boldsymbol{S}_{z_j}$ are the total spins at the i_{th} and j_{th} lattice sites. By applying the Ising Hamiltonian on a crystal where the exchange interaction only act between NN pairs (J_1) and 2NN pairs (J_2), the energy gain can be written as

$$\begin{aligned} E_{ex} &= -J_{NN} n^2 s^2 \sum_{NN} e_i \cdot e_j - J_{2NN} n^2 s^2 \sum_{2NN} e_i \cdot e_j \\ &= -J_1 \sum_{NN} e_i \cdot e_j - J_2 \sum_{2NN} e_i \cdot e_j \end{aligned} \tag{4-3}$$

where J_{NN} and J_{2NN} are the exchange constants between NN and 2NN pairs, n is the number of unpaired electrons at site i (j) and the s is the spin quantum number (for electrons $s = \frac{1}{2}$). The left summation in the equation is over *i,j* between NN pairs, the right summation is over *i,j* between 2NN pairs and e_i, e_j= +1 or -1 (spin up and spin down).

Subsequently the exchange energies J_1 and J_2 can be extracted from total energies of different magnetic configurations[24-26]. In our case only J_1 exists in the NN cell

$$E(AF - FM)_{NN} = 2J_1 \tag{4-4}$$

and similarly J_2 can be obtained from the calculations of the 2NN cell

$$E(AF - FM)_{2NN} = 2J_2 \tag{4-5}$$

Hence $E(AF - FM)_{NN}$ and $E(AF - FM)_{2NN}$ are energy gains resulted from the exchange interactions of the transition metal ion pair in the NN cell and 2NN cell. The larger energy difference between FM and AF states indicates stronger interaction.

All calculations here are performed as described in 4.2.1 except in the charged cell containing Fe^{3+} ions, in which a homogeneous background-charge is applied.

4.3.2 Interactions between transition metal ions and their site preferences

Figure 4-6 shows results of density functional theory calculations for four different transition metal pairs, V^{2+}, Mn^{2+}, Fe^{3+} and Ni^{2+}, embedded in the 4x4x4 MgO cell. Firstly we note that the absolute values of $E(AF-FM)_{NN}$ and $E(AF-FM)_{2NN}$ drop with increasing value of U_{eff}. In the DFT+U method, U_{eff} is introduced to account for the on-site coulomb interaction between electrons. So higher values of U_{eff} give rise to more confined d orbitals (less diffuse) which results in less overlap between metal 3d and oxygen 2p orbitals[20]. Similarly the direct d-d orbital overlap, if it exists, diminishes with increasing U_{eff}. Since the interactions J_1 and J_2 depend on the extent of orbital overlap, they are expected to weaken as U_{eff} increases. This is indeed supported by the decreasing absolute values of $E(AF-FM)_{NN}$ and $E(AF-FM)_{2NN}$ seen in our results.

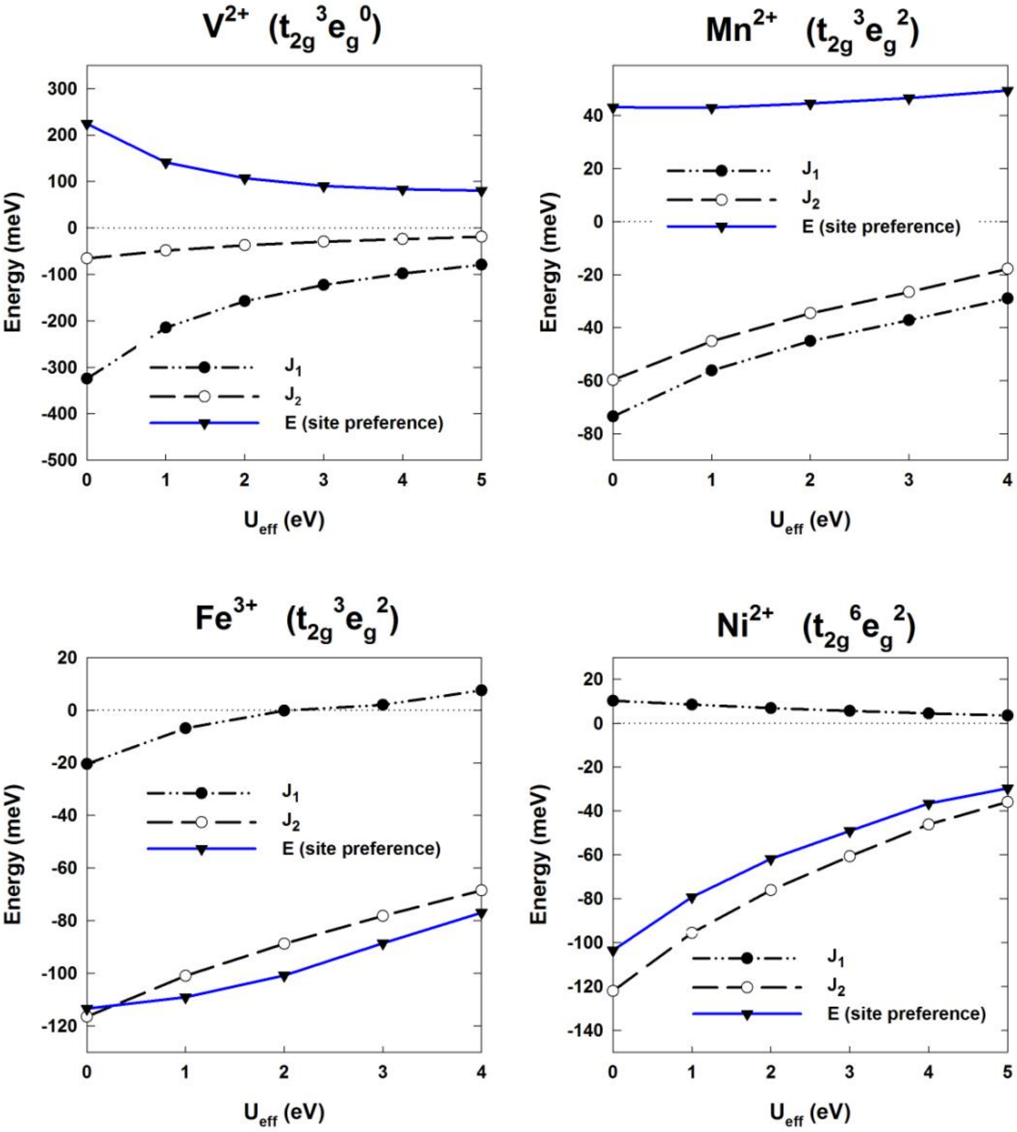

Figure 4-6: The calculated energies versus U$_{eff}$ of the four cases. Note that in the Fe^{3+} case, the energies do not exhibit a convergent/asymptotic behaviour as in other three cases. This might be a consequence of the calculated cell being charged and the choice of method used by VASP to attempt to correct for this.

$E(2NN - NN)$, termed as the site preference energy, is the energy difference between the favoured spin configuration (lower in energy) of the NN cell and 2NN cell. In other words, if $E(2NN - NN)$ is positive, the lattice energy of the 2NN cell is lower and therefore the transition metal ion pair prefers to stay as nearest neighbours. Conversely, if $E(2NN-NN)$ is negative, the 2NN cell is more stable and that means the pair of transition metal ions prefers to stay as 2nd nearest neighbours. Such site preferences certainly involve a size effect, i.e. the size difference between Mg^{2+} and the embedded transition metal ions, but also, we propose, from the difference in energy gain through J_1 in the NN cell and J_2 in the 2NN cell (relative strength). Therefore the site preference energy should contains two contributions and is written as

$$\begin{aligned} &E(2NN-NN) \\ &\qquad = \{|E(AF-FM)_{NN}| - |E(AF-FM)_{2NN}|\} \\ &\qquad + E(size) \end{aligned} \tag{4-6}$$

The term in the curly brackets is the contribution from interactions between transition metal ions, denoted as $E(interaction)$ in figure 4-7 and $E(size)$ is the contribution from the size effect. From the relationships between $|E(2NN-NN|$, $|E(interaction)|$, and $|E(size)|$ in figure 4-7, it can be seen that the energies associated with the size effect are no more than 40 meV, due to the comparable ionic radii between Mg^{2+} (0.72 Å), V^{2+} (0.79 Å), Mn^{2+} (0.83 Å), Fe^{3+} (0.645 Å) and Ni^{2+} (0.69 Å). Moreover they are not sensitive to U_{eff}. Since the size effect is small and usually not significant, the contribution arising from the relative strength in J_1 and J_2 could become the dominating factor in the site preference energy. As seen in figure 4-7, $|E(2NN-NN)|$ is highly correlated with $|E(interaction)|$ apart from the case of Mn^{2+} in which the strengths of J_1 and J_2 are similar.

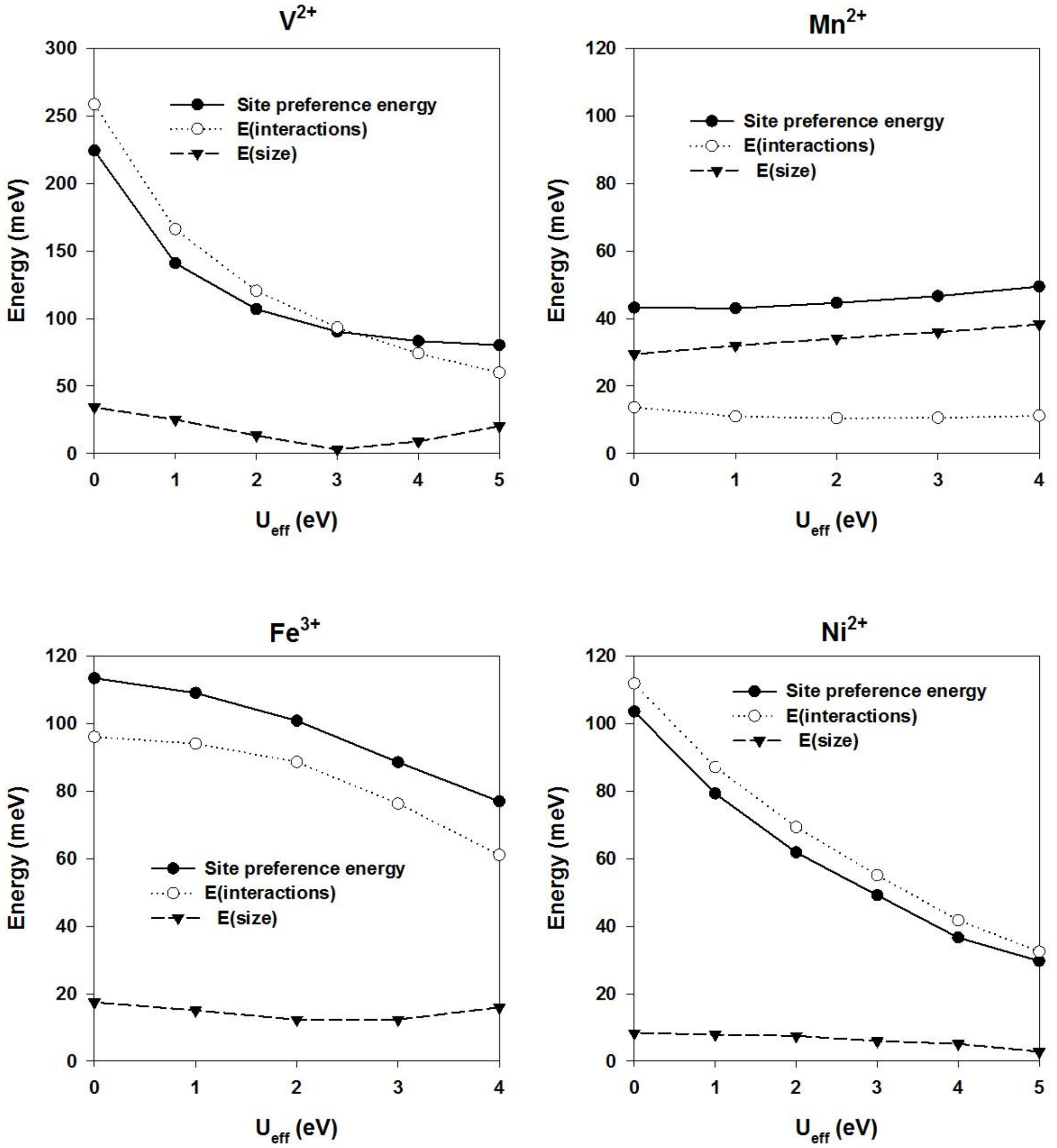

Figure 4-7: The correlation between the site preference energy, E(interaction) and E(size).

As seen in figure 4-6, in the case of V^{2+} ($t_{2g}^{3}e_{g}^{0}$), the large value of E(AF-FM)$_{NN}$ indicates strong J$_1$, resulted from the direct overlap of half-filled t_{2g} orbitals. Compared to E(AF-FM)$_{NN}$, E(AF-FM)$_{2NN}$ is much smaller. Overall, the NN cell is lower in energy due to larger energy gain through J_1 and therefore the V^{2+} pair strongly prefers to stay as nearest neighbours. Interestingly, as shown in figure 4-8, such strong J_1 interaction in the NN cell is accompanied by the shortening in the V^{2+}-V^{2+} distance in the AF state compared to the FM state. This "V^{2+}-V^{2+} dimerization" is similar to the dimerization of Ti^{3+} ions seen in $NaTiSi_2O_6$[27] and $MgTi_2O_4$[28]. In those compounds, Ti^{3+} ions also have half-filled t_{2g} orbitals and are located at octahedral sites sharing common edges, the same as V^{2+} pairs in the NN cell.

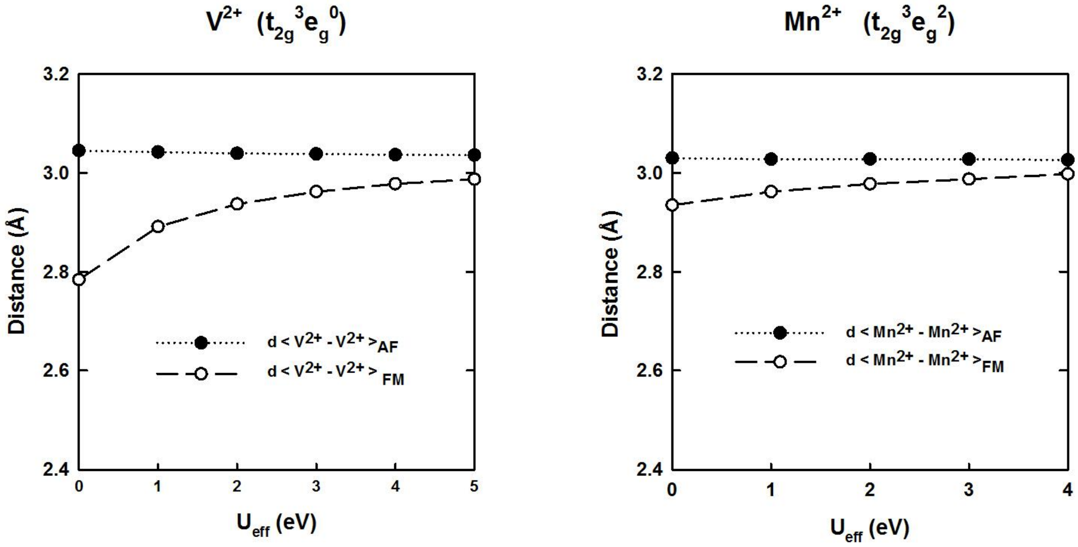

Figure 4-8: The M-M distance in FM and AF states in the NN cell.

In the case of Mn^{2+}, from figure 4-8 there is also a difference in the Mn^{2+}-Mn^{2+} distance in the NN cell between FM and AF states in combination with a noticeably large J_1. Nevertheless, as seen in figure 4-6 the magnitude of $E(AF\text{-}FM)_{NN}$ is much smaller than in the V^{2+} case which makes $E(AF\text{-}FM)_{NN}$ and $E(AF\text{-}FM)_{2N}$ comparable

(The energy gains through J_1 and J_2 are similar). The NN cell is energetically more favourable than the 2NN cell, although with a much smaller site preference energy than the V^{2+} case. As a result, the Mn^{2+} pair prefers to stay as nearest neighbours in the MgO supercell.

Fe^{3+} ($t_{2g}^3e_g^2$) has the same electronic configuration as Mn^{2+} but with higher valency and smaller ionic radius. The shorter Fe^{3+}-O^{2-} bond length compared to Mn^{2+}-O^{2-} leads to a difference in the crystal field splitting and greater covalency between metal 3d and oxygen 2p orbitals. All these factors can influence the interactions J_1 and J_2. Our results show that J_1 is weakened compared to the Mn^{2+} case while J_2 is enhanced. Also the difference in M-M distance between FM and AF states in the NN cell vanishes, consistent with small J_1. Overall, the 2NN cell is lower in energy due to larger energy gain through J_2 and therefore the Fe^{3+} pair strongly prefers to stay as 2nd nearest neighbours.

In the Ni^{2+} ($t_{2g}^6e_g^2$) case, the t_{2g} orbitals are fully occupied and therefore there should not be overlap between them. Consequently only the 90° Ni^{2+}-O-Ni^{2+} superexchange through the overlap between e_g orbitals of Ni^{2+} and 2p orbitals of oxygen contributes to J_1, which is expected to be weak. This is confirmed by the calculated smaller values of $E(AF\text{-}FM)_{NN}$. In contrast, J_2 is large. Overall, the 2NN cell is lower in energy due to larger energy gain through J_2 and therefore the Ni^{2+} pair strongly prefers to stay as 2nd nearest neighbours.

So far we have demonstrated that strengths of interactions J_1 and J_2 between transition metal ions depend strongly on their electronic configurations. Besides, if the size effect is negligible, when J_1 is stronger than J_2, the energy gain through J_1 in the NN cell is larger than the energy gain through J_2 in the 2NN cell. Therefore the lattice energy of the NN cell is lower and this means that transition metal pairs prefer to stay as nearest neighbours. Conversely, if J_2 is stronger than J_1, the transition metal pair would prefer to stay as 2nd nearest neighbours.

4.4 Explanations for the cation arrangement in $LiMO_2$

Figure 4-9 again shows the stability of $LiMO_2$ with the γ and o cation arrangement both in ferro- and anti-ferromagnetic states, relative to the layered cation arrangement. In both $LiAlO_2$ and $NaAlO_2$, the lattice energies of $LiAlO_2$ and $NaAlO_2$ with the layered cation arrangement are calculated to be lowest and hence most stable. Because $LiAlO_2$ and $NaAlO_2$ are ionic, the only reason for them to be stabilised in the layered strurcture is the size difference between two cations. Also the more significant the size difference between cations, the more stable the layered cation arrangement is. This can be realised by comparing $LiAlO_2$ and $NaAlO_2$. Because the size difference between Na^+ and Al^{3+} is larger than between Li^+ and Al^{3+}, as shown in figure 4-9 $NaAlO_2$ is much more stabilised in the layered cation arrangement than in $LiAlO_2$. In fact due to the pronounced size difference between Na^+ and M^{3+}, all $NaMO_2$ compounds exhibit the layered structure[29-34]. Therefore the size effect is the dominating factor of cation arrangement in $NaMO_2$.

If only the size effect is taken into account, all $LiMO_2$ compounds should prefer the layered cation ion arrangement. If, as we have demonstrated in the previous section, there exists a larger interaction J_2 between M^{3+} ions than J_1, this could drive them to settle as 2nd neighbours and result in a different cation arrangement.

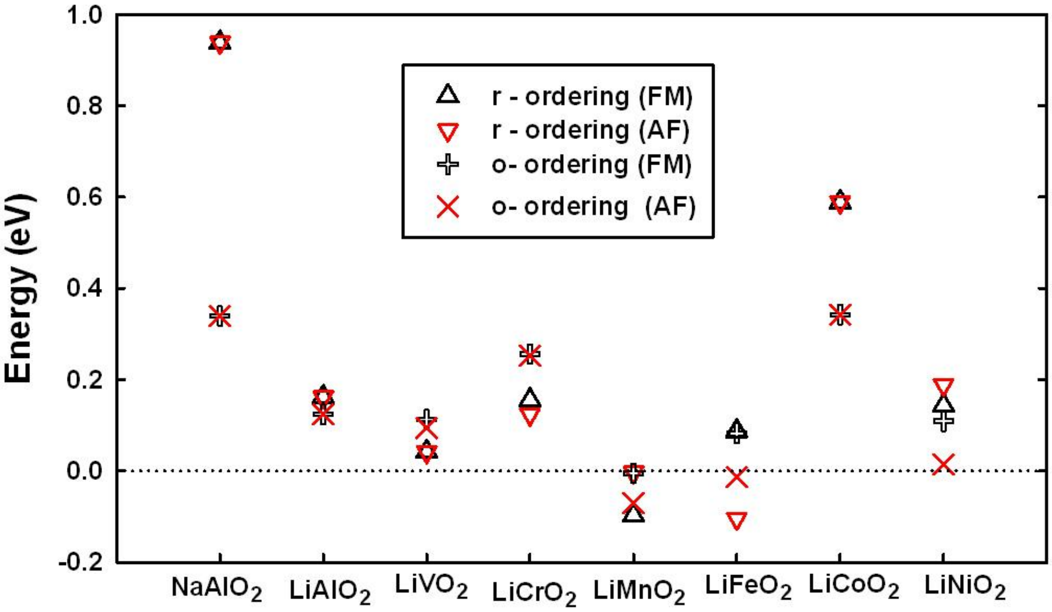

Figure 4-9: Calculated lattice energies of $LiMO_2$ with γ and o ordering relative to the layered ordering (ferromagnetic).

From figure 4-9, $LiVO_2$ and $LiCrO_2$ are predicted to stabilise in the layered structure, in agreement with experiments. The electronic configuration of V^{3+} and Cr^{3+} are $t_{2g}^2e_g^0$ and $t_{2g}^3e_g^0$. The unfilled e_g orbital gives rise to a weak J_2 as indicated by the small energy difference between AF and FM configurations with the γ cation ordering. J_1, which arises from the direct overlap of half-filled t_{2g} orbitals, between V^{3+} ions and Cr^{3+} ions, regardless its strength, would only reinforce the stability of the layered cation arrangement.

It is known that the magnetic coupling between neighbouring pair of V^{3+} in $LiVO_2$ and Cr^{3+} $LiCrO_2$ is anti-ferromagnetic. Therefore one might be concerned about the calculated results which assume ferromagnetic coupling in the layered structure. Indeed it has been reported[35] that the lattice energy is lower in the layered $LiCrO_2$ with the anti-ferromagnetic and ferrimagnetic configurations than for the ferromagnetic configuration. Nonetheless such lowering in the lattice energy would only reinforce the relative stability of the layered cation arrangement. Therefore despite the fact that only ferromagnetic coupling in $LiVO_2$ and $LiCrO_2$ is considered in this study, the calculated relative structural stabilities of $LiVO_2$ and $LiCrO_2$ are correct even though the magnetic states are not.

In $LiFeO_2$, the calculated structural stability indicates that antiferromagnetic γ-$LiFeO_2$ is more stable than phases with the layered and o-$LiMnO_2$ cation arrangements. Indeed although layered $LiFeO_2$[9] and $LiFeO_2$ with the o-$LiMnO_2$ cation arrangement[10] have been synthesised, they are meta-stable. However γ-$LiFeO_2$ with ferromagnetic coupling is less favourable than the layered structure and there is a huge energy difference (about 200 meV) between the AF and FM states as already mentioned earlier. This indicates a strong J_2 interaction between Fe^{3+} ions, which not only results in strong antiferromagnetic coupling but also is the driving force for $LiFeO_2$ to crystallise in the γ-$LiFeO_2$ structure. The γ-$LiFeO_2$

structure is therefore the result of maximising the number of J_2, as seen in table 4-2, and hence obtaining the largest energy gain through the exchange interaction.

Table 4-2: The number of J_1 and J_2 interactions acting on one transition metal ion in the cells with different cation orderings. The positive and negative value means FM and and AF coupling respectively.

	J_1	J_2
Layered	6	0
γ	2, -2	-4
o	2, -4	-2

The situation in $LiMnO_2$ is more complicated. Due to the degenerate electronic configuration of Mn^{3+} ($t_{2g}^3e_g^1$), the MnO_6 octahedron undergoes a strong Jahn-Teller distortion which lifts the orbital degeneracy and its corresponding orbital ordering produces further complexity in the cation interactions. The unique result that the o-$LiMnO_2$ structure observed experimentally is favoured over the layered and γ-$LiFeO_2$ cation arrangement in $LiMnO_2$ can be regarded as the consequence of the collective Jahn-Teller distortions of MnO_6 octahedra and their corresponding orbital ordering. Nevertheless, as seen in figure 4-9 $LiMnO_2$ is calculated to be most stable with the γ cation arrangement in ferromagnetic state, which contradicts the experimentally observed o-$LiMnO_2$ structure. Figure 4-10 shows the calculated phase stabilities with different against U_{eff}, relative to the layered structure, in $LiMnO_2$. The correct phase stability with AF o-$LiMnO_2$ being the most favourable can be reproduced when U_{eff} is less than 3. In addition, the lattice energy between the FM γ-$LiFeO_2$ and AF o-$LiMnO_2$ phases are similar in certain range of U_{eff}, which could be the reason for the often reported high concentration of stacking faults in $LiMnO_2$[36-38]. If we look back to figure 4-2, it not difficult to see that the stacking faults in the o-$LiMnO_2$ structure would indeed result in the γ-$LiFeO_2$ structure.

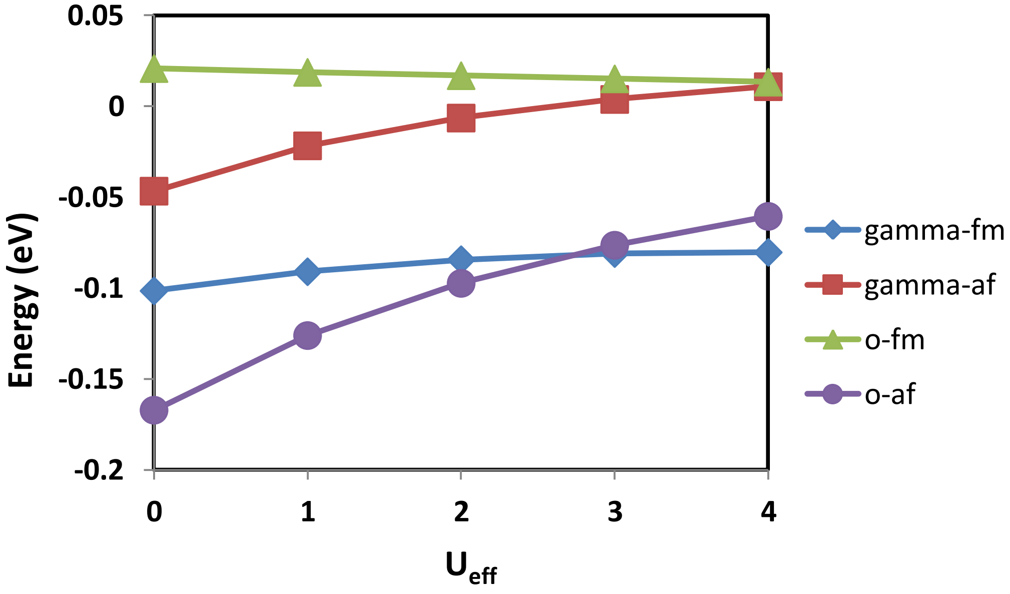

Figure 4-10: Phase stability of $LiMnO_2$.

In $LiCoO_2$, the Co^{3+} ($t_{2g}^6e_g^0$) has fully occupied t_{2g} and empty e_g orbitals. Hence Co^{3+} is nonmagnetic and there is no exchange interaction acting on Co^{3+} ions. However figure 4-8 shows that $LiCoO_2$ is more strongly stabilised in the layered structure than the ionic case $LiAlO_2$, despite the similar ionic size between Co^{3+} (0.545 Å)and Al^{3+} (0.535 Å). The fully occupied t_{2g} orbitals along with the covalence in the Co^{3+}-O^{2-}

bonding result in a strong isotropic tendency of Co^{3+} with rigid CoO_6 octahedron. As seen in table 4-3, due to size difference between Li^+ and Co^{3+}, LiO_6 and CoO_6 octahedra can only both remain undistorted with the layered cation arrangement. Therefore it costs energy for CoO_6 octahedra to be distorted as in phases with the γ and o cation arrangements. This is what makes them very unfavourable compared to layered structure, in addition to the size effect.

In $LiNiO_2$, similar to $LiMnO_2$, the Ni^{3+} ($t_{2g}^6e_g^1$) ion is also Jahn-Teller active due to orbital degeneracy. However $LiNiO_2$ does not exhibit the o-$LiMnO_2$ structure. It is often reported to crystallise in the layered structure, although with considerable amounts of Li-Ni anti-site defects or nonstoichiometry. Nevertheless the calculated lattice energies of the layered $LiNiO_2$ and the antiferromagnetic $LiNiO_2$ with o cation arrangement are very close. This may be responsible for the considerable amount of Li-Ni anti-site defects or nonstoichiometry often reported in $LiNiO_2$. Since the presence of Ni ions in the supposed layered $LiNiO_2$ would to some extent make the cation ordering locally look like that in o-$LiMnO_2$.

Table 4-3: The Li^+ - O^{2-} and Co^{3+} - O^{2-} distance in $LiCoO_2$ with different cation orderings.

	Li^+ - O^{2-} (Å)	***Co^{3+} - O^{2-} (Å)***
Layered	2.11 x 6	1.94 x 6
γ	1.97 x 4 2.36 x 2	1.92 x 2 1.97 x 4
o	1.97 x 2 2.06 x 2 2.38 x 2	1.91 x 2 1.95 x 2 1.96 x 2

4.5 Summary

By embedding first row transition metal ion pairs in the MgO supercell, the dependence of J_1 and J_2 exchange interactions on electronic configuration is demonstrated. Also it is shown that when size effect is not noticeable compared to the effect of exchange interactions, their site preference to stay as nearest neighbours or 2nd nearest neighbours depends on the relative strength of J_1 and J_2 exchange interactions. When the exchange interaction J_1 is stronger (more energy gain), the transition metal pair prefers to stay as nearest neighbours (90° M-O-M). When the exchange interaction J_2 is stronger, the transition metal pair then prefers to stay as 2nd-nearest neighbours (180° M-O-M).

Accordingly, the structural variation of rock-salt $LiMO_2$ is explained. The size difference between Li^+ and M^{3+} as well as J_1 favours the layered structure, as in $LiVO_2$, $LiCrO_2$ and $LiCoO_2$. Whereas in $LiFeO_2$, a significant J_2 exchange interaction arising from half-filled e_g orbitals stabilises M^{3+} in the 180° M-O-M configuration and therefore it does not form the layered structure.

References

1. Cardoso, L.P., et al., *Structural studies of* $Li_{0.7}VO_2$ *in the temperature range 20–300°C.* Journal of Solid State Chemistry, 1988. **72**(2): p. 234-243.

2. Komaba, S., et al., *Electrochemical intercalation activity of layered* $NaCrO_2$ *vs.* $LiCrO_2$*.* Electrochemistry Communications, 2010. **12**(3): p. 355-358.

3. Akimoto, J., Y. Gotoh, and Y. Oosawa, *Synthesis and Structure Refinement of* $LiCoO_2$ *Single Crystals.* Journal of Solid State Chemistry, 1998. **141**(1): p. 298-302.

4. Kanno, R., et al., *Phase Relationship and Lithium Deintercalation in Lithium Nickel Oxides.* Journal of Solid State Chemistry, 1994. **110**(2): p. 216-225.

5. Greedan, J.E., N.P. Raju, and I.J. Davidson, *Long Range and Short Range Magnetic Order in Orthorhombic* $LiMnO_2$*.* Journal of Solid State Chemistry, 1997. **128**(2): p. 209-214.

6. Armstrong, A.R. and P.G. Bruce, *Synthesis of layered* $LiMnO_2$ *as an electrode for rechargeable lithium batteries.* Nature, 1996. **381**(6582): p. 499-500.

7. Tabuchi, M., et al., *Preparation of* $AFeO_2$ *(A = Li, Na) by hydrothermal method.* Solid State Ionics, 1995. **79**(0): p. 220-226.

8. Barré, M. and M. Catti, *Neutron diffraction study of the β' and γ phases of* $LiFeO_2$*.* Journal of Solid State Chemistry, 2009. **182**(9): p. 2549-2554.

9. Shirane, T., et al., *Structure and physical properties of lithium iron oxide,* $LiFeO_2$*, synthesized by ionic exchange reaction.* Solid State Ionics, 1995. **79**(0): p. 227-233.

10. Sakurai, Y., et al., *Low temperature synthesis and electrochemical characteristics of $LiFeO_2$ cathodes.* Journal of Power Sources, 1997. **68**(2): p. 711-715.

11. Matsumura, T., et al., *Synthesis, Structure, and Electrochemical Properties of a New Cathode Material, $LiFeO_2$, with a Tunnel Structure.* Journal of The Electrochemical Society, 2002. **149**(12): p. A1509-A1513.

12. Tabuchi, M., et al., *Effect of Cation Arrangement on the Magnetic Properties of Lithium Ferrites ($LiFeO_2$) Prepared by Hydrothermal Reaction and Post-annealing Method.* Journal of Solid State Chemistry, 1998. **140**(2): p. 159-167.

13. Shannon, R., *Revised effective ionic radii and systematic studies of interatomic distances in halides and chalcogenides.* Acta Crystallographica Section A, 1976. **32**(5): p. 751-767.

14. Wu, E.J., P.D. Tepesch, and G. Ceder, *Size and charge effects on the structural stability of $LiMO_2$ (M = transition metal) compounds.* Philosophical Magazine Part B, 1998. **77**(4): p. 1039-1047.

15. Chen, H., C.L. Freeman, and J.H. Harding, *Charge disproportionation and Jahn-Teller distortion in $LiNiO_2$ and $NaNiO_2$: A density functional theory study.* Physical Review B, 2011. **84**(8): p. 085108.

16. Cox, D.E., et al., *Neutron Diffraction and Mössbauer Study of Ordered and Disordered $LiFeO_2$.* Physical Review, 1963. **132**(4): p. 1547-1553.

17. Kresse, G. and D. Joubert, *From ultrasoft pseudopotentials to the projector augmented-wave method.* Physical Review B, 1999. **59**(3): p. 1758-1775.

18. Kresse, G. and J. Furthmüller, *Efficient iterative schemes for ab initio total-energy calculations using a plane-wave basis set.* Physical Review B, 1996. **54**(16): p. 11169-11186.

19. Perdew, J.P., K. Burke, and M. Ernzerhof, *Generalized Gradient Approximation Made Simple.* Physical Review Letters, 1996. **77**(18): p. 3865-3868.

20. Dudarev, S.L., et al., *Electron-energy-loss spectra and the structural stability of nickel oxide: An LSDA+U study.* Physical Review B, 1998. **57**(3): p. 1505-1509.

21. Anderson, P.W., *Antiferromagnetism. Theory of Superexchange Interaction.* Physical Review, 1950. **79**(2): p. 350-356.

22. Goodenough, J.B., *Direct Cation- -Cation Interactions in Several Oxides.* Physical Review, 1960. **117**(6): p. 1442-1451.

23. Kanamori, J., *Superexchange interaction and symmetry properties of electron orbitals.* Journal of Physics and Chemistry of Solids, 1959. **10**(2–3): p. 87-98.

24. Fischer, G., et al., *Exchange coupling in transition metal monoxides: Electronic structure calculations.* Physical Review B, 2009. **80**(1): p. 014408.

25. de P. R. Moreira, I. and F. Illas, *Ab initio theoretical comparative study of magnetic coupling in $KNiF_3$ and K_2NiF_4.* Physical Review B, 1997. **55**(7): p. 4129-4137.

26. Feng, X. and N.M. Harrison, *Magnetic coupling constants from a hybrid density functional with 35% Hartree-Fock exchange.* Physical Review B, 2004. **70**(9): p. 092402.

27. Popović, Z.S., Ž.V. Šljivančanin, and F.R. Vukajlović, *Sodium Pyroxene $NaTiSi_2O_6$: Possible Haldane Spin-1 Chain System.* Physical Review Letters, 2004. **93**(3): p. 036401.

28. Schmidt, M., et al., *Spin Singlet Formation in $MgTi_2O_4$: Evidence of a Helical Dimerization Pattern.* Physical Review Letters, 2004. **92**(5): p. 056402.

29. McQueen, T.M., et al., *Successive Orbital Ordering Transitions in $NaVO_2$.* Physical Review Letters, 2008. **101**(16): p. 166402.

30. Komaba, S., et al., *Electrochemically Reversible Sodium Intercalation of Layered $NaNi_{0.5}Mn_{0.5}O_2$ and $NaCrO_2$.* ECS Transactions, 2009. **16**(42): p. 43-55.

31. Giot, M., et al., *Magnetoelastic Coupling and Symmetry Breaking in the Frustrated Antiferromagnet α-$NaMnO_2$.* Physical Review Letters, 2007. **99**(24): p. 247211.

32. McQueen, T., et al., *Magnetic structure and properties of the S=5/2 triangular antiferromagnet α-$NaFeO_2$.* Physical Review B, 2007. **76**(2): p. 024420.

33. Takahashi, Y., Y. Gotoh, and J. Akimoto, *Single-crystal growth, crystal and electronic structure of $NaCoO_2$.* Journal of Solid State Chemistry, 2003. **172**(1): p. 22-26.

34. Matsumura, T., et al., *Synthesis, structure and physical properties of $Li_xNa_{1-x}NiO_2$.* Solid State Ionics, 2002. **152-153**(0): p. 303-309.

35. Mazin, I.I., *Electronic structure and magnetism in the frustrated antiferromagnet $LiCrO_2$: First-principles calculations.* Physical Review B, 2007. **75**(9): p. 094407.

36. Croguennec, L., et al., *Nature of the stacking faults in orthorhombic $LiMnO_2$.* Journal of Materials Chemistry, 1997. **7**(3): p. 511-516.

37. Wu, S.-h. and M.-t. Yu, *Preparation and characterization of o-$LiMnO_2$ cathode materials.* Journal of Power Sources, 2007. **165**(2): p. 660-665.

38. Kim, J.-M. and H.-T. Chung, *Electrochemical characteristics of orthorhombic $LiMnO_2$ with different degrees of stacking faults.* Journal of Power Sources, 2003. **115**(1): p. 125-130.

Chapter 5

Effects of cation substitution on structural defects in layered $LiNiO_2$

5.1 Introduction

Layered rock salt structure materials with the general formula $LiMO_2$ (M=transition metal) have been studied intensively due to their applicability as cathode materials in lithium ion batteries. $LiCoO_2$ is the prototype commercially used cathode. However cobalt is toxic and expensive. The search for replacements for cobalt-based cathodes has lasted for decades. $LiNiO_2$ is one of the potential cathode materials for lithium ion batteries. Although this compound has been intensively studied for many years, the electronic, magnetic and local structures are still highly controversial[1, 2], as discussed in chapter 3.

Experimentally it is not yet possible to synthesise perfect, stoichiometric $LiNiO_2$. A certain fraction of extra nickel ions occupy the lithium site making the true formula of the material $[Li_{1-x}Ni_x]NiO_2$[3] (This is referred to hereafter as an extra Ni defect).

A recent theoretical study on $LiNiO_2$ also predicts an unavoidable high concentration of Ni present in the Li layers at high temperature[4]. Besides, 11% of Li-Ni interlayer mixing (cation exchange between Li and Ni in the expected layered structure) is reported to occur in the $LiNiO_2$-based materials $LiNi_{1/2}Mn_{1/2}O_2$ and 6% $LiNi_{1/3}Mn_{1/3}Co_{1/3}O_2$[5, 6]. The presence of Ni in the Li layers has a detrimental effect on the electrochemical performance of the material as a cathode. First, it disrupts the lithium diffusion by blocking the diffusion pathways[7]. Second, it has been suggested that the presence of nickel in the lithium layer is responsible for first-cycle irreversibility[8-10]. During the first charge, the Ni^{2+} ions at Li sites are oxidised to smaller Ni^{3+} ions. This causes a local shrinkage around those nickel ions and therefore it is difficult to insert lithium ions back into the positions around them.

Oxygen loss is another issue in layered cathode materials. A recent study on $LiNi_{0.8}Mn_{0.1}Co_{0.1}O_{2-\delta}$ demonstrated that up to ~12% oxygen loss occurs depending on the synthesis conditions and there is a strong correlation between oxygen content and electrochemical performance[11]. As introduced in chapter 1, delithiated $Li_{1-x}NiO_2$ is not thermally stable. It undergoes a phase transition accompanied by oxygen evolution. It has been shown that the extent of oxygen evolution increases as x increases[12]. This irreversible structural change concomitant with oxygen loss may be responsible for the observed capacity fading[13, 14].

In order to improve the electrochemical performance of $LiNiO_2$, the strategy of partial substitution of Ni by other metal cations has been deployed. It is known that Co substitution gives better 2-D layered character. For $LiNi_{1-x}Co_xO_2$ with $x > 0.3$, nickel is no longer present in the lithium layer[15]. As a result, the irreversibility at the first-cycle mentioned above disappears. By contrast, the interlayer mixing increases with Mn doping[16]. Nevertheless, $Li_xNi_{0.5}Mn_{0.5}O_2$ exhibits excellent structural stability at low Li content against oxygen loss[17] and therefore better safety. Al doping improves the thermal stability although Ni is still found in the Li layer[18, 19]. Cycling tests show that 10% aluminium suppresses all the phase transitions observed for the Li_xNiO_2 system[19].

Although the properties produced by partial cationic substitution are well studied, the reasons why these foreign dopants produce them are not clear. In this study, first-principles calculations were performed to investigate the structural defects of Li-Ni anti-site, extra Ni and oxygen vacancy in $LiNiO_2$ and the effect of Ni substitution by Co ($LiNi_{0.5}Co_{0.5}O_2$), Al ($LiNi_{0.5}Al_{0.5}O_2$) and Mn ($LiNi_{0.5}Mn_{0.5}O_2$). Same structural defects in $NaNiO_2$ and $LiCoO_2$ are also calculated for comparison.

5.2 Point defects in crystals

Perfect crystals do not exist. According to the dimensionality, defects in crystals can be categorized into point defects, line defects and planar defects. It is the point defects we are concerned with here. Figure 5-1 shows some common point defects. They are vacancies, interstitial and substitutional impurities. The vacancy defect means that there are ions missing from their lattice and result in vacant lattice sites. The interstitial defect is that an atom occupies a position in the crystal which is not a regular lattice site. The substitutional impurity means that an atom at its regular lattice site is replaced by a foreign element, such as doping in semiconductors. Apart from the above defects, there is another defect called the anti-site defect in which two atoms swap their regular lattice sites. In ionic solids, different types of defects usually occur simultaneously in order to maintain the charge neutrality - for example the *Frenkel disorder* and *Schottky disorder* in an ionic binary compound M^+X^-. The *Frenkel disorder* means one atom is displaced from its normal site to an interstitial site, i.e. a vacancy defect and an interstitial defect are created simultaneously. In the *Schottky disorder*, one cation and one anion are missing together, i.e. two vacant sites are created simultaneously. The charge neutrality can also be retained by the creation of electrons or holes, i.e. electronic and hole defects.

In transition metal oxides, due to variable valency of transition metal ions, the concentration of point defects can be very high and compounds are frequently non-stoichiometric. Non-stoichimetric compounds are characterised with a single phase over a range of compositions. For example in VO_x the oxygen content x can range from 0.79 to 1.29. In addition, the charge compensation associated with defect formation in transition metal oxides often takes place on transition metal ions by changing its charge state because charges in transition metal oxides often easily localise in the form of small polarons.

Defects in ionic crystals are commonly described using the Kröger–Vink notation:

$$M_S^C$$

In the representation M corresponds to atoms or vacancies and can also be electrons (*e*) or holes (*h*). S indicates the lattice site in perfect crystal that is occupied by M. C indicates the electronic charge of M relative to the species originally occupying that site. Positive charge is denoted by ·, negative charge is denoted by $'$ and zero charge is denoted by x.

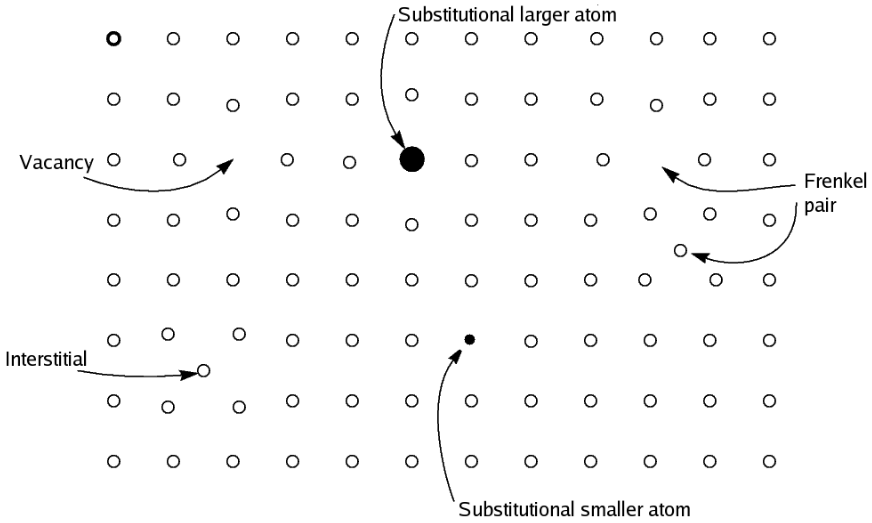

Figure 5-1: Schematic view of point defects

The importance of studying defects arises because they have an impact on properties of materials. For example $YBa_2Cu_3O_{7-x}$ can be tuned to be either an insulator or a superconductor depending on the amount of oxygen deficiency[20]. In solid electrolytes, the ionic conductivity is usually correlated with defect concentration[21, 22]. Therefore if we can control the concentration of defects, properties of materials can be manipulated.

5.2.1 Defects in thermal equilibrium at the dilute limit

At any finite temperature all crystals contain certain amount of defects because the defect formation is thermodynamically favoured. Let us consider a crystal containing N regular sites but n of them are occupied by one species of defect, for example vacancies in a simple metal. The change in free energy for the creation of n point defects in a perfect crystal is then

$$\Delta G = ng - TS_c \tag{5-1}$$

where g is the work necessary to create a single defect (defect formation energy) and S_c is the configurational entropy. Therefore although it costs free energy ng to create point defects, an entropy contribution TS_c is introduced by the creation of defects and lowers the free energy. The minimization of the free energy by the formation of defects is clearly depicted in figure 5-2.

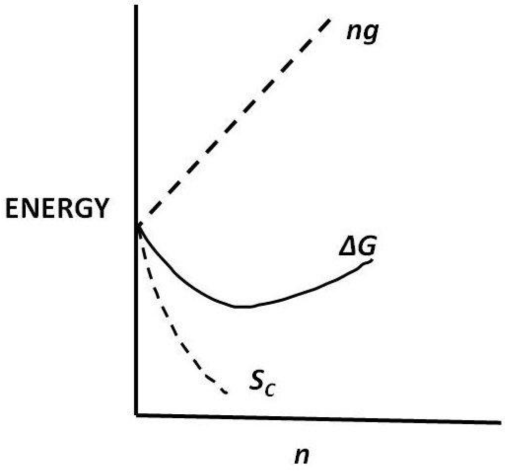

Figure 5-2: Free energy against the number of defect. This explains why point defects exist.

The configurational entropy depends on the number of ways in which the defects can be arranged W and can be expressed as

$$S_c = k \ln W \tag{5-2}$$

where k is Boltzmann's constant. Obviously in a perfect crystal there is only one way for its arrangement and $W = 1$. When there are n defects taking place in N lattice sites, the number of possible arrangements is

$$W = \frac{N!}{(N-n)!\,n!} \tag{5-3}$$

If N, $(N-n)$ and n are all numbers, by using Stirling's approximation the configurational entropy in equation 5-2 then becomes

$$S_c = kT\left[N\ln\frac{N}{N-n} + n\ln\frac{N-n}{n}\right] \tag{5-4}$$

and when n<<N, i.e. dilute defect concentration, it becomes

$$S_c = kTn\ln\frac{N}{n} \tag{5-5}$$

At equilibrium, the free energy is the minimum with respect to the number of defecst and therefore

$$\frac{\partial \Delta G}{\partial n} = g - kT\ln\frac{N}{n} = 0 \tag{5-6}$$

By rearranging the above equation, the defect concentration $f \equiv n/N$ can then be written as

$$f = \exp\left(\frac{-g}{kT}\right) \tag{5-7}$$

It is clear that at any finite temperature T, there is a non-zero defect concentration. For defects in ionic crystals, the relation between the defect concentration and the defect formation energy is more complicated than equation 5-7. As mentioned above, there is necessarily more than one defect type and it is necessary to impose overall charge neutrality. Nevertheless, the relation between the intrinsic defect concentrations and their formation energies can usually still be expressed by a Boltzmann factor-like term.

5.2.2 Defect formation energies at the dilute limit

Through the thermodynamics of defects, one can estimate the defect concentration from the defect formation energy. The knowledge about the defect concentration can then be linked to material properties. Therefore for such purposes obtaining accurate defect formation energies is the key of studying defects. However the definition and calculation of the defect formation energy is not trivial. In recent years one formalism, originally proposed to tackle intrinsic defects in semiconductor at the dilute limit[23], has been widely used, including the recent study on layered $LiMO_2$ (M=Ni, Co, Mn, $Li_{1/3}Mn_{2/3}$)[4]. In the formalism (usually referred to as the Zhang-Northrup method), a cell representing a perfect bulk crystal containing n_i atoms of each species i is assumed to be in equilibrium with a reservoir of atoms with chemical potential μ_i for each species and a reservoir of electrons with chemical potential μ_e. When a defect is formed by removing or add Δn_i atoms and charge q and results in a defective cell with energy E^{def}, the change in Gibbs free energy (defect formation energy) can be written as

$$\Delta G_f = E^{def} - \sum_i (n_i + \Delta n_i)\mu_i + q\mu_e \tag{5-8}$$

Since the energy of the perfect supercell is

$$E_{perf} = \sum_i n_i \mu_i \tag{5-9}$$

The defect formation energy is then

$$\Delta G_f = E^{def} - E_{perf} - \sum_i \Delta n_i \mu_i + q\mu_e \qquad (5\text{-}10)$$

One should be aware that this formalism is in principle only applicable for defects at the dilute limit, results obtained from this formalism for systems where defects are clearly not dilute should be interpreted with care.

5.3 Treatments of defects in layered $LiMO_2$

In this study, we consider the presence of extra Ni in the Li layers, the Li-Ni interlayer mixing and the oxygen loss as point defects in the supposedly perfect layered $LiMO_2$. Experimentally, nearly stoichiometric $LiNiO_2$ can only be synthesized under an oxygen flow and Li_2O and NiO are often used as starting materials. Therefore the presence of NiO and Li_2O is assumed under such conditions and the extra Ni defect can be considered as occurring through the following defect reaction

$$"LiMO_2" + NiO \rightarrow Ni_{Li}^{\cdot} + M'_M + \frac{1}{2}Li_2O + \frac{1}{4}O_2 \qquad (5\text{-}8)$$

Furthermore, the focus of this study is the effect of cation substitution which is reflected from the relative defect formation energies between different compositions. The choice of a different defect reaction scheme will not alter the relative defect formation energies.

The interlayer mixing defect is considered as occurring through the reaction

$$"LiMO_2" + Li_{Li}^{\times} + Ni_{Ni}^{\times} \rightarrow Li_{Ni}'' + Ni_{Li}^{\cdot} + M_{M}^{\cdot} \qquad (5\text{-}9)$$

and the oxygen vacancy defect occurs through the reaction

$$"LiMO_2" \rightarrow V_{O}^{\cdot\cdot} + 2M_{M}' + \frac{1}{2}O_2 \qquad (5\text{-}10)$$

In this work we define defect formation energies (DFE) as the formation enthalpies of the above defect reactions at 0 K. Two assumptions are made here. First, in solid phases the volume term can be neglected and thereby the enthalpy corresponds to the internal energy. Second, defects are assumed to distribute evenly in the crystal. In the case of extra Ni defect in LiNiO$_2$, the defect formation energy per defect is then

$$\begin{aligned} DFE(extra\ Ni) &= \Delta G = \Delta H - T\Delta S \\ &\approx -E(perfect) - E(NiO) + E(defective) \\ &+ \frac{1}{2}E(Li_2O) + \frac{1}{4}E(O_2) \end{aligned} \qquad (5\text{-}10)$$

where $E(perfect)$ is the lattice energy of a perfect LiNiO$_2$ cell and $E(defective)$ is the lattice energy of the cell containing one extra Ni defect.

Similarly the defect formation energy of interlayer mixing is

$$E(interlayer\ mixing) = -E(perfect) + E(defective) \qquad (5\text{-}11)$$

where $E(perfect)$ is the lattice energy of the perfect cell and $E(defective)$ is the lattice energy of the cell containing one interlayer mixing defect.

The defect formation energy of oxygen vacancy is

$$E(oxygen\ vacancy) = -E(perfect) + E(defective) + \frac{1}{2}E(O_2) \tag{5-11}$$

where $E(perfect)$ is the lattice energy of the perfect cell and $E(defective)$ is the lattice energy of the cell containing one oxygen vacancy.

In $LiNiO_2$, since the amounts of Ni present in the Li layers and oxygen deficient are reported to be a few percent, far beyond the dilute limit, by an appropriate choice of the supercell size, correct defect concentration can be simulated.

5.4 Computational details

In this study, first-principles calculations were performed to investigate the structural defects of interlayer mixing, extra Ni and oxygen vacancy in layered $LiNiO_2$ and the effect of Ni substitution by Co ($LiNi_{0.5}Co_{0.5}O_2$), Al ($LiNi_{0.5}Al_{0.5}O_2$) and Mn ($LiNi_{0.5}Mn_{0.5}O_2$). The structural defects in layered $NaNiO_2$ and $LiCoO_2$ are also calculated for comparison.

All calculations are based on density functional theory in combination with the projector augmented wave (PAW) method[24]. The generalized gradient approximation is used with the Perdew-Burke-Ernzerhof functional[25] and a Hubbard model U correction[26] is incorporated for the d electrons to give a better description of this strongly correlated system. The U parameters used for Ni, Co and Mn are 6.5, 4.9 and 4.5 eV respectively, adapted from a self-consistent calculation[27]. The plane wave energy-cutoff is set to 500 eV. For all cells, the *k*-point spacing is less than 0.05 $Å^{-1}$ in the Brillouin zone. Structure optimizations were performed until the residual force acting on each ion was less than 0.01 eV/A. All calculations were carried out using the Vienna ab initio simulation package (VASP)[28].

For the calculation of perfect layered $LiNiO_2$, the possible ground state cell with space group symmetry $P2_1/c$ proposed in chapter 3 is used as the starting structure. In this $P2_1/c$ cell the Jahn-Teller distortions of Ni^{3+} in the NiO_2 slab are in a zigzag ordering. For calculations of layered $LiNi_{0.5}Co_{0.5}O_2$, $LiNi_{0.5}Al_{0.5}O_2$ and $LiN_{i0.5}Mn_{0.5}O_2$ the two simplest in-plane cation orderings, linear and zigzag orderings, are considered as shown in figure 5-3. Supercells with 32 formula units containing 128 atoms are used in all defect calculations. The interlayer mixing defect and extra Ni defect in such supercell correspond to a concentration of 3.125 % which is well within the experimentally reported range of defect concentration in $LiNiO_2$. Therefore the size of the cell is adequate for simulating the observed defects in $LiNiO_2$ and there is no need for the extrapolation to the infinite limit.

The interlayer mixing defect in layered AMO_2 is constructed by swapping one Ni (Co in the $LiCoO_2$ case) in the MO_2 slab with its nearest A ion. The extra Ni defect is constructed by replacing one A by Ni in the supercell. The oxygen vacancy defect is constructed by removing one oxygen from the supercell.

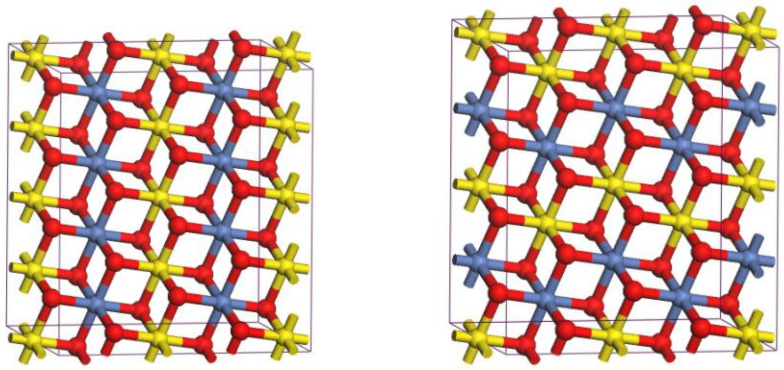

Figure 5-3: The linear (left) and zigzag (right) ordering of cations in the MO_2 slab. Red denotes oxygen. Blue and yellow denotes two different types of cations.

5.5 Results and Discussions

5.5.1 Properties of pristine compounds

Before proceeding to the defect structure calculations, crystal and electronic structure of perfect $LiNi_{0.5}Co_{0.5}O_2$, $LiNi_{0.5}Al_{0.5}O_2$ and $LiNi_{0.5}Mn_{0.5}O_2$ are first determined. In $LiNi_{0.5}Co_{0.5}O_2$ and $LiNi_{0.5}Al_{0.5}O_2$ the linear ordering of cations with space group symmetry P2/m is found to be more favourable energetically than the zigzag ordering and therefore used for subsequent defect calculations. In $LiN_{i0.5}Mn_{0.5}O_2$, the zigzag ordering of Ni and Mn with space group symmetry P2/c is more energetically favourable, in agreement with a previous theoretical study[29].

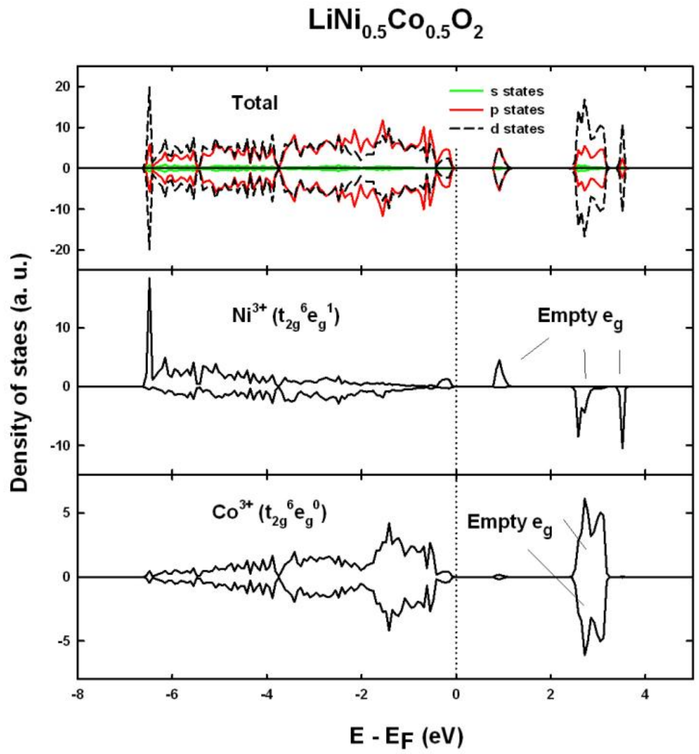

Figure 5-4: Total Density of states and local density of states on metal ions of $LiNi_{0.5}Co_{0.5}O_2$.

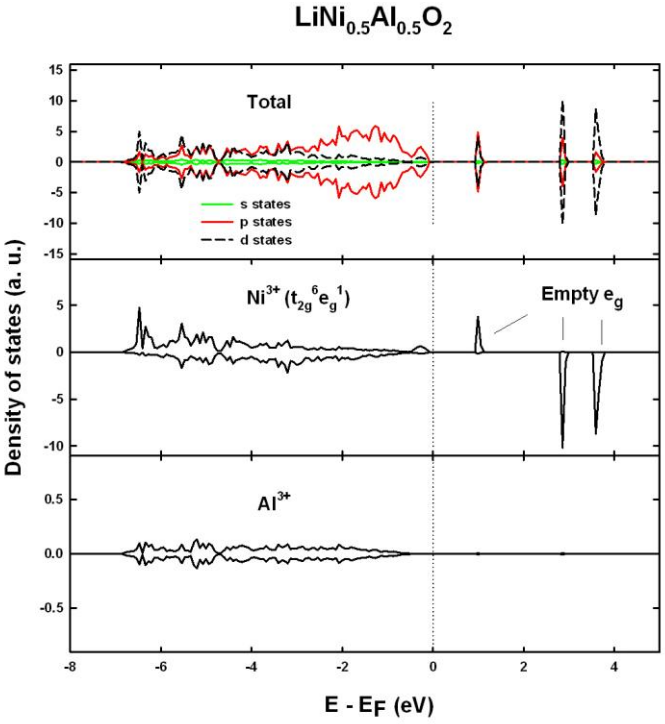

Figure 5-5: Total Density of states and local density of states on metal ions of $LiNi_{0.5}Al_{0.5}O_2$.

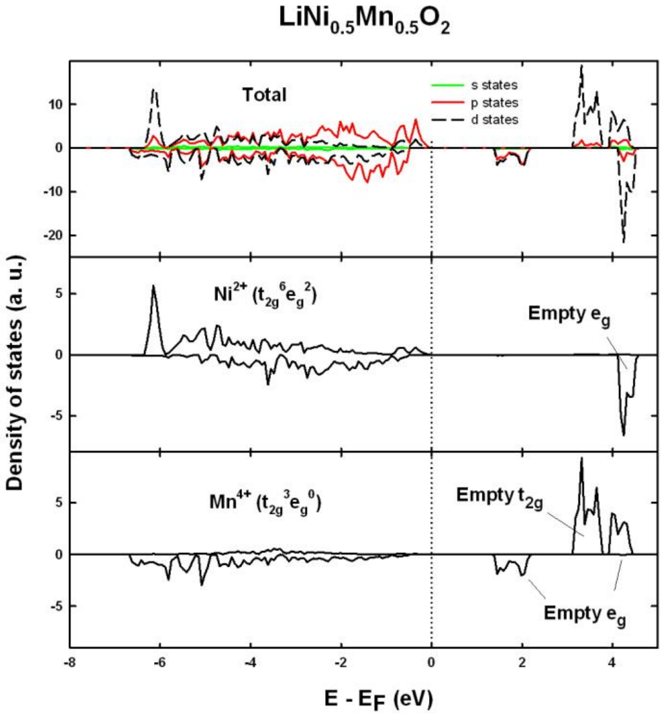

Figure 5-6: Total Density of states and local density of states on metal ions of $LiNi_{0.5}Mn_{0.5}O_2$.

Figure 5-4, 5-5 and 5-6 shows the calculated density of states. The insulating behaviour of these compunds is well reproduced with band gaps, about 0.7 eV, 0.9 eV and 1.1 eV in $LiNi_{0.5}Co_{0.5}O_2$, $LiNi_{0.5}Al_{0.5}O_2$ and $LiNi_{0.5}Mn_{0.5}O_2$ repectively. The local density of states (DOS) of Ni in $LiNi_{0.5}Co_{0.5}O_2$ shows one empty spin-up and two empty spin-down states which indicates that the electronic configuration of Ni is $t_{2g}^6e_g^1$ (S=1/2), thus low-spin Ni^{3+}, in accordance with the calculated magnetic moment 1.12 μ_B. A Jahn-Teller distortion occurs as expected on low-spin Ni^{3+} as shown from the Ni-O bond lengths in table 5-1. Cobalt ions are therefore anticipated to be Co^{3+} for the sake of charge neutrality. Indeed the empty spin-up and empty spin-down states from the local density of states of cobalt indicate that its electronic configuration is $t_{2g}^{6}e_{g}^{0}$ (S=0) meaning low-spin Co^{3+}, along with its calculated zero magnetic moment. Likewise, nickel ions are determined to be low spin Ni^{3+} in $LiNi_{0.5}Al_{0.5}O_2$ with a Jahn-Teller distortion. Nevertheless, from the Ni^{3+}-O bond lengths in table 5-1, it is clear that Ni^{3+} displays two different modes of Jahn-Teller distortion, Q_2 and Q_3 in $LiNi_{0.5}Co_{0.5}O_2$ and $LiNi_{0.5}Al_{0.5}O_2$ respectively, as shown in figure 5-7. The Q_3 mode of Jahn-Teller distortion is the one observed in $LiNiO_2$[30]. In $LiNi_{0.5}Co_{0.5}O_2$, the low-spin Co^{3+} ions are very stable in the isotropic octahedral environment with 6 identical Co^{3+}-O^{2-} bond lengths. The structural constraint imposed by the presence of rigid Co^{3+} octahedra makes the more distorted Q_3 mode less favourable and results in the Q_2 mode for distorted Ni^{3+}. This result is in agreement with an EXAFS study that in $LiNi_{1-y}Co_yO_2$ the Jahn-Teller distortion of NiO_6 octohedra is suppressed with increasing y[31]. In $LiNi_{0.5}Mn_{0.5}O_2$, two empty spin-down e_g states seen in the local density of states of nickel and fully-occupied spin-down t_{2g} states seen in the local density of states of manganese indicate that their electronic configurations are $t_{2g}^{6}e_{g}^{2}$ and $t_{2g}^{3}e_{g}^{0}$ corresponding to Ni^{2+} and Mn^{4+}, in agreement with previously reported results[32].

Table 5-1: Calculated metal-oxygen bond lengths. Angle brackets denote average bond lengths.

$LiNi_{0.5}Co_{0.5}O_2$		**$LiNi_{0.5}Al_{0.5}O_2$**		**$LiNi_{0.5}Mn_{0.5}O_2$**	
	Bond length (Å)		Bond length (Å)		Bond length (Å)
$Ni^{3+} – O$	1.88 x 2 1.95 x 2 2.08 x 2	$Ni^{3+} – O$	1.91 x 2 1.92 x 2 2.11 x 2	$Ni^{2+} – O$	2.06 x 2 2.08 x 2 2.09 x 2
$<Ni^{3+} – O>$	1.97	$<Ni^{3+} – O>$	1.97	$<Ni^{2+} – O>$	2.08
$Co^{3+} – O$	1.94 x 6	$Al^{3+} – O$	1.90 x 2 1.93 x 2 1.96 x 2	$Mn^{4+} – O$	1.92 x 2 1.95 x 2 1.98 x 2
$<Co^{3+} – O>$	1.94	$<Al^{3+} – O>$	1.93	$<Mn^{4+} – O>$	1.95

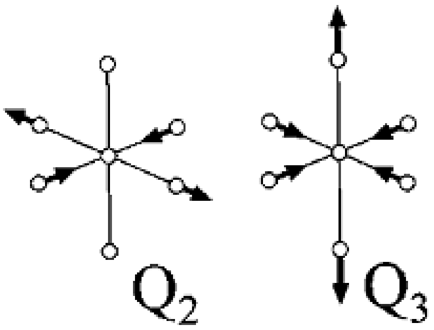

Figure 5-7: Two modes of Jahn-Teller distortion

5.5.2 Change of charge states of metal ions induced by defect formations

In all $LiMO_2$ cells with extra Ni and interlayer mixing defects, the calculated magnetic moment of 1.7 μ_B (S=1) of the Ni present in the Li layer along with its average Ni-O bond length 2.07 Å together imply that it is Ni^{2+}. Therefore in the $LiNiO_2$, $LiNi_{0.5}Co_{0.5}O_2$ and $LiNi_{0.5}Al_{0.5}O_2$ cells with the interlayer mixing defect, in order to retain charge neutrality one Ni in the NiO_2 slab is oxidised from Ni^{3+} to Ni^{4+} with calculated magnetic moment 0.19 μ_B (S=0), as seen in the spin density contour map of the top graph in figure 5-8, and average Ni-O bond length 1.89 Å. In the $LiNi_{0.5}Mn_{0.5}O_2$ cell, the interlayer mixing defect does not cause any change of charge state as nickel ions are already Ni^{2+}.

In cells with the extra Ni defect, since one Li^+ is replaced by Ni^{2+}, one metal ion in the MO_2 slab must be reduced to keep the charge neutrality. In the $LiNiO_2$, $NaNiO_2$, $LiNi_{0.5}Co_{0.5}O_2$ and $LiNi_{0.5}Al_{0.5}O_2$ cells, it is the Ni in the MO_2 slab that gets reduced from Ni^{3+} to Ni^{2+} with calculated magnetic monent 1.7 μ_B (S=0) and average Ni-O bond length 2.07 Å. The preferred change of charge state on Ni rather than Co in $LiNi_{0.5}Co_{0.5}O_2$ is probably due to the relatively stable electronic configuration of Co^{3+} ($t_{2g}^6e_g^0$). In $LiNi_{0.5}Mn_{0.5}O_2$, the charge state of Ni^{2+} cannot be reduced anymore and therefore the charge compensation accompanied by the extra Ni defect takes place on manganese with $Mn^{4+} \rightarrow Mn^{3+}$. The middle graph of figure 5-8 shows the case of the extra-Ni defect in $LiNi_{0.5}Mn_{0.5}O_2$. The e_g orbital character on Ni^{2+} ($t_{2g}^6e_g^2$) can be seen from the shape of spin density pointing towards oxygens. Similarly, the spin density on Mn^{4+} ($t_{2g}^3e_g^0$) pointing away from oxygen represents the t_{2g} orbital character. The Mn showing different shape of spin density is the one gets reduced from Mn^{4+} to Mn^{3+}.

In cells with the oxygen vacancy defect, two metal ions in the MO_2 next to the oxygen vacancy site are reduced to keep the charge neutrality. The bottom graph in figure 5-8 clearly shows that two Co^{3+} ions are reduced to Co^{2+} upon the removal of one oxygen ion.

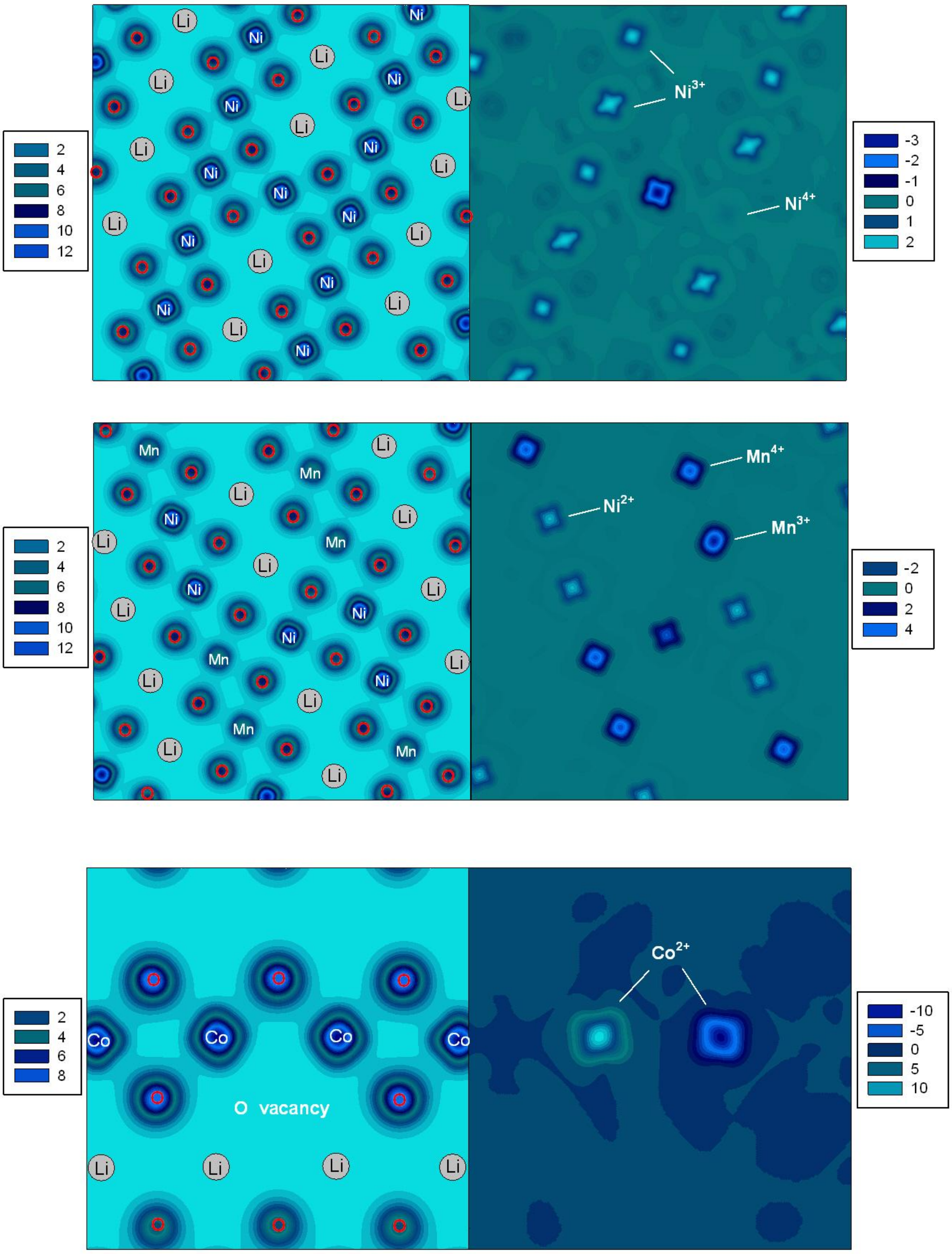

Figure 5-8: Charge density (left) and spin density (right) contour maps (e/Å^3) of $LiNiO_2$ with the Li-Ni anti-site defect (top), $LiNi_{0.5}Mn_{0.5}O_2$ with the extra-Ni defect (middle) and $LiCoO_2$ with the oxygen vacancy defect (bottom).

5.5.3 Stabilities of defects and the effect of cation substitution

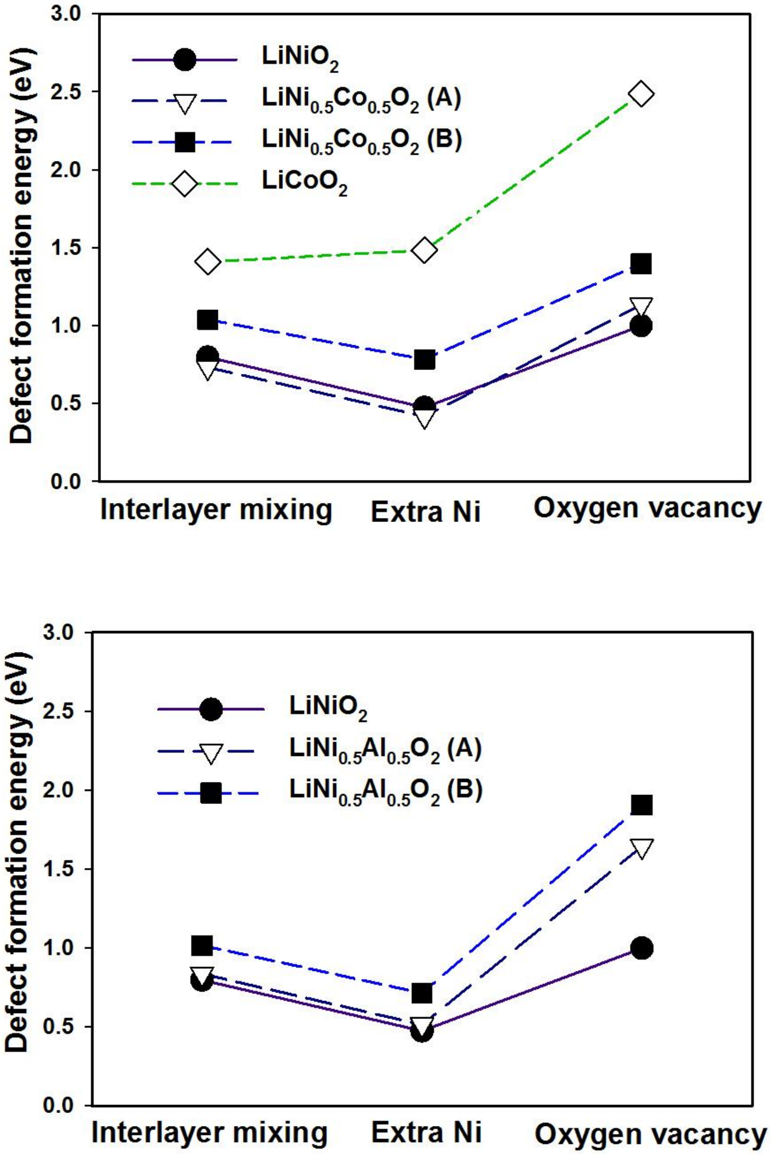

Figure 5-9: The effect of Co and Al substitution on calculated defect formation energies.

The calculated defect formation energies in $LiNiO_2$ are shown in figure 5-9. The calculated formation energies of the three defects in $LiNiO_2$ are all small, ranging from approximately 0.3 to 1.0 eV. This is consistent with the difficulty to synthesize stoichiometric defect-free $LiNiO_2$. It is shown in the previous chapter that the cation arrangement in rock salt structure compounds depends strongly on the cation interactions if the size effect is insignificant. Therefore we suggest that the presence of Ni ions in the Li layers in the supposedly layered $LiNiO_2$ is stabilized by the 180° Ni-O-Ni superexchange interaction, which results in the low formation energies of the interlayer mixing and the extra Ni defects. Nevertheless, the extra Ni defect is the most favourable and therefore is the predominant defect species in $LiNiO_2$.

In $LiNi_{0.5}Co_{0.5}O_2$ and $LiNi_{0.5}Al_{0.5}O_2$ due to the linear cation ordering in the transition metal plane, there are two inequivalent Li sites on which to place the Ni in the interlayer mixing and the extra Ni defects, as shown in figure 5-10, and we refer to them as configurations A and B. In $LiNi_{0.5}Mn_{0.5}O_2$, the zigzag ordering of Ni and Mn also results in two inequivalent Li sites referred to as A and B. Similarly in the cells of $LiNi_{0.5}Co_{0.5}O_2$, $LiNi_{0.5}Al_{0.5}O_2$ and $LiNi_{0.5}Mn_{0.5}O_2$, there are two inequivalent oxygens, one bonding with two Ni and one bonding with one Ni, in the cell which can be removed to create the oxygen vacancy. We refer to the removal of the oxygen bonding with two Ni as configuration A and the removal of the oxygen bonding with only one Ni as configuration B.

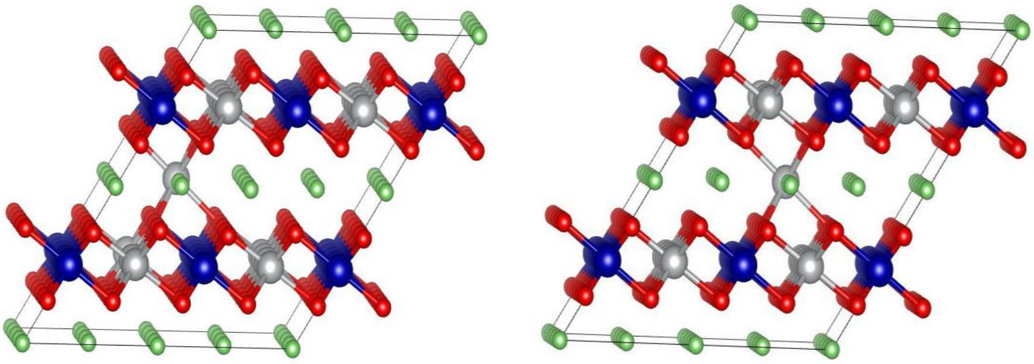

Figure 5-10: Two inequivalent positions in the Li layer, configuration A (left) and B (right). The grey sphere denotes Ni. The blue sphere denotes Co. The green sphere denotes Li. And the red sphere denotes O.

The effect of Co substitution can be seen in the top panel of figure 5-9. It is first noted that the defect formation energies of the interlayer mixing and the extra Ni defects in $LiNi_{0.5}Co_{0.5}O_2$ drop lower than in $LiNiO_2$. This is rather surprising since it is known that experimentally Co substitution in $LiNiO_2$ suppresses the presence of Ni in the Li layer. Nevertheless the formation energies of the interlayer mixing and extra Ni defects are higher in configuration B than configuration A by about 300 meV and 360 meV respectively. This can be explained by the exchange interactions discussed in chapter 4. As seen in figure 5-10, in configuration A, the Ni in the Li layer forms six 180˚ Ni-O-Ni chains. In configuration B, the six 2nd-nearest-neighbours, in the cation sublattice, of the Ni in the Li layer are Co^{3+}, forming 180˚ Ni-O-Co chains which does not give rise to the 180˚ superexchange interaction due to the empty e_g orbitals of Co^{3+} ($t_{2g}^6 e_g^0$). This again confirms that the presence of Ni^{2+} in the Li layer is stabilized by the 180˚ Ni-O-Ni superexchange interaction. The higher number of the 180˚ Ni-O-Ni chains gives rise to the lower energy. In the real $LiNi_{0.5}Co_{0.5}O_2$ compound, the Co^{3+} ions distribute randomly in the MO_2 slab and the main effect of cobalt substitution is screening the 180˚ Ni-O-Ni superexchange interaction. This is different from a previous proposed size effect[15], and therefore destabilizes the presence of Ni in the Li layer.

The defect formation energies in $LiCoO_2$ are also shown in the top panel of figure 5-9. The defect energies of the interlayer mixing defect and the extra Co defect are considerably higher than Ni containing compounds. This agrees with experimentally observed perfect layered $LiCoO_2$. Owing to the electronic configuration of Co^{3+} in the CoO_2 slab, there is no interaction between Co ions that can stabilize the presence of Co in the Li layer.

Since there is no d electron in the Al^{3+} ion, there is no superexchange interaction between Al^{3+} and Ni^{2+}. A similar effect of Al substitution to Co substitution on defect formation energies is therefore expected because Al substitution should also effectively screen the Ni-O-Ni superexchange interaction. Indeed by adopting the linear cation ordering in the $LiNi_{0.5}Al_{0.5}O_2$ cell (left panel in figure 5-3), as shown in the bottom panel of figure 5-9 the calculated formation energies of the interlayer mixing and the extra Ni defects are very similar to those in $LiNi_{0.5}Co_{0.5}O_2$. Defects of configuration A are also more favourable due to the stabilisation by the exchange interaction. However, unlike in $LiNi_{1-x}Co_xO_2$ with $x > 0.3$ neither the interlayer mixing defect nor extra Ni defects are observed[15]. Experimentally 5% of extra-nickel ions are still found in the lithium layer in $LiNi_{1-x}Al_xO_2$ with $0.1 < x < 0.5$[19].

Therefore the assumption of even distribution of Ni and Al is probably not correct and this result backs up the theory that Al tends to segregate to interfaces[33] and that a core-shell structure may be formed[34] in $LiNi_{0.5}Al_{0.5}O_2$. Consequently, the extra-Ni and Li-Ni anti-site defects can still occur in Ni-rich domains in $LiNi_{0.5}Al_{0.5}O_2$ as in $LiNiO_2$, where the presence of Ni in the Li layer can be stabilized by the 180° Ni-O-Ni exchange interaction.

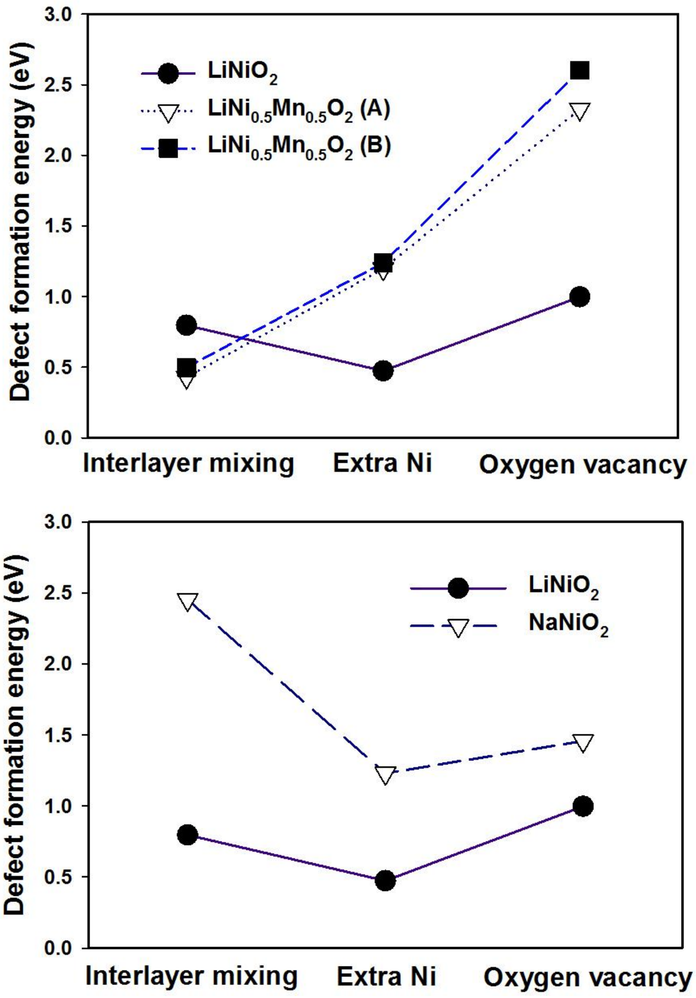

Figure 5-11: Calculated defect formation energies in $LiNi_{0.5}Mn_{0.5}$ and $NaNiO_2$ compared to $LiNiO_2$.

In $LiNi_{0.5}Mn_{0.5}O_2$, as shown in the top panel of figure 5-11 there is no significant difference in configuration A and B of the formation energy of the interlayer mixing and the extra Ni defects. The formation energy of the interlayer mixing is markedly lower than the extra-Ni defect. This is consistent with the experimentally observed high concentration of interlayer mixing defects in $LiNi_{0.5}Mn_{0.5}O_2$. Also the formation energy of the interlayer mixing defect is even lower than in $LiNiO_2$ by about 0.3 eV. Unlike in $LiNi_{0.5}Co_{0.5}O_2$ and $LiNi_{0.5}Al_{0.5}O_2$ where the 180˚ Ni-O-Co and 180˚ Ni-O-Al interactions are absent, in $LiNi_{0.5}Mn_{0.5}O_2$ the electronic configuration of Mn^{4+} ($t_{2g}^3e_g^0$) could give rise to moderate 180˚ Ni^{2+}-O^{2-}-Mn^{4+} interactions[35]. Consequently although the number of 180˚ Ni-O-Ni interaction is reduced due to Mn substitution, the presence of Ni^{2+} can be stabilized not only by the 180˚ Ni-O-Ni interaction but also the 180˚ Ni^{2+}-O^{2-}-Mn^{4+} interaction. And since the ionic radius of Ni^{2+} is similar to Li^+, these ions can exchange sites readily without significant rearrangement of the surrounding atomic positions. Besides no charge compensation is necessary to create the interlayer mixing defect in $LiNi_{0.5}Mn_{0.5}O_2$. In contrast to the interlayer mixing defect, the extra Ni defect is hugely destabilised in $LiNi_{0.5}Mn_{0.5}O_2$ compared to $LiNiO_2$ as the defect formation energy is much higher. The reason is probably that the reduction of Mn^{4+} to Mn^{3+}, which is the charge compensation accompanying the extra-Ni defect, is considerably less favourable than the reduction of Ni^{3+} to Ni^{2+} due to the stable electronic configuration of Mn^{4+} ($t_{2g}^3e_g^0$).

In $NaNiO_2$, the structural constraint comes from the large ionic size of Na^+. It is shown in table 5-2 that for the zigzag ordering of the Ni^{3+} Jahn-Teller distortions or charge disproportionation $Ni^{3+} \rightarrow Ni^{2+}+Ni^{4+}$ in the NiO_2 slab to happen, the LiO_6 octahedron must undergo significant distortion. The larger Na^+ ion, compared to Li^+, fills up the interslab space completely (more closely packed) and forbids the zigzag ordering of the Ni^{3+} Jahn-Teller distortions or charge disproportionation $Ni^{3+} \rightarrow Ni^{2+}+Ni^{4+}$ in the NiO_2 slab. Hence the Ni^{3+} Jahn-Teller distortions in $NaNiO_2$ are forced to align collinearly as observed experimentally, which results in undistorted NaO_6 octahedra. This gives a good 2-D layered character and is less susceptible to defects as manifested in the high defect formation energies compared to $LiNiO_2$ as shown in the bottom panel in figure 5-11. Actually because of the dramatic difference in ionic radii between Na and first-row transition metal M, the size effect dominates the interactions between cations and consequently all $NaMO_2$ are reported to form perfect layered structures as already pointed out in chapter 4.

Table 5-2: Li-O bond lengths in the three different $LiNiO_2$ cells

	Li – O bond lengths (Å)
C2/m (collinear ordering of the Ni^{3+} Jahn-Teller distortions)	2.11 x 4 2.13 x 2
$P2_1/c$ (zigzag ordering of the Ni^{3+} Jahn-Teller distortions)	2.04 x 2 2.10 x 2 2.24 x2
P2/c (charge disproportionation $Ni^{3+} \rightarrow Ni^{2+}+Ni^{4+}$)	2.03 x 2 2.08 x 2 2.19 x 2

5.5.4 Oxygen vacancy

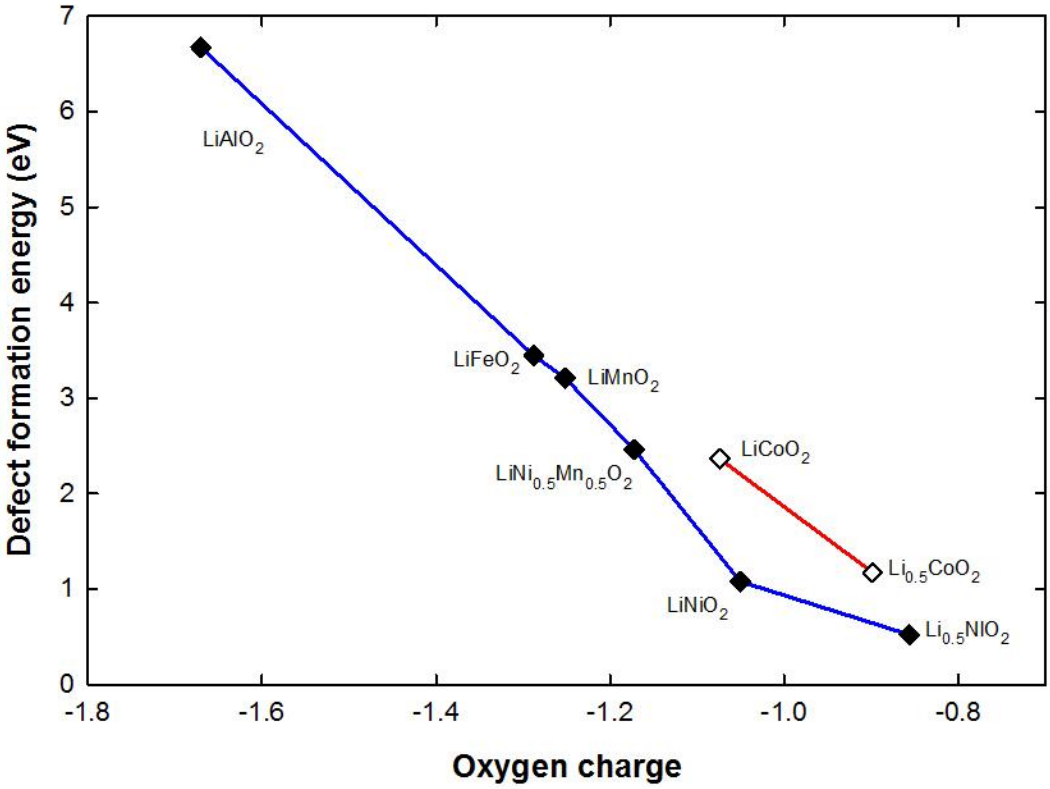

Figure 5-12: Correlation between oxygen charge and defect formation energy of the oxygen vacancy.

Figure 5-12 shows the calculated defect formation energy of the oxygen vacancy against calculated oxygen charge by using the Bader charge analysis[36, 37]. The charge on oxygen should be closer to -2 in highly ionic compounds. However in transition metal oxides, there is a considerable overlap between the oxygen 2p and metal 3d orbitals. The metal-oxygen bond length is shorter for late transition metals or metals with higher charge states and thereby greater overlap between oxygen 2p and metal 3d orbitals is observed. This is reflected in the calculated oxygen charge as shown in figure 5-12, from left to right ($LiAlO_2$ → $LiNiO_2$ and $LiCoO_2$ → $Li_{0.5}CoO_2$), the decrease of calculated oxygen charge is a consequence of the increase in overlapping between oxygen 2p and metal ion 3d orbitals. The important point here is that a correlation can be clearly seen between the formation energy of the oxygen vacancy defect and the calculated oxygen charge. Also as shown in figure 5-9 and figure 5-10, in $LiNi_{0.5}Co_{0.5}O_2$, $LiNi_{0.5}Al_{0.5}O_2$ and $LiNi_{0.5}Mn_{0.5}O_2$, the defect formation energy for removing the oxygen bonding to two Ni (configuration A) is lower than the oxygen bonding with one Ni (configuration B). The oxygen bonding with two Ni has lower charge. It appears that the smaller the oxygen charge is, the easier it is to remove the oxygen. It has been suggested that in terms of ionic bonding, the strength of the metal-oxygen bond depends on the effective charge on oxygen[38]. Therefore the smaller the oxygen charge, the weaker the bonding is. However it is not clear whether this is the true explanation for this correlation or not. In addition when the charge on oxygen ions is low, there would be a tendency for them to form peroxide at the surface as suggested by Goodenough et al.[39] and then dissociate through the following reaction:

$$2(O_2)^{2-} = 2O^{2-} + O_2$$

This is consistent with experimental results that the temperature for oxygen evolution on heating (i.e. the thermal stability) decreases as x decreases in layered Li_xMO_2[40-42]. It seems that low oxygen charge causes the chemical instability of an oxide compound against oxygen loss.

For example from figure 5-12 the defect formation energy of the oxygen vacancy in $Li_{0.5}NiO_2$ is lower than in $LiNiO_2$. The common argument for the thermal instability of Li_xNiO_2 with x<1 is associated with the presence of Ni^{4+} due to its "unconventional" high oxidation state. However Ni^{4+} has the same electronic configuration $t_{2g}^6e_g^0$ as Co^{3+} in an octahedral site which is very stable in $LiCoO_2$. It is equally possible to argue that it is the low amount of charge on oxygen associated with Ni^{4+} that causes the instability of the compound.

Comparing $LiNiO_2$ with $LiCoO_2$ there is no noticeable difference in the oxygen charge, but the defect formation energy of the oxygen vacancy in $LiCoO_2$ is significantly higher than in $LiNiO_2$ (by about 1.2 eV). This is probably due to the relatively stable electronic configuration of low-spin Co^{3+} $t_{2g}^6e_g^0$. Therefore by creating an oxygen vacancy, it costs more energy to reduce Co^{3+} to Co^{2+} than to reduce Ni^{3+} to Ni^{2+} in $LiNiO_2$. Although the defect formation energy of an oxygen vacancy in $LiCoO_2$ is markedly higher than in $LiNiO_2$, it drops drastically by ~1.5 eV in $Li_{0.5}CoO_2$ upon removal of half the lithium ions. This can again be explained by the decrease of oxygen charge which is associated with the creation of Co^{4+} ions.

According to the correlation between oxygen charge and the defect formation energy of the oxygen vacancy, doping with a more electro-positive cation should mitigate the oxygen loss in layered Li_xMO_2 compounds and result in better thermal stability. Indeed doping with Mn^{4+} causes a decrease in oxygen loss[43] and so does Al or Mg doping[18, 44, 45], or Ti^{4+} substitution for Mn^{4+} in $Li[Li_{0.33}Mn_{0.67-x}Ti_x]O_2$[46].

5.6 Conclusions

All calculated formation energies in the various $LiMO_2$ compounds are consistent with experiments. It is demonstrated that the defect formation energies in $LiNiO_2$ are low, in agreement with the experimental difficulty of synthesizing stoichiometric defect-free $LiNiO_2$. The driving force for the Ni ion to be present in the Li layer is the 180˚ Ni-O-Ni superexchange interaction. Therefore substituting Ni by Co in the MO_2 slab screens the 180˚ Ni-O-Ni configurations and thus effectively reduces the concentration of Ni in Li layers. Moreover, a correlation between the defect formation energy of the oxygen vacancy and oxygen charge (as measured from a Bader analysis) is noted. It appears that the smaller the oxygen charge, the lower the oxygen vacancy formation energy, although the reason is not clear. Nevertheless this explains the thermal instability of Li_xCoO_2 and Li_xNiO_2 at low x, as well as the improved electrochemical behaviour in Al, Mg or early transition metal doped $LiMO_2$. Therefore in designing better cathode materials, the use of high electropositive cations is desirable.

References

1. Chung, J.H., et al., *Local structure of $LiNiO_2$ studied by neutron diffraction.* Physical Review B, 2005. **71**(6): p. 064410.

2. Chen, H., C.L. Freeman, and J.H. Harding, *Charge disproportionation and Jahn-Teller distortion in $LiNiO_2$ and $NaNiO_2$: A density functional theory study.* Physical Review B, 2011. **84**(8): p. 085108.

3. Kanno, R., et al., *Phase Relationship and Lithium Deintercalation in Lithium Nickel Oxides.* Journal of Solid State Chemistry, 1994. **110**(2): p. 216-225.

4. Koyama, Y., et al., *Defect Chemistry in Layered $LiMO_2$ (M = Co, Ni, Mn, and $Li_{1/3}Mn_{2/3}$) by First-Principles Calculations.* Chemistry of Materials, 2012.

5. Venkatraman, S. and A. Manthiram, *Structural and Chemical Characterization of Layered $Li_{1-x}Ni_{1-y}MnyO_{2-\delta}$ ($y = 0.25$ and 0.5, and $0 \leq (1 - x) \leq 1$) Oxides.* Chemistry of Materials, 2003. **15**(26): p. 5003-5009.

6. Kim, J.-M. and H.-T. Chung, *The first cycle characteristics of $Li[Ni_{1/3}Co_{1/3}Mn_{1/3}]O_2$ charged up to 4.7 V.* Electrochimica Acta, 2004. **49**(6): p. 937-944.

7. Arai, H., et al., *Characterization and cathode performance of $Li_{1-x}Ni_{1+x}O_2$ prepared with the excess lithium method.* Solid State Ionics, 1995. **80**(3–4): p. 261-269.

8. Peres, J.P., et al., *The relationship between the composition of lithium nickel oxide and the loss of reversibility during the first cycle.* Journal of Physics and Chemistry of Solids, 1996. **57**: p. 1057-1060.

9. Zheng, S., et al., *Microstructural Changes in $LiNi_{0.8}Co_{0.15}Al_{0.05}O_2$ Positive Electrode Material during the First Cycle.* Journal of The Electrochemical Society, 2011. **158**(4): p. A357-A362.

10. Delmas, C., et al., *On the behavior of the Li_xNiO_2 system: an electrochemical and structural overview.* Journal of Power Sources, 1997. **68**(1): p. 120-125.

11. Idris, M.S. and A.R. West, *The Effect on Cathode Performance of Oxygen Non-Stoichiometry and Interlayer Mixing in Layered Rock Salt $LiNi_{0.8}Mn_{0.1}Co_{0.1}O_{2-\delta}$.* Journal of The Electrochemical Society, 2012. **159**(4): p. A396-A401.

12. Lee, K.-K., et al., *Thermal behavior and the decomposition mechanism of electrochemically delithiated* $Li_{1-x}NiO_2$*.* Journal of Power Sources, 2001. **97–98**(0): p. 321-325.

13. Muto, S., et al., *Capacity-Fading Mechanisms of* $LiNiO_2$*-Based Lithium-Ion Batteries II. Diagnostic Analysis by Electron Microscopy and Spectroscopy.* Journal of The Electrochemical Society, 2009. **156**(5): p. A371-A377.

14. Wu, L., et al., *Structural Origin of Overcharge-Induced Thermal Instability of Ni-Containing Layered-Cathodes for High-Energy-Density Lithium Batteries.* Chemistry of Materials, 2011. **23**(17): p. 3953-3960.

15. Rougier, A., et al., *Effect of cobalt substitution on cationic distribution in* $LiNi_{1-y}Co_yO_2$ *electrode materials.* Solid State Ionics, 1996. **90**(1–4): p. 83-90.

16. Rossen, E., C.D.W. Jones, and J.R. Dahn, *Structure and electrochemistry of* $Li_xMn_yNi_{1-y}O_2$*.* Solid State Ionics, 1992. **57**(3–4): p. 311-318.

17. Yabuuchi, N., et al., *Thermal Instability of Cycled* $Li_xNi_{0.5}Mn_{0.5}O_2$ *Electrodes: An in Situ Synchrotron X-ray Powder Diffraction Study.* Chemistry of Materials, 2008. **20**(15): p. 4936-4951.

18. Guilmard, M., et al., *Thermal Stability of Lithium Nickel Oxide Derivatives. Part I:* $Li_xNi_{1.02}O_2$ *and* $Li_xNi_{0.89}Al_{0.16}O_2$ *(*$x = 0.50$ *and 0.30).* Chemistry of Materials, 2003. **15**(23): p. 4476-4483.

19. Guilmard, M., et al., *Effects of aluminum on the structural and electrochemical properties of* $LiNiO_2$*.* Journal of Power Sources, 2003. **115**(2): p. 305-314.

20. Wu, M.K., et al., *Superconductivity at 93 K in a new mixed-phase Y-Ba-Cu-O compound system at ambient pressure.* Physical Review Letters, 1987. **58**(9): p. 908-910.

21. Nakamura, A. and J.B. Wagner, *Defect Structure, Ionic Conductivity, and Diffusion in Yttria Stabilized Zirconia and Related Oxide Electrolytes with Fluorite Structure.* Journal of The Electrochemical Society, 1986. **133**(8): p. 1542-1548.

22. Goff, J.P., et al., *Defect structure of yttria-stabilized zirconia and its influence on the ionic conductivity at elevated temperatures.* Physical Review B, 1999. **59**(22): p. 14202-14219.

23. Zhang, S.B. and J.E. Northrup, *Chemical potential dependence of defect formation energies in GaAs: Application to Ga self-diffusion.* Physical Review Letters, 1991. **67**(17): p. 2339-2342.

24. Kresse, G. and D. Joubert, *From ultrasoft pseudopotentials to the projector augmented-wave method.* Physical Review B, 1999. **59**(3): p. 1758.

25. Perdew, J.P., K. Burke, and M. Ernzerhof, *Generalized Gradient Approximation Made Simple.* Physical Review Letters, 1996. **77**(18): p. 3865.

26. Dudarev, S.L., et al., *Electron-energy-loss spectra and the structural stability of nickel oxide: An LSDA+U study.* Physical Review B, 1998. **57**(3): p. 1505-1509.

27. Zhou, F., et al., *First-principles prediction of redox potentials in transition-metal compounds with LDA+U.* Physical Review B, 2004. **70**(23): p. 235121.

28. Kresse, G. and J. Furthmüller *Efficient iterative schemes for ab initio total-energy calculations using a plane-wave basis set.* Physical Review B, 1996. **54**(16): p. 11169-11186.

29. Won-Sub, Y., et al., *Local Structure and Cation Ordering in O3 Lithium Nickel Manganese Oxides with Stoichiometry* $Li[Ni_xMn_{(2-x)/3}Li_{1-2x)/3}]O_2$. Electrochemical and Solid-State Letters, 2004. **7**(7): p. A167-A171.

30. Rougier, A., C. Delmas, and A.V. Chadwick, *Non-cooperative Jahn-Teller effect in* $LiNiO_2$*: An EXAFS study.* Solid State Communications, 1995. **94**(2): p. 123-127.

31. Nakai, I., et al., *Study of the Jahn–Teller Distortion in* $LiNiO_2$*, a Cathode Material in a Rechargeable Lithium Battery, byin SituX-Ray Absorption Fine Structure Analysis.* Journal of Solid State Chemistry, 1998. **140**(1): p. 145-148.

32. Reed, J. and G. Ceder, *Charge, Potential, and Phase Stability of Layered* $Li(Ni_{0.5}Mn_{0.5})O_2$. Electrochemical and Solid-State Letters, 2002. **5**(7): p. A145-A148.

33. Croguennec, L., et al., *Segregation Tendency in Layered Aluminum-Substituted Lithium Nickel Oxides.* Chemistry of Materials, 2009. **21**(6): p. 1051-1059.

34. Xu, X., et al., *Self-Organized Core–Shell Structure for High-Power Electrode in Solid-State Lithium Batteries.* Chemistry of Materials, 2011. **23**(17): p. 3798-3804.

35. Goodenough, J.B., *Magnetism and the Chemical Bond*. Inorganic Chemistry Section. Vol. 1. 1963: INTERSCIENCE (WILEY).

36. Bader, R.F.W., *Atoms in Molecules: A Quantum Theory.* Oxford University Press, 1990.

37. W Tang, E Sanville, and G. Henkelman, *A grid-based Bader analysis algorithm without lattice bias.* Journal of Physics: Condensed Matter, 2009. **21**: p. 084204.

38. Tatsumi, K., et al., *Local atomic and electronic structures around Mg and Al dopants in* $LiNiO_2$ *electrodes studied by XANES and ELNES and first-principles calculations.* Physical Review B, 2008. **78**(4): p. 045108.

39. Goodenough, J.B. and Y. Kim, *Challenges for Rechargeable Li Batteries.* Chemistry of Materials, 2009. **22**(3): p. 587-603.

40. Dahn, J.R., et al., *Thermal stability of* Li_xCoO_2, Li_xNiO_2 *and* λ-MnO_2 *and consequences for the safety of Li-ion cells.* Solid State Ionics, 1994. **69**(3–4): p. 265-270.

41. Konishi, H., T. Yuasa, and M. Yoshikawa, *Thermal stability of* $Li_{1-y}Ni_xMn_{(1-x)/2}Co_{(1-x)/2}O_2$ *layer-structured cathode materials used in Li-Ion batteries.* Journal of Power Sources, 2011. **196**(16): p. 6884-6888.

42. Furushima, Y., et al., *Thermal stability and kinetics of delithiated* $LiCoO_2$. Journal of Power Sources, 2011. **196**(4): p. 2260-2263.

43. Arunkumar, T.A., E. Alvarez, and A. Manthiram, *Chemical and structural instability of the chemically delithiated* $(1-z)Li[Li_{1/3}Mn_{2/3}]O_2\cdot(z)[Co_{1-y}Ni_y]O_2$ $(0\leq y\leq 1$ *and* $0\leq z\leq 1)$ *solid solution cathodes.* Journal of Materials Chemistry, 2008. **18**(2): p. 190-198.

44. D'Epifanio, A., et al., *Effect of* Mg^{2+} *Doping on the Structural, Thermal, and Electrochemical Properties of* $LiNi_{0.8}Co_{0.16}Mg_{0.04}O_2$. Chemistry of Materials, 2004. **16**(18): p. 3559-3564.

45. Kondo, H., et al., *Effects of Mg-substitution in* $Li(Ni,Co,Al)O_2$ *positive electrode materials on the crystal structure and battery performance.* Journal of Power Sources, 2007. **174**(2): p. 1131-1136.

46. Deng, Z.Q. and A. Manthiram, *Influence of Cationic Substitutions on the Oxygen Loss and Reversible Capacity of Lithium-Rich Layered Oxide Cathodes.* The Journal of Physical Chemistry C, 2011. **115**(14): p. 7097-7103.

Chapter 6

Conclusions

In this thesis, we have performed density function calculations to study selected $LiMO_2$ compounds that are potential cathode materials in Li ion batteries.

In chapter 3, we resolved the controversy on $LiNiO_2$ regarding its local crystal structure and electronic structure. First the interpretation of oxygen hole in $Li_xNi_{1-x}O$ is rejected. The results from our calculation suggested that although oxygen 2p character is indeed found in the holes state upon Li doping, the Jahn-Teller distortion and local density of states of Ni indicates the change of Ni oxidation states. Hence the hole is better described as localised on Ni result in Ni^{3+} upon Li doping. In the calculations of $LiNiO_2$, four different cells corresponding to different local structure were considered. We found that in the cell with P2/c space group symmetry, there are two inequivalent Ni ions with valency 2+ and 4+, indicating charge disproportionation $Ni^{3+} \rightarrow Ni^{2+} + Ni^{4+}$. Another cell with $P2_1/c$ space group symmetry, in which the Jahn-Teller distortions of octahedral surrounding the Ni^{3+} ions are in a zigzag ordering, has a similar lattice energy with the P2/c cell. The energy difference between these two cells is marginal. Therefore we suggest that in real $LiNiO_2$ samples, the two phases coexist. This explains the absence of long range ordering in $LiNiO_2$.

In chapter 4, the structural variation in rock-salt $LiMO_2$ (M = V, Cr, Mn, Fe, Co, Ni) compounds was explored. There are three different stable phases of $LiMO_2$ according to the cation orderings, layered, o-$LiMnO_2$ and γ-$LiFeO_2$. The different cation ordering cannot be explained by the size difference. Instead by embedding transition metal pairs in a MgO supercell, it is shown that the exchange interactions between transition metal ions have an effect on their site preferences and hence are responsible for the structural variation. In $LiMO_2$, the size difference between Li and M favours the layered cation ordering. The exchange interaction between 1st-nearest neighbouring transition metal ions J_1 also has the effect to stabilise transition metal ions in a 90° M-O-M configuration and hence favours the layered cation ordering. Conversely the exchange interaction between 2nd-nearest neighbouring transition metal ions in the rock-salt structure J_2 stabilises transition metals in a 180° M-O-M configuration. Therefore in $LiFeO_2$, the strong J_2 exchange interaction surpasses the size effect and the J_1 exchange interaction and results in the γ-$LiFeO_2$ cation ordering which maximises the number of the 180° Fe-O-Fe configuration.

In chapter 5, we studied the structural defect in layered $LiNiO_2$ and the effect of cationic substitution. It is found that the defect formation energies are low in $LiNiO_2$, in agreement with the difficulty to synthesise truly stoichiometric $LiNiO_2$ and the results of a recent theoretical study. The tendency of the presence for Ni to be present in the Li layers is induced by the 180° Ni-O-Ni exchange interaction. Therefore with Co substitution for Ni, the nonmagnetic Co ions screen the 180° Ni-O-Ni interaction and destabilise the presence of Ni in the Li layer. The same effect is found with Al substitution from our calculation. The substitution of Ni with Mn makes the interlayer mixing defect worse compared to the same defect in $LiNiO_2$. In addition, a correlation between the oxygen charge and the defect formation of oxygen vacancy is found. It appears that the lower the oxygen charge, the smaller the defect formation energy is.

6.1 Suggestion for designing new cathode materials

For $LiMO_2$ compounds to function as a good cathode material, the perfect layered structure is desirable. In this thesis, we have found that due to the size similarity between Li^+ and M^{3+}, the exchange interaction is an important factor that controls the cation ordering in $LiMO_2$ compounds. The 90° M-O-M exchange interaction J_1 stabilises the layered structure but the 180° M-O-M exchange interaction J_2 destabilises the layered structure. In order to stabilise $LiFeO_2$, $LiMnO_2$ and $LiNiO_2$ in the layered structure by partially cationic substitution with another cation M, M should be able to eliminate the J_2 interaction or enhance the J_1 interation. The best example is the Co^{3+} substitution for Ni in $LiNi_{1-x}Co_xO_2$ discussed in chapter 5.

In order to ease the problem of oxygen deficiency or oxygen evolution which degrades the electrochemical performance in layered Li_xMO_2, the correlation demonstrated in between the oxygen charge and the defect formation energy of oxygen vacancy suggests that, the more electropositive cations, such as early first-row transition metals, should be considered because this would result in higher oxygen charge and hence the compound would be less likely to loss oxygen.

6.2 Future work

In this thesis, bulk properties are investigated. We have learnt from our results how to control the structure and maintain structural stability of layered $LiMO_2$ compounds. This facilitates the design of safer batteries with longer life time. However it has been reported, for example in $LiNiO_2$, the electronic structure at the surface shows different characteristics from the bulk. Lithium insertion and extraction as well as oxygen evolution must all take place initially from the surface. Moreover, a solid-electrolyte interface can grow on the surface and impede the lithium diffusion. All these suggest the importance of characterisation and control of the surface structure, which play a more important role on the electrochemical performance. It is therefore well worth a thorough study on the surface structures of layered cathode materials. We should begin from investigating what is the energetically favoured $LiMO_2$ surface and study the interaction between surface and electrolyte. Once the cathode-electrolyte interface is established, we can then proceed to the study of lithium diffusion in and out of cathode and see the effect of surface structure on lithium mobility. Also the effect of different electrolytes on stabilising surface structure should be studied. This requires study of an organic/mineral interface. Such interfaces are, of course, well-known in biominerals but there are few simulation studies of this problem in the context of battery materials. The results of such study can help on controlling surface structure of cathodes and improve lithium diffusivity.

Appendix I

Bader charge analysis

In a molecule or solid atomic charges are not observables and therefore cannot be obtained from any quantum mechanical operation. Richard Bader proposed an *atoms in molecules* approach[1] for partitioning the charge in a molecule into regions associated with individual atoms that comprise the molecule. This approach uses the analysis of the real space charge density. First a set of atomic volumes are divided by zero flux surfaces. A zero flux surface is a surface on which the charge density is a minimum perpendicular to the surface. Every point $\boldsymbol{r}_s$ on the surface satisfies the following relation

$$\nabla\rho(\boldsymbol{r}_s)\cdot\boldsymbol{n}(\boldsymbol{r}_s)=0$$

where ρ is the electron density and $\boldsymbol{n}(\boldsymbol{r}_s)$ is the unit vector normal to the surface at $\boldsymbol{r}_s$. Atomic charges can then be obtained by integrating the charge density over atomic volumes. The idea of the Bader approach is clearly illustrated in figure A below.

The computational programme for performing the Bader charge analysis used in this thesis is developed by Wenjie Tand and Graeme Henkelman[2,3].

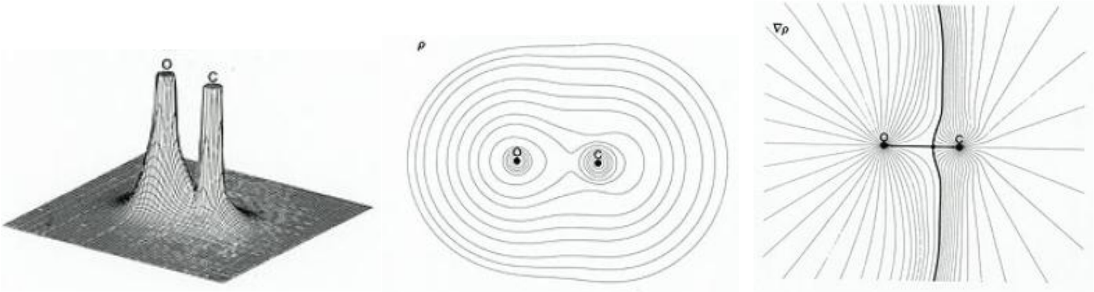

Figure A: Charge density in CO and the zero flux surface as the boundary between the two atoms [1].

References

1. Bader, R.F.W., *Atoms in Molecules: A Quantum Theory.* Oxford University Press, 1990.

2. Tang, W., Sanville, E. and Henkelman, G., *A grid-based Bader analysis algorithm without lattice bias*. Journal of Physics: Condensed Matter, 2009. **21**: p. 084204.

3. Henkelman, G., Arnaldsson, A., Jonsson, H., *A fast and robust algorithm for Bader decomposition of charge density*. Computational Material Science, 2006. **36**: p. 354-360.

Appendix II

Calculated energies in chapter 5

Table A: Calculated cohesive energies of solids and the dissociation energy of oxygen molecule used in working out defect energies from defect reactions.

Compound	***Energy (eV)**
Li_2O	-14.313
Na_2O	-11.211
NiO	-10.069
O_2	-9.846

* Energies calculated by VASP are with respect to pseudo-atoms.

** It is well known that the dissociation energy of oxygen molecule exhibits large error when LDA or GGA functionals are used. However this error cancels out when we compare defect formation energies (relative values are unaffected) in compounds with different compositions and therefore has no influence on our comparison of the results.

Table B: Calculated defect formation energies (eV) in various layered $LiMO_2$ compounds. A and B means different configurations of a defect.

	Interlayer mixing	**Extra Ni**	**Oxygen vacancy**
$LiNiO_2$	0.7968	0.4738	0.9983
$LiNi_{0.5}Co_{0.5}O_2$ (A)	0.7305	0.41593	1.13127
$LiNi_{0.5}Co_{0.5}O_2$ (B)	1.03607	0.78229	1.39668
$LiCoO_2$	1.40951	1.34512	2.48625
$LiNi_{0.5}Al_{0.5}O_2$ (A)	0.83557	0.51257	1.6458
$LiNi_{0.5}Al_{0.5}O_2$ (B)	1.01532	0.7137	1.9073
$LiNi_{0.5}Mn_{0.5}O_2$ (A)	0.42902	1.19638	2.32757
$LiNi_{0.5}Mn_{0.5}O_2$ (B)	0.49716	1.23861	2.60038
$NaNiO_2$	2.45361	1.229713	1.45924

Appendix III

Ionic radii (Å) of ions of interest

Li^+	0.76
V^{3+}	0.64
Cr^{3+}	0.615
High-spin Mn^{3+}	0.645
Fe^{3+}	0.645
Co^{3+}	0.545
Low-spin Ni^{3+}	0.56